

ABSTRACT

Title of Dissertation: **SEASONAL AND INTERANNUAL OCEAN-ATMOSPHERE VARIABILITY IN THE TROPICAL ATLANTIC: OBSERVED STRUCTURE AND MODEL REPRESENTATION**

Ching-Yee Chang, Doctor of Philosophy, 2008

Directed By: Professor James A. Carton
Professor Sumant Nigam
Department of Atmospheric and Oceanic Science

Tropical Atlantic is clamped by the South America (the Amazon) in the west and Africa (the Sahel) in the east. These two regions have been undergoing significant climate/environment changes for decades. In order to use climate models to study the impacts of these changes, climate models need to be able to well simulate the seasonal climate of the tropical Atlantic sector.

The first part of this dissertation focuses on the representation of the seasonal cycle in the CCSM3 coupled atmosphere-ocean model. CCSM3 SST has a north-south dipole pattern of bias centered at the latitude of the thermal equator, resembling the observed pattern of interannual climate variability in boreal spring. Along the equator in boreal spring CCSM3 exhibits striking westerly winds at the surface, reminiscent of the pattern of climate variability in boreal summer. The westerly winds cause deepening of the eastern thermocline that keeps the east warm despite enhanced coastal upwelling. Next, a comparison is made with a simulation using historical SST to force the atmospheric model (CAM3) in order to deduce information about the

origin of bias in CCSM3. The patterns of bias in CAM3 resemble that in CCSM3, indicating that the source of the bias in CCSM3 may be traced to difficulties in the atmospheric model.

The next chapter presents a modeling study of the origin of the westerly wind bias CAM3 by using a steady-state linearized atmospheric model. The results indicate that underestimation of rainfall over the eastern Amazon region can lead to the westerly bias in equatorial Atlantic surface winds. They suggest that efforts to reduce coupled model biases, especially seasonal ones, must target continental biases, even in the deep Tropics where ocean-atmosphere interaction generally rules.

The fourth chapter investigates the relationship between the two predominate modes of Tropical Atlantic interannual variability. The leading modes of Tropical Atlantic SST variability in boreal spring and summer are shown to be related, with the spring meridional mode leading into summer equatorial mode. The presence of a meridional mode with warm SST anomalies in the southern tropics in spring leads to a warm phase equatorial mode in summer, and vice-versa. This modal linkage occurs independently of climate variability in other ocean basins (e.g., ENSO). Atmospheric diabatic heating associated with a meridional shift of the Inter-Tropical Convergence Zone plays an important role in this relationship. The identification of this relationship enhances the prospects for prediction of boreal summer rainfall over the Guinea Coast of equatorial Africa.

SEASONAL AND INTERANNUAL OCEAN-ATMOSPHERE VARIABILITY IN
THE TROPICAL ATLANTIC: OBSERVED STRUCTURE AND MODEL
REPRESENTATION

By

Ching-Yee Chang

Dissertation submitted to the Faculty of the Graduate School of the
University of Maryland, College Park, in partial fulfillment
of the requirements for the degree of
Doctor of Philosophy
2008

Advisory Committee:
Professor James A. Carton, Chair
Professor Sumant Nigam
Professor Russell Dickerson
Dr. Semyon A. Grodsky
Professor Antonio Busalacchi

© Copyright by
Ching-Yee Chang
2008

Dedication

To my parents, who have devoted themselves to their children and to others and who have always believed in me.

Acknowledgements

I would like to express my sincerest gratitude to both of my advisers, Dr. James Carton and Dr. Sumant Nigam, for their resources that have made my studies go more smoothly, for their guidance and mentoring that have helped me go through the difficulties of the research, and for their being supportive and understanding all the time. I also would like to thank Dr. Semyon Grodsky, who has shared with me his knowledge and skills in all aspects when I needed help, and Dr. Alfredo Ruiz-Barradas for sharing the datasets. I would like to thank the committee members for their time and for their insightful suggestions to my dissertation.

I would like to thank many friends, Dr. Renu Joseph, Dr. Alfredo Ruiz-Barradas, Dr. Jin-ho Yoon, Bin Guan, and Hailong Liu and other fellow students, for sharing many interesting discussions with me; especially I want to thank Dr. Shu-Chih Yang who has been both a friend and a helper to me all the time. I also would like to thank my friend Dr. Yiing-Rei Chen, who is always there for me, even when she has returned to Taiwan. This can not go without mentioning my Chemical Physics friends: Brooke Hester, Craig Stutts, Danny Rodgers, and Mandy Woodward. They have made my life at UMD more colorful and interesting.

My thanks also go to my husband, Yi-Hsing Peng, who and I have supported and cheered up each other through all the difficulties and who shares all the happiness and sadness in our life together. Also thank my daughter, Sophia, who has given some challenge and much more joy and happiness to my life.

Table of Contents

Dedication	ii
Acknowledgements	iii
Table of Contents	iv
List of Tables	v
List of Figures.....	vi
Table of Acronyms.....	x
1. Introduction.....	1
1.1. Climate in the Tropical Atlantic sector.....	1
1.2. Modeling of the Tropical Atlantic climate.....	8
2. Seasonal Climate of the Tropical Atlantic Sector in the NCAR CCSM3: Error Structure and Probable Causes of Errors	11
2.1. Introduction.....	11
2.2. Model and data.....	12
2.3. Results.....	16
2.4. Summary and discussion.....	34
3. Origin of the Spring-time Westerly Bias in Equatorial Atlantic Surface Winds in CAM3 Model Simulations	39
3.1. Introduction.....	39
3.2. Datasets and diagnostic model.....	41
3.3. CAM3 biases in the Tropical Atlantic	44
3.4. Dynamical diagnosis of CAM3's westerly bias in surface winds	49
3.5. Summary and concluding remarks.....	59
4. Tropical Atlantic Variability and Prediction of Summer West African Rainfall.....	64
4.1. Introduction.....	64
4.2. Datasets and analysis methods.....	67
4.3. Results.....	69
4.4. Mechanism supporting the model relationship.....	84
4.5. The modal relationship and prediction of summer West African rainfall	88
4.6. Summary and concluding remarks.....	95
5. Summary and Concluding Remarks.....	101
Appendices.....	104
A. The second and third modes in boreal spring and summer.....	104
B. The relation between the North Atlantic Oscillation and the first three modes in both seasons	105
C. Climate general circulation models.....	109
Bibliography	111

List of Tables

Table 4.1 Correlation coefficients between the PCs and the summer Guinea Coast rainfall index. Shaded numbers are those also shown in Figure 4.12.	95
Table B.1 Correlation between 3-month-averaged NAO index and the PCs. Numbers in red font indicates the correlation is above 95% of significance. The shaded cases are used for plotting the correlation between the PCs and the SSTAs.	105

List of Figures

Figure 1.1 Scatterdiagram of monthly mean SST for the equatorial cold tongue region of Atlantic (4°S-4°N, 16°W-4°E) and the Pacific (4°S-4°N, 104-86°W) oceans. Unit: °C. (From Mitchell and Wallace 1992).....	5
Figure 2.1 Seasonal SST. a) Observed; b) CCSM3; and c) SST bias (CCSM3-Obs). Contour interval: 1°C.	18
Figure 2.2 Observed and CCSM3 equatorial SST and zonal winds (averaged from 4S to 0N) versus longitude. a) SST; b) Annual and semiannual harmonics of SST. Unit: °C. c) Observed, CCSM3 and CAM3 zonal winds. Contour interval: 1 m/s.....	20
Figure 2.3 Seasonal CCSM3 ocean heat content bias and depth of thermocline. a) Bias in averaged upper ocean temperature (averaged 5m-96m). Contour intervals: 1°C. b), c) and d) Depth of the thermocline (as indicated by the depth of the 20C isotherm) in northern tropical Atlantic (averaged 25°N-30°N and averaged 10°N-15°N) and equatorial area (averaged 5°S-0°N) for CCSM3 (red, solid line) and observed (blue, dashed line). Unit: m.....	22
Figure 2.4 Seasonal surface winds. a) Observed; b) CCSM3; c) CCSM3 zonal wind bias; d) CCSM3 meridional wind bias; e) CAM3 zonal wind bias; f) CAM3 meridional wind bias. Contour intervals: 1 m/s.	24
Figure 2.5 Seasonal SLP. a) Observed; b) CCSM3; c) CCSM3 bias; d) CAM3 Bias. Contour intervals: a) and b) 2 mb; c) and d) 0.5 mb.....	25
Figure 2.6 Seasonal atmospheric vertical velocity (negative omega) with latitude and height along 0°E. Red indicates ascending motion and blue descending motion. Contour intervals are 0.01Pa/s. a) Observed; b) CCSM3; c) CCSM3 bias.	27
Figure 2.7 Seasonal precipitation. a) Observed; b) CCSM3; c) CCSM3 bias; d) CAM3 bias. Contour intervals are 2 mm/day for a) and b), and 1 mm/day for c) and d).....	29
Figure 2.8 Seasonal surface radiative fluxes. a) Observed net short wave radiation; b) CCSM3 net short wave radiation bias; c) CAM3 net short wave radiation bias. Contour intervals: 20 W/m ²	31
Figure 2.9 Seasonal Ekman vertical velocity. a) Observed; b) CCSM3; c) CCSM3 bias. Contour intervals are 4•10 ⁻⁶ m/s for a) and b), and 2•10 ⁻⁶ m/s for c).....	33
Figure 2.10 Zonal current averaged 2S-2N during MAM. Depth of the 20C isotherm is superimposed in grey. Left: Observed; Right: CCSM3. Contour interval: 20cm/s...	34
Figure 2.11 SST bias of a) CCSM3 and b) NCEP CFS (see <i>Saha et al., 2005</i> for model details). Contour intervals: 1°C.....	37
Figure 3.1. Seasonal evolution of the surface zonal wind (upper panels, 1 m/s), zonal wind bias (lower middle, 1 m/s), and rainfall bias in the equatorial American and African sectors (lower left and right panels, respectively, 1 mm/day). Data is	

averaged over 2°S-2°N in all panels. Wind is from the 1000 hPa level in model simulations. The GPCP rainfall climatology is for the 1979-2005 period.	45
Figure 3.2 Precipitation (left, 1 mm/day) and diabatic heating (right, 0.5 K/day) distribution over tropical South America in observations and CAM3 simulation during March-May. Observationally derived fields are in the top panels, CAM3 ones in the middle, and the CAM3 bias (e.g., CAM3-ERA-40) in the bottom panels. The mass-weighted vertical average (175 hPa to the surface) of heating is displayed. The marked rectangle in the bottom panels indicates the tropical region whose influence is subsequently investigated.....	48
Figure 3.3 Observed and diagnostically simulated March-May surface circulation (zonally asymmetric part) in the Pacific and Atlantic sectors: Sea-level pressure and 1000 hPa winds from ERA-40 reanalysis are shown in the upper panel, while their simulation from the SLPE model is shown in the lower panel, using the same contour interval and vector scale. The SLPE model is forced by orography, 3D diabatic heating, and submonthly thermal and vorticity transient fluxes, all obtained/diagnosed from the ERA-40 reanalysis. Wind vectors are not plotted when the wind speed is less than 1 m/s, and values over land are masked out prior to computation of the zonally-asymmetric component.	51
Figure 3.4 CAM3's surface circulation <i>bias</i> (upper panel) and its diagnostic simulation (lower panel): The zonally asymmetric part of sea-level pressure and 1000 hPa winds is shown, as in Figure 3.3. The diagnostic simulation is obtained without thermal and mechanical transient forcing bias. The SLP contour interval and wind vector scale are indicated in the title line. Positive SLP bias is shaded red.....	52
Figure 3.5 Diagnostic analysis of CAM3's March-May surface circulation <i>bias</i> : From (a) global tropical (15°S-15°N) heating bias; (b) tropical South American (marked box) heating bias; (c) tropical South American <i>continental</i> heating bias; and (d) synthetic continental heating bias. The latter is obtained by multiplication of vertically averaged heating by the average heating profile over tropical South American land. SLP contour interval (half of Figure 3.4) and wind vector scale are indicated in the title line. Vector scale in the top panel is twice as large as in the rest. Bias vectors of less than 0.2 m/s wind speed are not plotted. Positive SLP bias is shaded red.....	55
Figure 3.6 Diabatic heating profiles over the tropical South American region: Average profile over the continental (oceanic) region of the box marked in Figure 3.5 is displayed in the left (right) panels. Both observationally constrained (ERA-40 residual diagnosis, blue) and CAM3 simulated (red) profiles are shown, along with the CAM3 bias (green).....	57
Figure 3.7 Diagnostic analysis of CAM3's March-May surface circulation <i>bias</i> (contd.): Bias forced by synthetic heating over the tropical South American continent (land in the marked box), consisting of only the (a) CAM3 heating <i>amount</i> bias, and (b) CAM3 heating <i>profile</i> bias. Rest as in Figure 3.5.....	58
Figure 3.8 Equatorial surface zonal wind (left panel) and tropical precipitation (right) biases in a CAM3 development simulation (Richter-Neale deep convection, see	

footnote 1 for more details). CAM3's precipitation bias in an expanded tropical sector is also shown to facilitate comparison. Rest as in Figure 3.1.....	60
Figure 3.9 Diagnostic analysis of CAM3's March-May surface circulation <i>bias</i> from tropical African continental heating bias. Rest as in Figure 3.5.	62
Figure 3.10 Diabatic heating profiles over the tropical South America and <i>tropical Africa</i> : Average profile over the continental region of the box marked in Figure 3.5 (Figure 3.9) is displayed in the left (right) panels. Both observationally constrained (ERA-40 residual diagnosis, blue) and CAM3 simulated (red) profiles are shown, along with the CAM3 bias (green).....	63
Figure 4.1 EOF patterns and the corresponding PCs. From original SSTA: EOF patterns of spring meridional mode (a) and summer equatorial mode (b), and their PCs (c). From ENSO-influence-removed SSTA: EOF patterns of spring meridional mode (d) and summer equatorial mode (e), and their PCs (f). Contour intervals for a, b, d, and e: 0.05°C.....	71
Figure 4.2 Regression (contours) between MAM PC1 and March-April South American rainfall (a); and between JJA PC1 and July-August West African rainfall (b). Shading indicates significant correlation (above 95% level). Contour levels: 3 mm/day.	73
Figure 4.3 Real monthly SST anomaly patterns, March through August, in year 1958 (left panel) and 1974 (right panel).....	75
Figure 4.4 Regression maps (contours) of meridional winds onto MAM PC1 (left panel), and onto JJA PC1 (right panel). Shading indicates significant correlation (above 95% level).	77
Figure 4.5 Regression maps (contours) of zonal winds onto MAM PC1 (left panel), and onto JJA PC1 (right panel). Shading indicates significant correlation (above 95% level).	79
Figure 4.6 Regression maps of SST anomaly (contours) onto the May west-equatorial zonal winds. Shading indicates significant correlation (above 95% level). Contour intervals: 0.1°C.....	81
Figure 4.7 Regression maps (contours) of SSTs onto MAM PC1 (left panel), and onto JJA PC1 (right panel). Shading indicates significant correlation (above 95% level).....	83
Figure 4.8 Regression maps of monthly zonal winds (black contours) and monthly rainfall (green/yellow shading) onto the MAM PC1.....	85
Figure 4.9 Lead-lagged correlation between the west equatorial zonal winds and the a) June and b) July eastern equatorial SST.	87
Figure 4.10 Regression (contours) between African rainfall (2-month-averaged) and MAM PC1 (left panel), and between African rainfall and JJA PC1 (right panel). Shading indicates significant correlation (above 95% level). Contour intervals: 0.3 mm/day.	90
Figure 4.11 a) West African rainfall climatology: contours: annual mean; vectors: amplitude and phase of the first harmonics of climatology. The vectors point to the	

time when the peak of the annual cycle of climatology occurs. b) Area averaged climatology of the box in a); unit: mm/day. c) Area-averaged monthly standard deviation of the box; unit: mm/day.....	91
Figure 4.12 Time series of the spring dipole PC (blue) and the summer zonal PC (red) and the index of Jul-Aug rainfall anomaly of Guinea Coast (black): a) original, b) de-trended.....	92
Figure 4.13 Power spectrum of spring dipole PC (blue) and summer zonal PC (red).	97
Figure 4.14 Time evolution of a) warm events and b) cold events at the equator. Only warm anomalies warmer than 0.4 °C and cold anomalies colder than -0.4 °C are included in the calculation.	100
Figure A.0.1 EOF patterns and the corresponding PCs, from original SSTA: EOF patterns of the second and third modes in spring (a and d, respectively) and in summer (band e, respectively), and their PCs (c and f). Contour intervals for a, b, d, and e: 0.05 °C.....	104
Figure B.0.2 Regression (contours) maps between the three-month-averaged SSTA onto the PCs derived from the original SSTA. Contour intervals: 0.1 °C. Correlation significance above 95% level are shaded.....	107
Figure B.0.3 Regression (contours) maps between the three-month-averaged SSTA onto the de-trended PCs derived from the ENSO-removed SSTA. Contour intervals: 0.1 °C. Correlation significance above 95% level is shaded.....	108

Table of Acronyms

AGCM	atmospheric general circulation models
CAM(3)	Community Atmosphere Model (version3)
CCSM(3)	Community Climate System Model (version 3)
DJF	December-January-February
ENSO	El Nino and Southern Oscillation
EOF	Empirical Orthogonal Function
GCM	general circulation models
ITCZ	Intertropical Convergence Zone
JJA	June-Jule-August
MAM	March-April-May
NAO	North Atlantic Oscillation
PC	Principal Component
SLP	sea level pressure
SON	September-October-November
SSH	sea surface height
SST	sea surface temperature
SSTA	sea surface temperature anomaly
WES	wind-evaporation-SST

1. Introduction

Tropical Atlantic is clamped by the South America (the Amazon) in the west and Africa (the Sahel) in the east. These two regions are known to be undergoing significant climate/environment changes for decades: deforesting and increasing biomass burning over the Amazon (cf. Skole and Tucker 1993) and the long-term drought over the Sahel (cf. Le Barbe et al. 2002). Tropical Atlantic climate has been shown to be coupled with the climate of these surrounding continents, and therefore understanding the tropical Atlantic climate variability is important in terms of its strong societal/economical impacts on the countries of these continents. While many observational studies can be (or have been) employed, climate modeling studies are another alternatives to investigate the impacts of these climate/environment changes. However, climate models have been shown to be highly deficient in reproducing reasonable seasonal climate of the tropical Atlantic, degrading the feasibility and credibility of further forecasting on the changes and the impacts.

In this dissertation, some systematic bias structures of a state-of-the-art climate model, CCSM3, will be discussed. Possible causes of one of the important biases will also be proposed and verified. Before we talk about the biases, we need to understand the observed climate of this sector.

1.1. Climate in the Tropical Atlantic sector

Here I begin with a brief review of the observed mean state and seasonal cycle of Atlantic climate. The mean state of the climate in the tropical Atlantic sector is characterized by a Hadley circulation in the atmosphere, with winds blowing towards the

equator at lower levels (below 500mb) and poleward at upper 200mb levels. At lower levels the winds are easterly due to conservation of angular momentum. Along the equator these easterly surface winds also represent the lower branch of the zonal-vertical Walker circulation, whose ascending motion is located over the Amazon and whose descending motion occurs broadly over the eastern Atlantic Ocean. The deep Tropics are with the Intertropical Convergence Zone (ITCZ), where strong atmospheric convection and precipitation occur, caused by convergent Hadley circulation flows at the surface. The superposition of the Hadley and Walker circulations leads to strong descending motion in the east subtropical region and produces a temperature inversion and stable atmospheric conditions, which in turn lead to the formation of the stratiform clouds (Klein and Hartmann, 1993). Stratiform clouds reduce the solar insolation and further cool the sea surface temperature of the eastern basin.

The eastern ocean is cooler than the western ocean as a result of the large scale circulation of the ocean, and the resulting shallowing of the thermocline in the east. Along the equator, easterly winds cause equatorial ocean upwelling. The easterly wind stresses acting on the ocean are balanced by the slope of the sea surface height (SSH) from east and west. SSH is proportional to the depth of the thermocline as a result of weak circulation in the deep ocean. Consequently the thermocline shoals in the east along the equator by 150m. This shoaling of the thermocline in the east brings cold deep water to the surface. As a result, the equatorial ocean surface has westward gradient of SST for much of the year. The zonal slope of SSH also drives a strong eastward Equatorial Undercurrent below the wind-driven surface layer, which flows near the depth of the thermocline.

Superimposed on this mean state, the climate of the tropical Atlantic varies strongly seasonally, with weaker, but important year to year variability.

a. Seasonal cycle

The origins of the seasonal cycle in this sector are linked to the proximity of continental convective zones and the geometry of the eastern boundary (Mitchell and Wallace, 1992; Xie, 1994; Chang and Philander, 1994; Nigam and Chao, 1996; Li and Philander 1996). The tropical Atlantic is flanked in the east by the West African continent, which extends to 10°W north of 3°N and supports a significant boreal summer monsoon. Convection over land is affected by the presence of an inland plateau which reaches heights of some 1km. The onset of the boreal summer monsoon in May following the northward shift of solar declination is associated with intensification of southeasterly trade winds along and south of the equator, a northward shift of the ITCZ and the associated intense convection.

The onset of the West African monsoon together with the enhanced southeasterly trade winds cool SST along the Africa coast and the equator, and form a pool of cool surface water, which is usually known as the equatorial cold tongue. The cold tongue appears along the equator (3°S-0°N) between 20°W-10°W in late-May and spreads southeastward to 10°S in the following season as a result of intensifying coastal upwelling, the southeastward propagation of coastal Kelvin waves that shallow the thermocline, the northwestward advection of cool surface water along the coast, and the reduction in solar isolation due to the shading by stratus clouds (Yu and Mechoso, 1999). At the same time, the intensifying winds cause a tremendous increase in mixing and entrainment bringing this cool water into the mixed layer and amplifying the effects of surface latent heat loss

(Foltz et al., 2003). The SST-induced anomalous pressure gradient at the western flank of the cold tongue enhances the easterly wind there. The enhanced wind produces extra cooling through equatorial upwelling to the west of the original cool SST anomaly, thus shifting the cool anomaly westward as envisioned in the “westward SST expansion” hypothesis (Mitchell and Wallace, 1992; Nigam and Chao, 1996; Okumura and Xie 2004). South of the equator the continent lies east of 10°E and in that hemisphere the boreal winter monsoon remains primarily confined to the continent (Xie and Carton, 2004).

In boreal late fall in response to increasing solar insolation in the Southern Hemisphere and weakening equatorial winds the equatorial thermocline becomes less steeply sloped. In the east the deepening of the thermocline reduces the temperature drop across the base of the oceanic mixed layer. The reduction in the temperature drop reduces the effectiveness of entrainment-induced cooling. In the southeast surface insolation reaches its maximum in January-February while latent heat loss remains close to its annual average. As a result, the heat content of the oceanic mixed layer increases throughout this season. In the Northern Hemisphere the increase in latent heat loss due to strengthening trade winds is partly compensated for by an increase in surface insolation due to reduced cloudiness. The result of these changes in mixed layer heating during December-February is that by March-April SSTs are uniformly warm throughout the tropical sector. As a result, the seasonal cycle of SST at the eastern equatorial region is strong in annual cycle with rapid cooling during June, July, and August and slow warming from September to May, as shown by Mitchell and Wallace (1992, **Figure 1.1**). Thus, March-April-May (MAM) and June-July-August (JJA) represent the warm and cool extremes of the seasonal cycle in this sector.

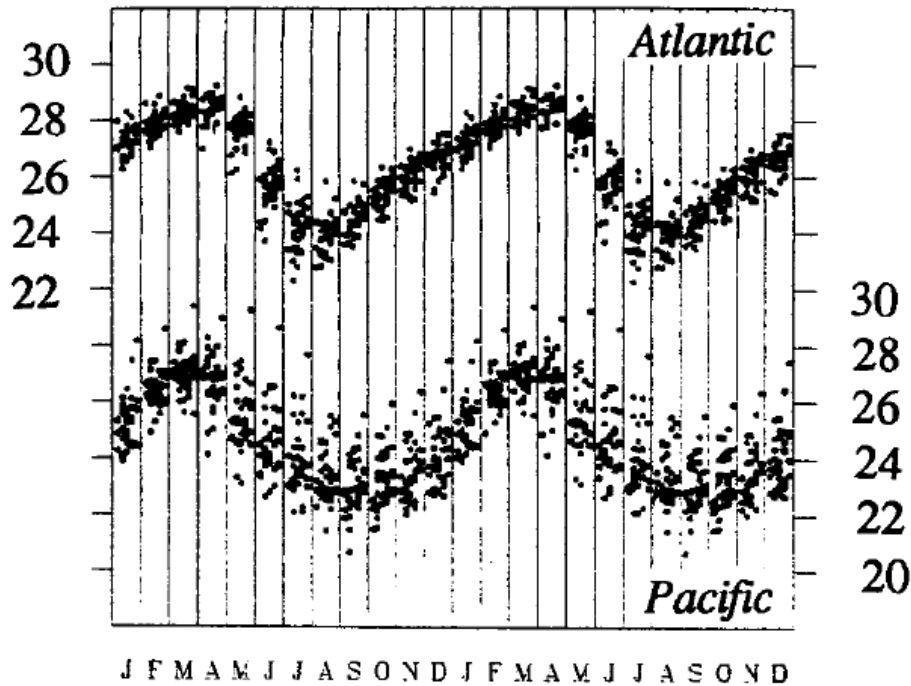


Figure 1.1 Scatterdiagram of monthly mean SST for the equatorial cold tongue region of Atlantic (4°S-4°N, 16°W-4°E) and the Pacific (4°S-4°N, 104-86°W) oceans. Unit: °C. (From Mitchell and Wallace 1992).

b. Tropical Atlantic Variability

As evident in **Figure 1.1**, interannual variability in the Atlantic is weaker in magnitude than the El Nino and Southern Oscillation (ENSO) variability of the Pacific. Nevertheless, the year-to-year climate variability of the Tropical Atlantic plays a critical role in influencing the climate of the adjoining continental regions, such as the rainfall variability in the Northeastern Brazil and West African region. Unlike the Pacific climate variability, which is dictated by a single dominant phenomenon, ENSO, Tropical Atlantic has several significant patterns of variability: (1) an equatorial mode (also known as the Atlantic Nino mode), (2) a meridional model (or interhemispheric mode), (3) remote influences from ENSO (Xie and Carton, 2004; Deser et al., 2006).

(1) Equatorial mode

During boreal summer when the seasonal equatorial thermocline in the eastern basin shoals due to upwelling (Carton and Huang 1984), the zonal trade winds along the equator relax in some years. This relaxation of the zonal trade winds, the corresponding southward shift of the ITCZ, and the weakening of the West African monsoon all occur in concert with a warming of the oceanic cold tongue and a deepening of the eastern equatorial thermocline. This conglomeration of events, known as Atlantic Nino or the equatorial mode in the literature, is reminiscent of El Nino in the Pacific, but weaker in magnitude, more seasonally locked to boreal summer, and more frequent (Xie and Carton, 2004; Ruiz-Barradas et al., 2000).

Like ENSO in Pacific, this mode is highly associated with a zonal wind anomaly in the western equatorial region (Zebiak 1993). Zonal wind anomalies lead to the changes in the thermocline depth in the eastern equatorial basin via the eastward-moving equatorial Kelvin waves, and cause a corresponding warming (or cooling for the opposite phase) of the surface and the mixed layer over the equatorial basin, and especially along the Coast of Guinea (Carton and Huang 1984). The warm water in the equatorial region due to Atlantic Nino sometimes can flow southward along the Benguela coast, resulting in a warming event in that region, which is one of the causes of the development of the “Benguela Nino” (Hagen et al., 2001). The equatorial mode is particularly highly related to interannual variability of summer rainfall over the Guinea Coast (Hirst and Hasternrath 1983; Giannini et al. 2003) as the peak season of this mode overlaps greatly with the African monsoon season.

(2) Meridional mode

In contrast to the cool season Atlantic Nino, in boreal spring, when the seasonal SSTs are warmest and most homogeneous near the equator, the latitudinal position of the ITCZ is sensitive to small changes in the interhemispheric gradient of SST due to the uniformity of SST (Ruiz-Barradas et al., 2000; Chiang et al 2002; Kushnir et al 2002; Xie and Carton 2004). During this sensitive season a southward gradient of anomalous SST induced either by local air-sea interaction or by remote influence from the Pacific can push the ITCZ southward, strengthening the northeast trade winds along the equator, weakening the southeast trade winds, and shifting convection southward as well (Xie and Carton, 2004).

The meridional mode, sometimes called the dipole mode, represents a concurrence of a strong cross-equatorial SST gradient, cross-equatorial flow, and the latitudinal movement of the ITCZ (Ruiz-Barradas et al. 2000). This mode is also often associated with a dipole pattern of SST anomaly (SSTA) with opposite signs of anomalies across the equator (Chang et al. 1997), although whether it is a statistical artifact is still under debate. Positive feedback between wind, evaporation, and SST (WES feedback) is responsible for the occurrence and existence of this mode (Chang et al. 1997). This mode has a great influence on the spring rainfall over Nordeste of Brazil (Moura and Shukla 1981).

(3) Remote influence from ENSO

During the years when El Nino peaks in boreal winter in Pacific, sea level pressure (SLP) decreases in the subtropical Atlantic and increases in the equatorial Atlantic a few (3~5) months after the ENSO peaks. The resulting anomalous southeasterly winds due to the anomalous pressure gradient weaken the northeast trade winds and lead to a delayed

warming of the ocean mixed layer. During an El Nino event, the Northwest Atlantic SST warms anomalously because of suppressed heat flux due to the reduced difference in air-sea temperature and to high humidity (Saravanan and Chang 2000; Chikamoto 2002); ITCZ rainfall also is reduced because of stronger than normal subsidence over the tropics while the ITCZ moves northward as an indirect response to the warmer SST to the northwestern Atlantic (Yulaeva and Wallace 1994; Saravanan and Chang 2000). Because ENSO is phase-locked with seasons, the influence from ENSO on Atlantic has substantial seasonality being strongest in the boreal spring and weakest in the boreal fall (Enfield and Mayer, 1997; Xie and Carton, 2004).

1.2. Modeling of the Tropical Atlantic climate

Although the climate of the tropical Atlantic Ocean is simple in that it is strongly seasonal, this strong seasonality has proven remarkably difficult to simulate (Davey et al., 2002; Deser et al., 2006). Most models have difficulties reproducing the observed eastern equatorial cold tongue in boreal summer, with reversed SST gradient along the equator. Many models tend to simulate weaker equatorial easterly in boreal spring. In the intercomparison study, Davey et al. (2002) show that for most of the coupled general circulation models (GCMs), for the annual mean values, the simulated zonal equatorial SST gradient is opposite to its observed direction, and the zonal equatorial wind stress is too weak. Coupled models also produce too abundant precipitation to the south of the equator during boreal spring, leading to a spurious double-ITCZ in the annual mean (Breugem et al. 2006; Deser et al. 2006; Stockdale et al. 2006; Richter and Xie 2008). Besides the warm bias in the eastern equatorial region, a more pronounced warm bias occurs in the southeastern basin, a bias also seen in the southeast Pacific, which is likely

due to models' deficiency in coastal upwelling and maritime stratus clouds (Yu and Mechoso 1999; Large and Danabasoglu 2006; Huang et al. 2007).

While coupled ocean-atmosphere feedbacks undoubtedly play a role in producing the above biases, previous studies have shown that uncoupled atmospheric GCMs with prescribed climatological SSTs also suffer significant biases (Richter and Xie 2008). Many atmospheric GCMs also underestimate the equatorial easterly winds (Okumura and Xie 2004). Biasutti et al. (2006) find that atmospheric GCMs tend place the ITCZ southerner than observed, which is likely related to a tendency to place the maximum rainfall over the SST maximum while observations place it over the surface convergence maximum. Richter et al. (2007) show that atmospheric GCM simulation of the South Atlantic anti-cyclone can be affected by the precipitation biases over tropical South America and Africa.

As pointed out earlier the meridional mode tends to happen in boreal spring when the seasonal SSTs are most homogeneous in latitude, while the equatorial mode occurs in boreal summer when the equatorial thermocline is most shallow in the east; in other words, the mean state can influence the ocean-atmosphere feedback and further affects the climate variability. The failure of coupled GCMs to simulate a realistic seasonal climate degrades their ability to produce reasonable seasonal-to-interannual SST and precipitation anomalies, and deteriorates the models' skill in prediction of the climate variability. It also downgrades the feasibility and credibility of long-term projections for the region under climate forcing scenarios (Breugem et al. 2006; Deser et al. 2006; Stockdale et al. 2006). It is therefore important to investigate the causes of GCM biases of the seasonal climate in the tropical Atlantic and to work toward their elimination.

In this dissertation the bias of the seasonal climate of a state-of-the-art climate GCM and of its atmospheric component model are investigated in Chapter 2, which shows that model biases project on the spatial pattern of the climate variability modes. Possible causes of the biases are proposed. In Chapter 3, a diagnostic model is used to test a hypothesis for the spring-time westerly bias in the coupled/atmosphere models discovered in Chapter 2. Chapter 4 is an observational diagnosis study of the relationship between the two dominant modes of the interannual variability, which was originally triggered by the relationship in the two major model bias patterns revealed in Chapter 2.

2. Seasonal Climate of the Tropical Atlantic Sector in the NCAR CCSM3: Error Structure and Probable Causes of Errors¹

2.1. Introduction

The CCSM project has developed since the 1990s to provide a tool for examining climate variability (Boville and Gent, 1998). SSTs in the original version (CSM1) showed errors of 1-3°C in the southeastern tropical Atlantic, but with near-climatological SSTs in the north. Like many of the coupled models described in Davey et al (2002) CSM1 had similar SST errors in the tropical Pacific. The latest version of CCSM, CCSM3, is designed to address a number of deficiencies in the original model (Collins et al., 2005a) and some errors are substantially reduced, particularly in representation of ENSO variability. However, examination of the mean climate of CCSM3 by Deser et al (2006) highlights some persistent problems in the tropical Atlantic. These include cold tongue SSTs that are 3°C too warm (26°C), Caribbean Sea SSTs that are 1°C too cold, a southward displacement of the ITCZ notably in boreal winter, and an absence of year-to-year variability along the equator (the Atlantic Nino). Deser et al. (2006) suggest that these problems may be traced back to the poor simulation of the West African monsoon by the atmosphere model (known as CAM3) even when forced by observed SST.

The problem of tropical bias in CCSM3 has also been discussed by Large and Danabasoglu (2006) in the context of the ocean's influence on the coupled model. Although primarily focused on the mean climate and the seasonal cycle in the tropical

¹ The work of this chapter is published: Chang, C.-Y., J. A. Carton, S. A. Grodsky, and S. Nigam, 2007: Seasonal climate of the tropical Atlantic sector in the NCAR Community Climate System Model 3: Error structure and probable causes of errors. *J. Climate*, 20, 1053–1070.

Pacific, Large and Danabasoglu examine an interesting experiment in which ocean temperature and salinity in the southeastern boundary regions of an enhanced resolution (T85) version of CCSM3 are returned to their observed climatological values, but the model is unconstrained otherwise. The result of this experiment was a reduction of eastern ocean temperatures, closer to those observed. A subsequent ocean-only experiment led the authors to suggest that the cause of the warm bias in the southeastern tropical oceans could be traced back to inadequate coastal upwelling close to the coast – that is, they suggested the cause was primarily contained in the ocean model.

DeWitt (2005), using ECHAM4.5 atmospheric GCM and MOM3 ocean GCM, shows in the ocean-only/coupled model study that the weak zonal wind stress along the equatorial may be the cause of the appearance of an incorrect zonal equatorial SST gradient. In another ocean-only/coupled model study, Hazeleger and Haarsma (2005) show that increasing the efficiency of wind-driven vertical mixing results in a deeper thermocline depth and higher SST, thus offering another explanation for the SST bias. Yu and Mechoso (1999) suggest that the source of the model bias lies in improper representation of low-level clouds over the eastern tropical oceans.

2.2. Model and data

a. The CCSM3 coupled model

The CCSM3 data used in this study are the output data of the “20th Century Climate in Coupled Models” project conducted for the Intergovernmental Panel on Climate Change. The output data are archived at the Program for Climate Model Diagnosis and Intercomparison website. Our study uses the case b30.030a (20C3M run1). This simulation was initiated on January 1, 1870 and integrated until December 31, 1999. This

is a simulation forced by historical ozone, solar, volcanic, green house gases, and sulfur dioxide/trioxide forcings with carbon distribution linearly scaled to population. Our analysis focuses on data for the final 50-year period beginning January 1950. A sensitivity examination has been carried out to ensure that the climatology of this particular case is similar to that of other cases and to that of the ensemble. The data are simulated based on the configuration of CCSM3 with atmosphere and land models (CAM3 and CLM3) and ocean and sea-ice models (POP1.4.3 and CSIM5). These models are connected to a flux coupler individually, and can only exchange data with the coupler. Fluxes exchanged among component models were not adjusted during this simulation.

b. The atmosphere component model: CAM3

The atmosphere model (CAM3) is based on the Eulerian spectral dynamical core with triangular spectral truncation at 85 wavenumber (T85, approximately 1.41° zonal resolution) and 26 levels (Collins et al., 2006a, b). In CAM3, a prognostic cloud parameterization replaces the diagnostic parameterization used in previous versions. Different evolution equations are applied for liquid and ice condensate. The new radiative parameterizations allow shortwave and longwave radiation to interact with cloud geometry and with water vapor. A prescribed aerosol climatology is used in calculating aerosol's radiative effects on shortwave fluxes and heating rates. This is an important consideration in the northern tropical Atlantic where Saharan dust may alter the surface radiative flux by 30W/m^2 (Carlson and Benjamin, 1980). The calculation of the thermodynamic tendencies has been reformulated relative to earlier versions of CCSM to insure conservation of energy.

We also examine a CAM3 AMIP-run using the enhanced version of CAM3 (T85), with prescribed SST for the period 1950 through 2001. The SST data sets were constructed by concatenating global HadISST (Rayner et al., 2003) for the years 1950 to 1981 with the Reynolds et al. (2002) SST data set for years after 1981.

c. The ocean component model: POP1.4.3

The ocean model is based on POP1.4.3 primitive equation numerics (See e.g. Danabasoglu et al., 2006). The model grid has a displaced pole in order to resolve the Arctic Ocean and has a nominal horizontal resolution of 10×10 in the tropics, with 40 levels (10m resolution nearsurface). Vertical mixing of heat and momentum uses a modified K-profile parameterization, while horizontal mixing is parameterized as a diffusive process with constant diffusion coefficients. Surface boundary conditions of heat, freshwater, and momentum are provided by the flux coupler. Solar radiation is allowed to penetrate into the ocean with an absorption profile that varies spatially and monthly based on satellite-based estimates of chlorophyll concentration. An additional modification is included to simulate the effect on mixed layer heating of diurnal variations. The initial condition of the ocean model is the climatological January-mean potential temperature and salinity, but zero velocity (Danabasoglu et al., 2006).

d. Observational/Reanalysis Data

To evaluate the performance of CCSM3 and CAM3 we compare the results to observation-based climatological analyses of atmospheric and ocean winds/currents, and precipitation, atmospheric vertical motion, ocean temperature, and several surface variables (surface winds, SST, SLP, and net shortwave). A number of variables are available based on satellite measurements. Our SST observation data set is same

combination of SST data sets that are used for the CAM3 AMIP run (Rayner et al., 2003; Reynolds et al., 2002). Observed surface winds are available also in a $1^\circ \times 1^\circ$ grid from the Special Sensor Microwave Imager for the 13-year period, 1988-2000 (Atlas et al. 1996) and are patched with the QuikSCAT scatterometer winds (Graf et al., 1998) available mid-1999-2005.

For net shortwave radiation we rely on the UMD/SRB D1 monthly analysis of Pinker et al. (2001), which is available on a $2.5^\circ \times 2.5^\circ$ grid for the 12-year period 1983-2004. Precipitation is provided by the Global Precipitation Climatology Project Version 2 monthly precipitation data on a $2.5^\circ \times 2.5^\circ$ grid for the 27-year period 1979-2005 (Adler et al. 2003). The estimated random error ranges between 10%-30% in regions where precipitation amounts exceed 3 mm/day. In the Atlantic sector, Adler et al. (2003) suggest that the maximum precipitation in the ITCZ may be underestimated.

The remaining variables cannot be estimated from satellite data sets. For sea level pressure and vertical motion, we rely on the monthly mean of the NCEP/NCAR daily reanalysis of Kalnay et al. (1996), available for the full 50-year period of interest on a $2.5^\circ \times 2.5^\circ$ grid. Ocean currents and temperature are provided by the Simple Ocean Data Assimilation (V1.4.2) ocean reanalysis of Carton and Giese (2006), available for a period of 44 years (1958-2001) on a $0.5^\circ \times 0.5^\circ$ grid at 40 vertical levels.

As indicated in the Introduction, the climate of the tropical Atlantic is characterized by a cool season (JJA) and a warm season (MAM). Thus we focus our examination of CCSM3 and CAM3 on their performance in these two extreme seasons. The seasonal averages are computed by combining the monthly averages for the full records. Later it

will be of interest to carry out a spectral analysis. This is carried out by Fourier decomposition of the monthly averages.

2.3. Results

The presentations of the results are organized in the following way. In the first part of this section we address seasonal errors in atmospheric circulation and SST beginning with seasonal mean SST. We then examine tropical surface wind fields, which are additionally affected by the subtropical distribution of SLP. Errors in winds and SLP are also related to errors in vertical motion and diabatic heating, and so we present the seasonal distribution of precipitation. In the second part of this section we address processes implicated in the development of seasonal errors in SST variability, including radiative and thermodynamic fluxes and entrainment/mixing in the ocean.

a. CCSM3 SST

We begin by examining the spatial pattern of SST in the cool (JJA) and warm (MAM) seasons. In CCSM3 SST during JJA is too warm by 1-3°C in the southeast, with the zone of anomalous temperature extending westward from the coast of Africa and also along the equator (**Figure 2.1**). In the northern tropics SST is too cool throughout the year by 1-2°C. Along the equator in JJA SST is 1°C too cool in the west and too warm in the east by up to 3°C so that the zonal gradient of temperature is positive, in conflict with observations. During MAM the anomalously warm SST in the southeast persists, but is confined to a narrower zone within 10° of the southeastern boundary. The contrasting cool and warm biases in SST in the northern and southern hemispheres, which induce a southward shift of the trade wind systems and northward intensification in the gradient of

SLP, are reminiscent of one phase of the interhemispheric mode. Along the equator the cool bias in the west and the warm bias in the east contribute to a westward bias in the CCSM3 SLP gradient.

We begin by examining the spatial pattern of SST in the cool (JJA) and warm (MAM) seasons. In CCSM3 SST during JJA is too warm by 1-3°C in the southeast, with the zone of anomalous temperature extending westward from the coast of Africa and also along the equator (**Figure 2.1**). In the northern tropics SST is too cool throughout the year by 1-2°C. Along the equator in JJA SST is 1°C too cool in the west and too warm in the east by up to 3°C so that the zonal gradient of temperature is positive, in conflict with observations. During MAM the anomalously warm SST in the southeast persists, but is confined to a narrower zone within 10° of the southeastern boundary. The contrasting cool and warm biases in SST in the northern and southern hemispheres, which induce a southward shift of the trade wind systems and northward intensification in the gradient of SLP, are reminiscent of one phase of the interhemispheric mode. Along the equator the cool bias in the west and the warm bias in the east contribute to a westward bias in the CCSM3 SLP gradient.

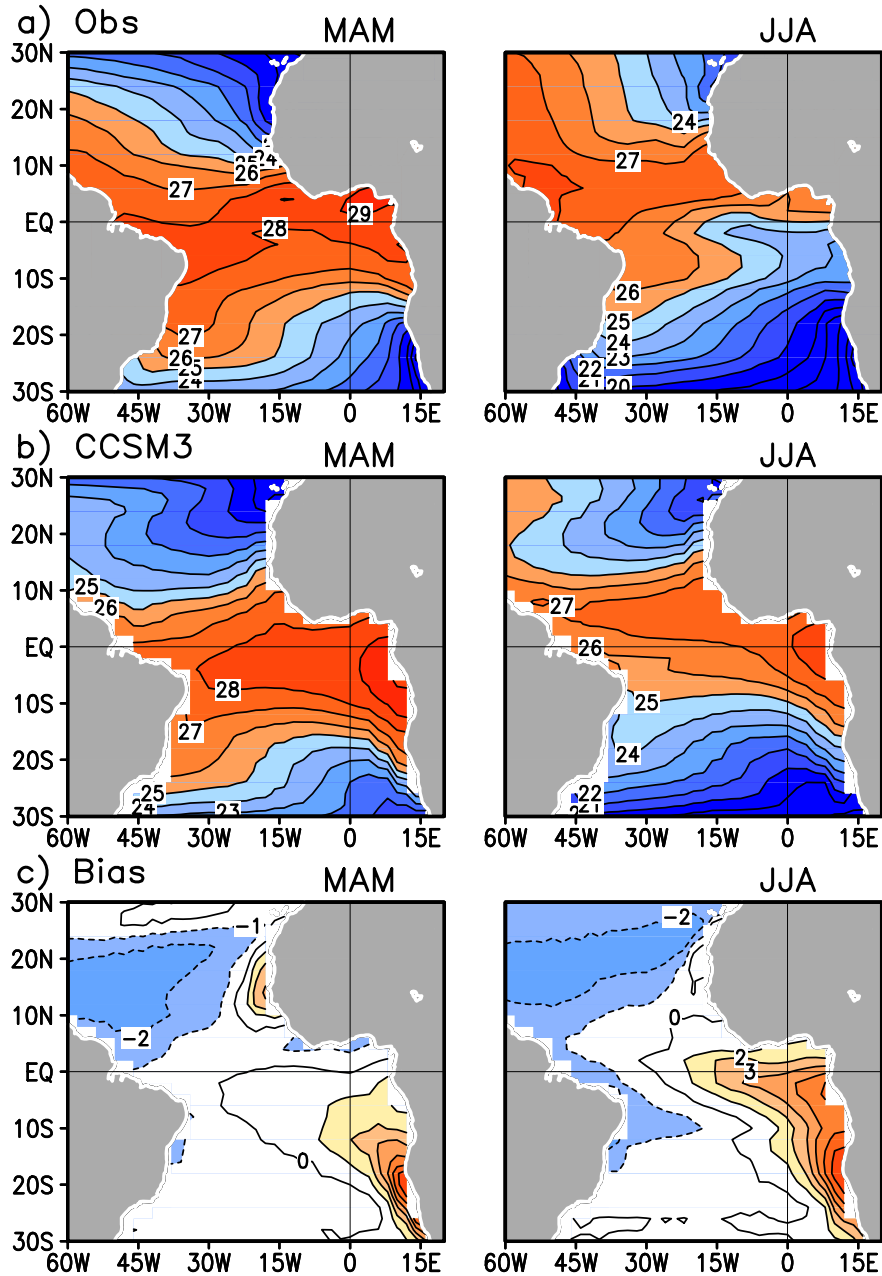


Figure 2.1 Seasonal SST. a) Observed; b) CCSM3; and c) SST bias (CCSM3-Obs). Contour interval: 1°C.

A climatology of SST along the equator shows that the cold tongue does not appear in CCSM3, while anomalies propagate eastward. The eastward progression of warm anomaly in the first half of the year has a higher speed than the cold anomaly in the

second half of the year (**Figure 2.2a**). To understand the nature of the seasonal cycle of SST along the equator we decompose monthly CCSM3 SST into its annual and semiannual harmonics (**Figure 2.2b**). The annual harmonic is similar in magnitude to the observations, but differs in fundamental ways. The CCSM3 annual harmonic appears first west of 30°W and progresses eastward, reflecting the eastward progression noted in **Figure 2.2a**. This result is in conflict with the observed annual harmonic, which appears first at the coast of Africa and progresses westward. The direction of progression of the annual cycle is projected by the direction of the anomaly progression in SST climatology, which is connected to the geographic location of the source (Africa in the case of the observation) and to the role of the trade winds in controlling mixed layer properties, as discussed in the Introduction. In CCSM3, westerly equatorial winds prevail in MAM (**Figure 2.2c**), thus inverting the processes leading to the observed westward development of seasonal winds and SST, but which in the model lead to eastward development of these variables. Another difference between the model and observation is the fact that CCSM3 has stronger summertime cooling in the western basin, whereas the observation show stronger cooling in the eastern basin. This difference may result from the thermodynamic effect of the stronger winds in the west during JJA in CCSM3 than in the observation, while the effects of entrainment are weaker in the east because the thermocline is too deep (**Figure 2.3c**).

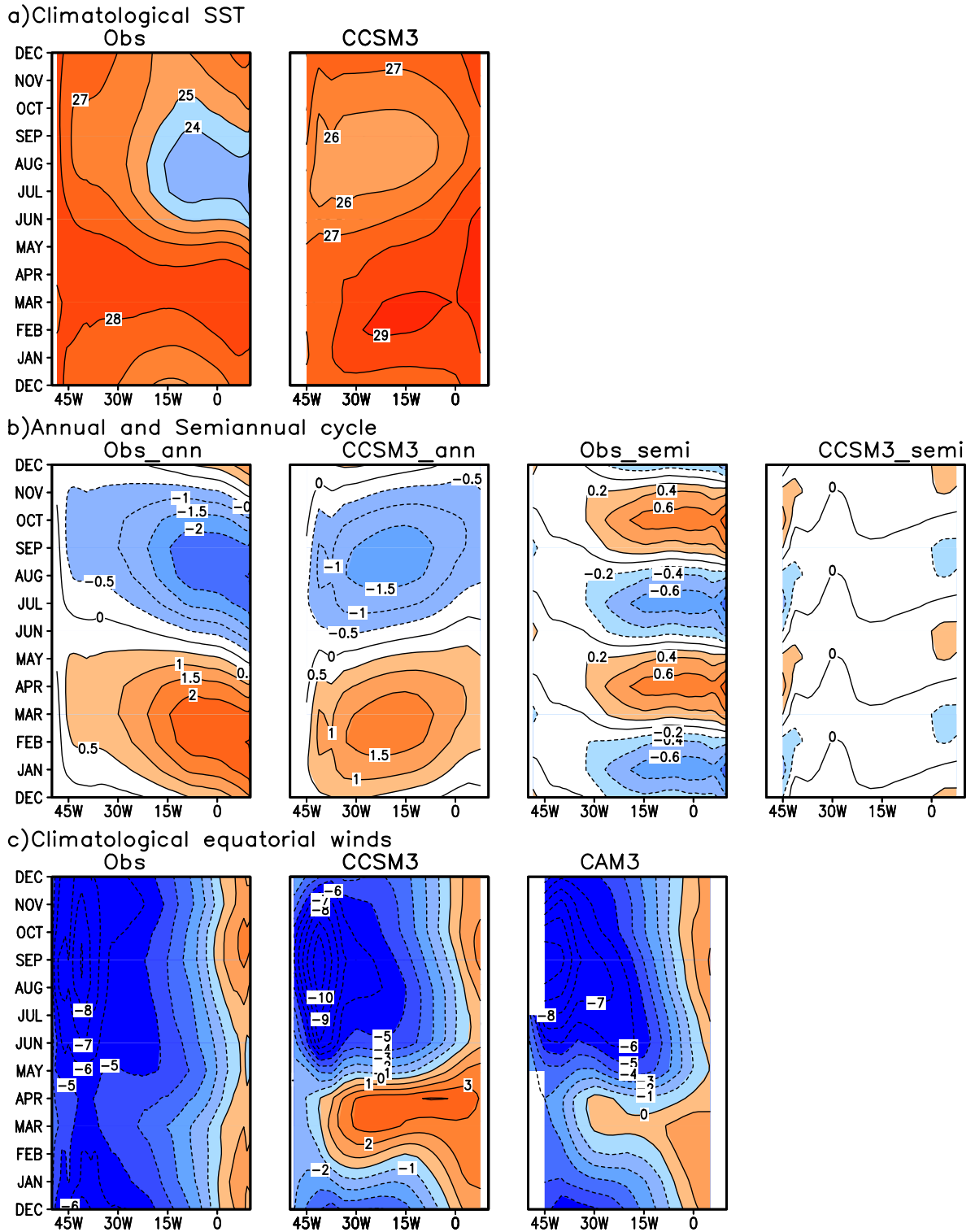


Figure 2.2 Observed and CCSM3 equatorial SST and zonal winds (averaged from 4S to 0N) versus longitude. a) SST; b) Annual and semiannual harmonics of SST. Unit: °C. c) Observed, CCSM3 and CAM3 zonal winds. Contour interval: 1 m/s.

The observed seasonal cycle of SST also has a significant semiannual harmonic (**Figure 2.2b**), with coldest SSTs in January and July. The most important factor governing the semiannual cycle is a response to the semiannually changing insolation. However, at least two additional factors contribute to this harmonic. One results from the semiannual increase in insolation over equatorial Africa (in March and September) increasing air temperature and lowering SLP. Lower SLP results in anomalous southerly winds that lead the cooling of the SST through coastal upwelling a month or two later. The second factor is the suddenness of the entrainment of cool subthermocline water into the observed mixed layer in June-July, which thus projects onto the semiannual harmonic with peaks in June-July and December-January. In comparison to observations, the CCSM3 thermocline (**Figure 2.3c**) in the eastern basin is too deep by 20-40 m throughout the year. This error increases the thermal inertia of the mixed layer and prevents the seasonal entrainment of cool subthermocline water. As a result the mechanisms giving rise to the observed semiannual harmonic in SST do not contribute to CCSM3.

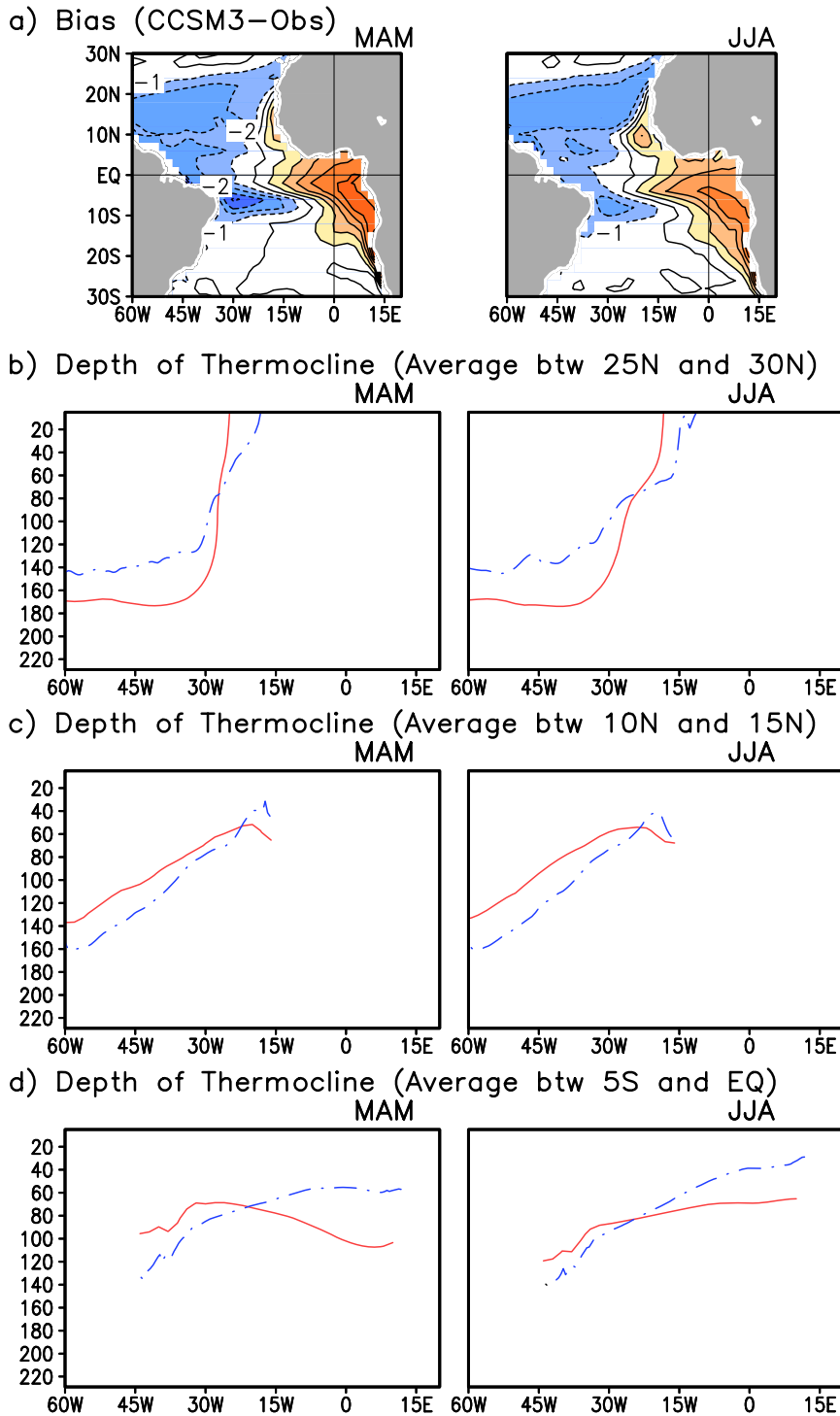


Figure 2.3 Seasonal CCSM3 ocean heat content bias and depth of thermocline. a) Bias in averaged upper ocean temperature (averaged 5m-96m). Contour intervals: 1°C. b), c) and d) Depth of the thermocline (as indicated by the depth of the 20C isotherm) in northern tropical Atlantic (averaged 25°N-30°N and averaged 10°N-15°N) and equatorial area (averaged 5°S-0°N) for CCSM3 (red, solid line) and observed (blue, dashed line). Unit: m.

b. Surface Winds and Sea Level Pressure (SLP)

The persistent anomalous meridional dipole pattern in CCSM3 SST occurs in conjunction with a cross-equatorial pressure gradient, shifting the latitude of the trade wind systems southward by 5-10° in the warm season (**Figure 2.4**). This southward shift causes the northeast trade winds to cross south of the equator giving a strong 3m/s northerly wind anomaly along the equator. At the same time the southeast trade winds become stronger between 25°S-5°S resulting in intensified convergence in the displaced ITCZ and a stronger than observed Atlantic Hadley Circulation (the vertical branches of this circulation are discussed below). In the east, the strengthened southeast trade winds extend to the coasts of southern Angola and Namibia where they act to intensify the coastal upwelling that normally prevails along these coasts (Xie and Carton, 2004). As noted below, however, the impact of coastal upwelling on SST is mitigated by the anomalously deep thermocline which seems to result from the equatorial westerly winds and the consequent propagation of downwelling equatorial/coastal Kelvin waves.

The southward displacement of the ITCZ in MAM together with the related anomalous westward gradient of CCSM3 SLP (about 2mb across the tropical basin, **Figure 2.5c**) are associated with the appearance of an intense 5m/s westerly anomaly in the zonal trade winds at the surface (**Figure 2.4c**) and an easterly anomaly at 200mb (not shown). The westerly anomaly of the zonal trade winds along the equator causes the winds to change direction so that westerly winds blow along the equator in MAM as shown in **Figure 2.2c**. These anomalous winds are indications of a greatly weakened (even reversed) Atlantic Walker Cell, with the weakening most intense north of the equator. The weakened Walker cell, in turn, is reminiscent of the warm phase of the Atlantic Nino except that the trade wind reversal occurs in CCSM3 every year during

MAM instead of every few years in JJA. As discussed in the Introduction, the southeasterly trade winds that prevail throughout most of the year along the equator in the Atlantic sector are in balance with an eastward SLP gradient. In CCSM3 the 3m/s westerlies that develop in MAM occur in balance with an anomalous westward SLP gradient. These westerlies force Ekman convergence and downwelling at the base of the ocean mixed layer along the equator, which in turn acts to reduce entrainment cooling of the mixed layer. The resulting warm SST bias in the eastern equatorial basin supports the westward SLP gradient and the westerly winds.

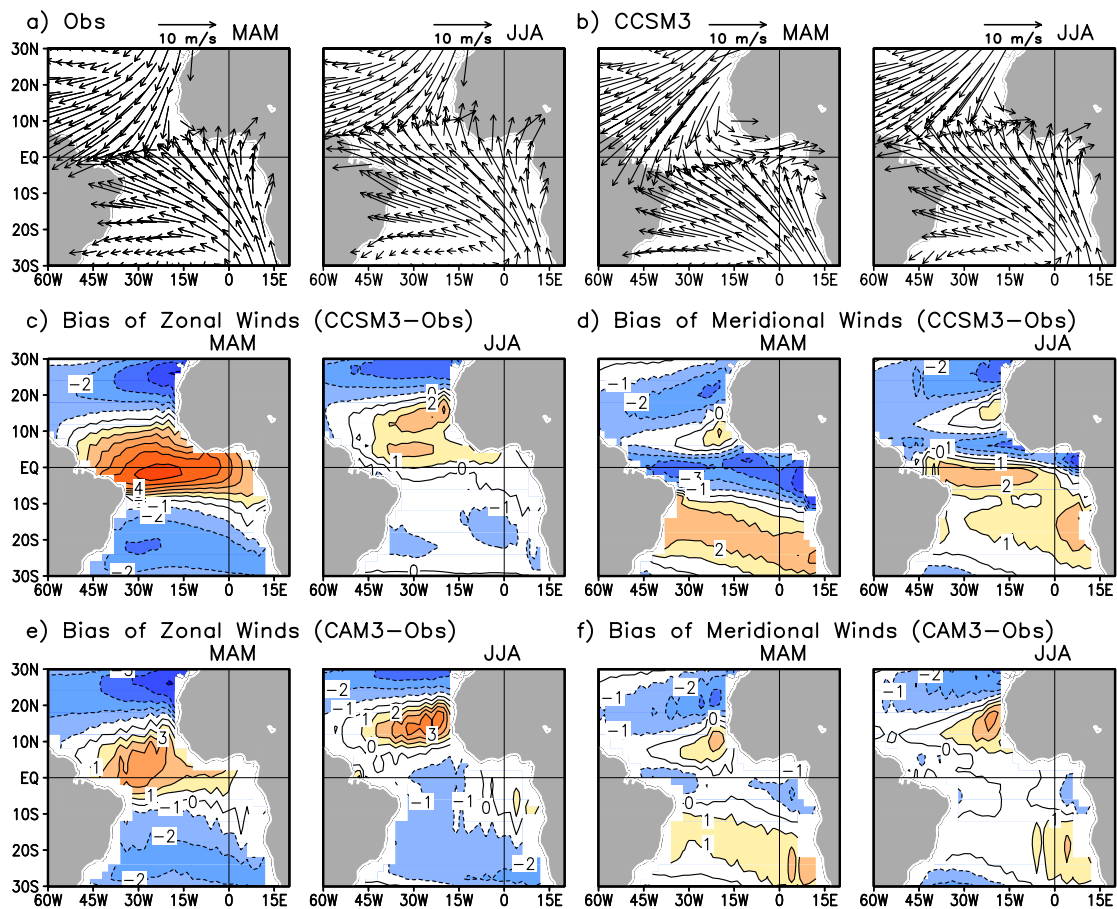


Figure 2.4 Seasonal surface winds. a) Observed; b) CCSM3; c) CCSM3 zonal wind bias; d) CCSM3 meridional wind bias; e) CAM3 zonal wind bias; f) CAM3 meridional wind bias. Contour intervals: 1 m/s.

To identify the causes of errors in surface winds we first attempt to separate those due to errors in internal atmospheric processes from those resulting from interactions with the ocean. We isolate the errors in internal atmospheric processes by comparing CCSM3 with CAM3 in which observed SSTs are prescribed. The CAM3 wind biases in Fig. 4e, f show similar (but weaker) patterns as that of the CCSM3 wind biases. Along the equator the anomalous westerlies in MAM occur even in the absence of errors in SST (that is, they appear in CAM3 as well as in CCSM3 but the strength is weaker). Examination of SLP and precipitation maps shows that the anomalous westerlies are connected with a weakened Walker circulation resulting from an imbalance in SLP along the equator (1-2mb excess pressure over the northern Amazon) (**Figure 2.5**). The weakening of the CAM3 Walker circulation along the equator does not occur in JJA; instead, it is slightly strengthened.

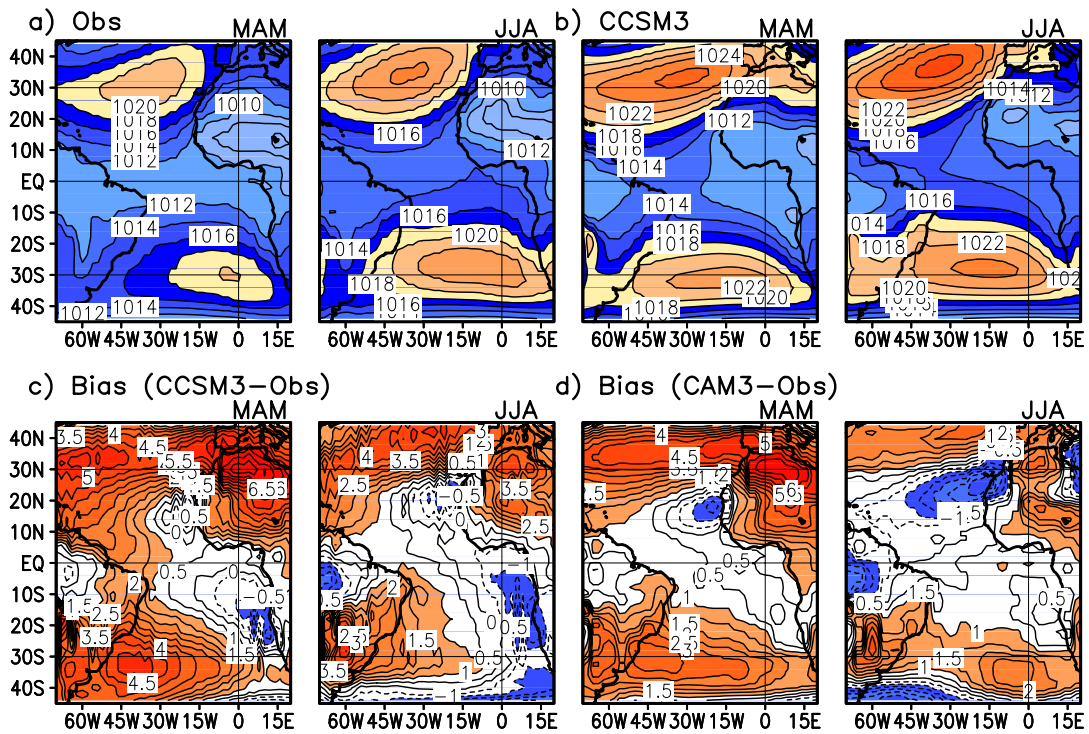


Figure 2.5 Seasonal SLP. a) Observed; b) CCSM3; c) CCSM3 bias; d) CAM3 Bias. Contour intervals: a) and b) 2 mb; c) and d) 0.5 mb.

Over the off-equatorial latitudes, the excessive trade wind strength in CCSM3 and CAM3 both reflect the presence of a persistent enhancement of the subtropical high pressure systems. The centers of the subtropical high pressure systems of both CCSM3 and CAM3 are slightly shifted northward in Northern Hemisphere, which is related to the negative bias of SLP over the West Africa coast (**Figure 2.5c, d**). This shift causes the southerly wind bias along the West Africa coast near 10°N, which in turn results in the SST warm bias in this area due to the decrease of coastal upwelling. In MAM the CCSM3 SLP error is largest in the North Atlantic sector reaching 4-5mb, with extensions eastward over northwest Africa and equatorward west of 40°W (**Figure 2.5**). During this season there are also substantial errors in SLP in the South Atlantic. In JJA the error is largest in the North Pacific, but still substantial in the North Atlantic.

c. Precipitation and Vertical velocity

One possible explanation for the positive bias in SLP in the subtropics is an anomalously intensified Hadley circulation. To diagnose the meridional-vertical circulation we focus on the meridional section at 0°E in CCSM3, which transects the eastern side of the oceanic cold tongue and crosses into the African continent north of 4°N. The vertical motion field (**Figure 2.6**) shows that descending motion in the subtropics is indeed too strong. In MAM the ascending motion associated with the ITCZ is substantially intensified with respect to the observed motion field with the largest velocity errors south of the equator occurring above 500mb. The intense convection is reflected in intense precipitation (**Figure 2.7**) and consequent diabatic heat release. In JJA convection extends too far northward onto the Northwest African continent in addition to being too intense and extending too high in the atmosphere.

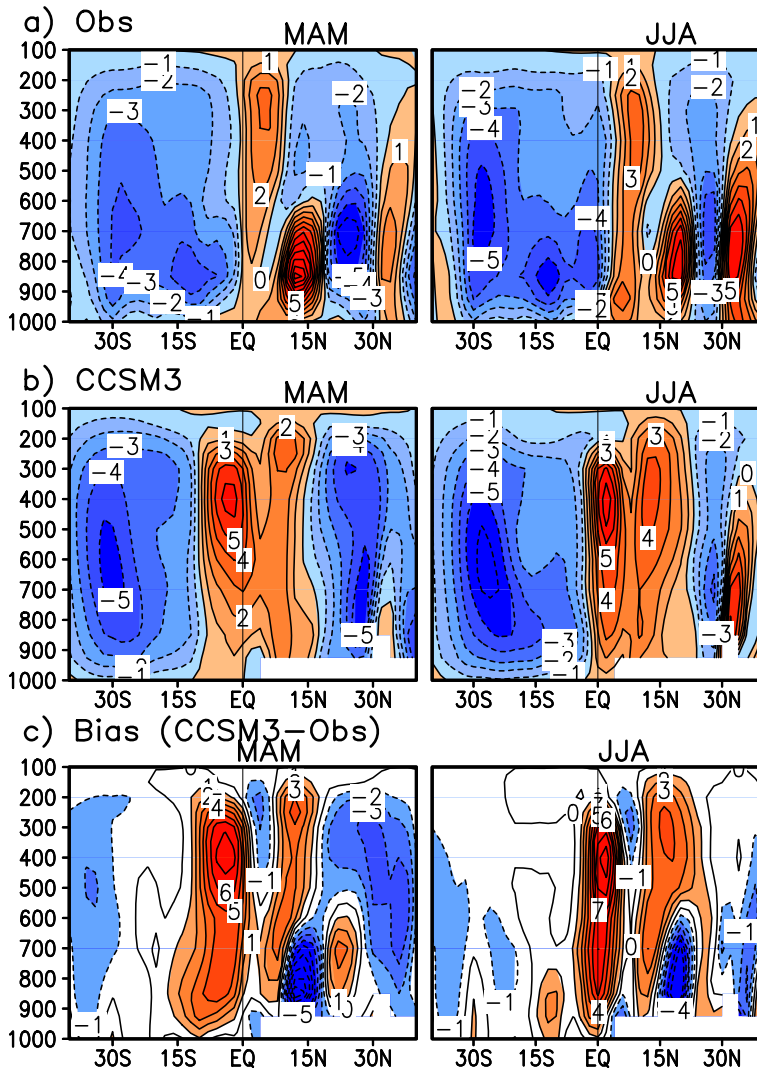


Figure 2.6 Seasonal atmospheric vertical velocity (negative omega) with latitude and height along 0°E. Red indicates ascending motion and blue descending motion. Contour intervals are 0.01Pa/s. a) Observed; b) CCSM3; c) CCSM3 bias.

The intense surface convergence due to the enhanced Hadley circulation in CCSM3 increases moisture convergence. Thus precipitation rates in the ITCZ during MAM (8mm/day) are 30% higher than observed values over the open ocean and even higher over Africa (**Figure 2.7**). On the other hand, the weakened Walker cell is reflected in the presence of insufficient precipitation over the Amazon and excess precipitation over West

Africa (**Figure 2.7**). This zonal dipole pattern of precipitation bias occurs in both MAM and JJA in CCSM3 when the Walker circulation along the equator is weakened. In CAM3 this dipole pattern only occurs in MAM, but not in JJA when the Walker circulation along the equator is instead stronger (**Figure 2.4e**). Clearly the rainfall biases at both continents bordering the tropical Atlantic are strongly associated with errors in the strength of the Walker cell.

We explore the coupled feedback between anomalous vertical motion and thus precipitation and anomalous SST by comparing precipitation in CCSM3 with CAM3 (**Figure 2.7**). Errors in precipitation are greatly reduced in CAM3 with prescribed SST. In MAM the excess rainfall in the southeast is reduced from 5-6 mm/day to 1 mm/day indicating that much of the source of precipitation error in this region, which is related to the southward displacement of the ITCZ, is associated with coupled interactions. On the other hand, over northwest Africa, between 10°N to 20°N, the rainfall is excessive in both CCSM3 and CAM3 and is produced by anomalously deep convection that isn't capped by descending flow aloft as it should be (**Figure 2.6**). The similarity of the errors in precipitation and SLP suggest that the causes should be traced back to the atmospheric models. A consequence of the additional soil moisture and cloud shading due to excess precipitation is colder surface air temperature in this region than observed (not shown) suggesting that the land surface model may play an important role as well.

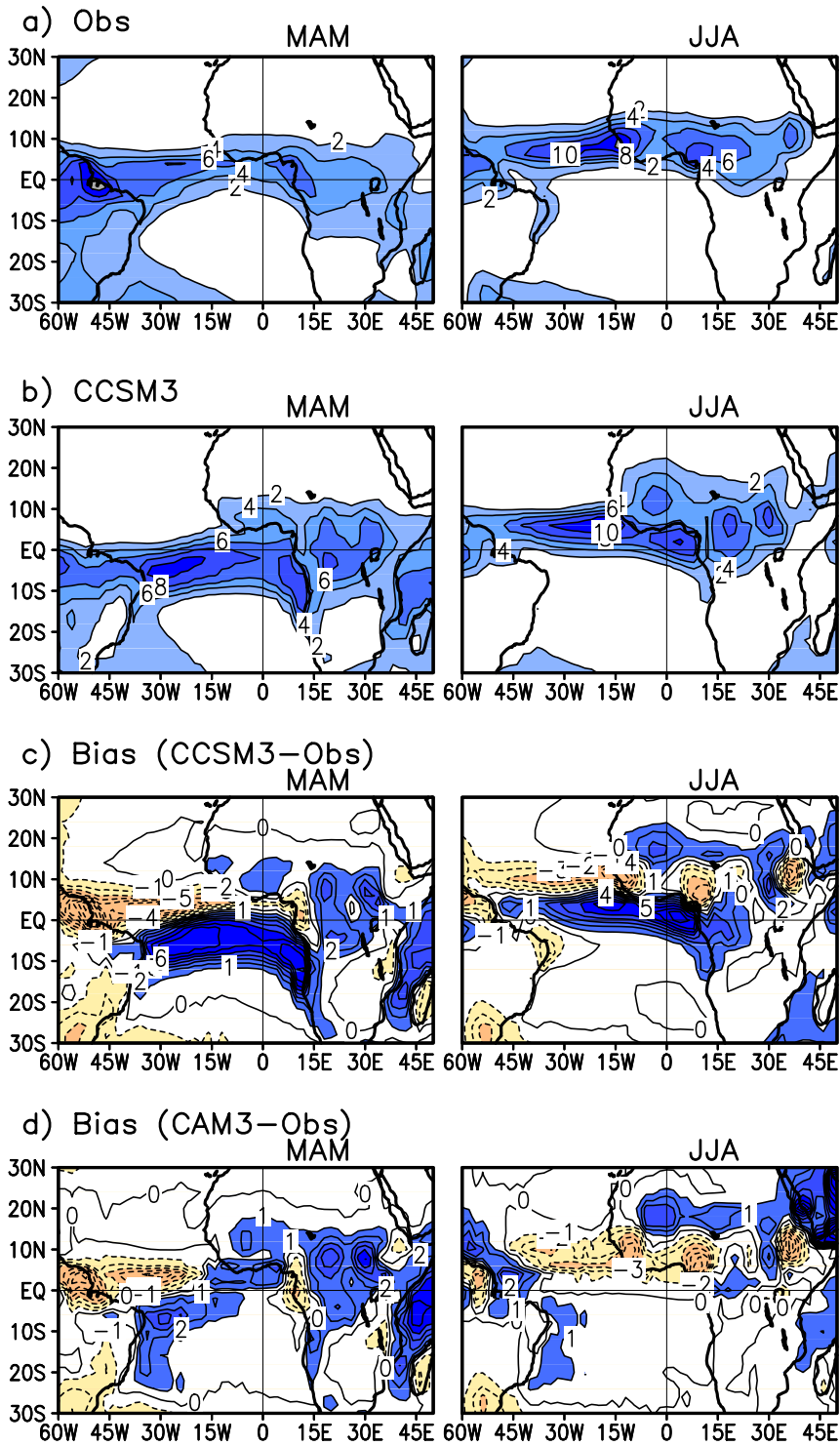


Figure 2.7 Seasonal precipitation. a) Observed; b) CCSM3; c) CCSM3 bias; d) CAM3 bias. Contour intervals are 2 mm/day for a) and b), and 1 mm/day for c) and d).

d. Surface Radiative Flux

North of the seasonal position of the ITCZ ($\sim 7^{\circ}\text{N}$) solar radiation in CCSM3 is reduced throughout the year by as much as $60\text{W}/\text{m}^2$ compared to observations (**Figure 2.8**). But the enhanced total cloud cover (not shown) is not associated with enhanced precipitation. The northeast trade winds are more intense north of 10°N (**Figure 2.4**) with enhanced upwelling to the north of the observed ITCZ and enhanced downwelling to the south (**Figure 2.9**). In the region of enhanced upwelling the thermocline is elevated by 10m (**Figure 2.3b**) and entrainment cooling is enhanced. This effect, together with the reduction in solar radiation and enhanced wind-induced thermodynamic surface fluxes are responsible for a $1\text{-}2^{\circ}\text{C}$ anomalous cooling of SST in this region. North of 20°N CCSM3 has stronger downwelling resulting in deeper thermocline and warmer heat content while SST has warm bias in MAM and cold bias in JJA, implying that wind-induced surface fluxes are more important. Very close to the coast of northwest Africa the trade winds weaken, reducing the upwelling that normally predominates in boreal summer.

CAM3 short wave radiation has a very similar bias pattern and strength to CCSM3 in the northern tropics, but differs in strength in the southern tropics. CAM3 has errors in simulating net surface short wave radiation due to errors in total cloud cover (not shown), which in turn may be due to the enhanced Hadley circulation. The deficiency of solar radiation may contribute to the cold SST bias. In CCSM3 close to the equator in the Gulf of Guinea net surface solar radiation is also too low by as much as $60\text{W}/\text{m}^2$ due to excessive clouds. However, the absence of solar radiation does not lead to cooling, suggesting that other terms in the mixed layer heat budget have been altered to compensate. Observational estimates suggest that entrainment/mixing should remove $50\text{-}100\text{W}/\text{m}^2$ from the mixed layer during JJA (Foltz et al., 2003). South of 10°S along the

coast of Africa solar radiation is close to its observed value, while we have already seen that the upwelling favorable winds are enhanced. But here the reduction in entrainment due to the anomalous deepening of the thermocline leads to an elevation of SST by several degrees.

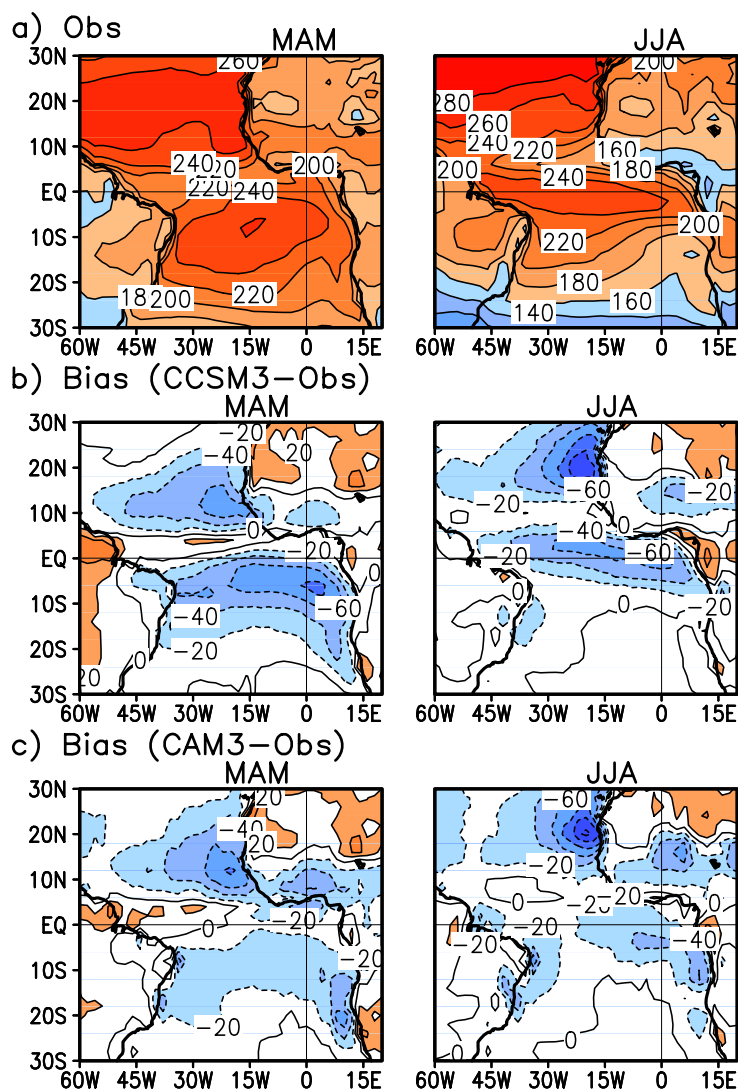


Figure 2.8 Seasonal surface radiative fluxes. a) Observed net short wave radiation; b) CCSM3 net short wave radiation bias; c) CAM3 net short wave radiation bias. Contour intervals: 20 W/m².

e. Oceanic variables: heat contents, Ekman vertical velocity, and ocean current

To evaluate the role of mixed layer entrainment/mixing in CCSM3 we need to examine the ocean stratification. Along the equator, the observed thermocline slopes upward from a depth of 80m at 30°W to 50 m at 0°W during MAM (**Figure 2.3c**) to balance the easterly surface stress. The weakening of the Walker Cell and the reversal of the trade winds causes the CCSM3 thermocline to reverse this slope, descending from 70m depth at 30°W to 100m depth at 0°W. The reversal of the zonal trade winds also reverses the sign of the vertical velocity at the base of the oceanic mixed layer (**Figure 2.9**). In JJA, the spatial pattern of Ekman pumping is similar to observed, but is shifted southward reflecting anomalous southward shift of the ITCZ (**Figure 2.7**).

The heat content of the upper ocean, thus, is anomalously high on the southeast side of the basin and anomalously low on the northeast side (a pattern closely matching the bias in SST except near the equator in MAM) by up to 4°C averaged over the depth range 5-96m (**Figure 2.3a**). Along the equator the observed westward upper ocean pressure gradient (reflecting the slope of sea level) is weakest in March-April. During these months the bias in the zonal gradient of heat content, also reflected in the depth of the thermocline, is sufficient to cause the ocean surface pressure gradient to reverse. The result of the reversal of both the winds and pressure gradient causes the acceleration of an eastward jet with speeds exceeding 40cm/s at the surface and reaching depths of 80m. Below this jet a weak westward Equatorial Undercurrent develops with speeds of 20 cm/s (**Figure 2.10**). This balance of terms contrasts with the observed circulation in which a brief interval of eastward currents along the equator at 23°W may result from a surfacing of the eastward Equatorial Undercurrent (Grotsky et al., 2005). The CCSM3 thermocline is also more stratified than observed and thus the ocean is too cold at lower thermocline

depths. The absence of cooling due to entrainment/mixing is why SST in the Gulf of Guinea is warmer than observed despite the reduced solar radiation.

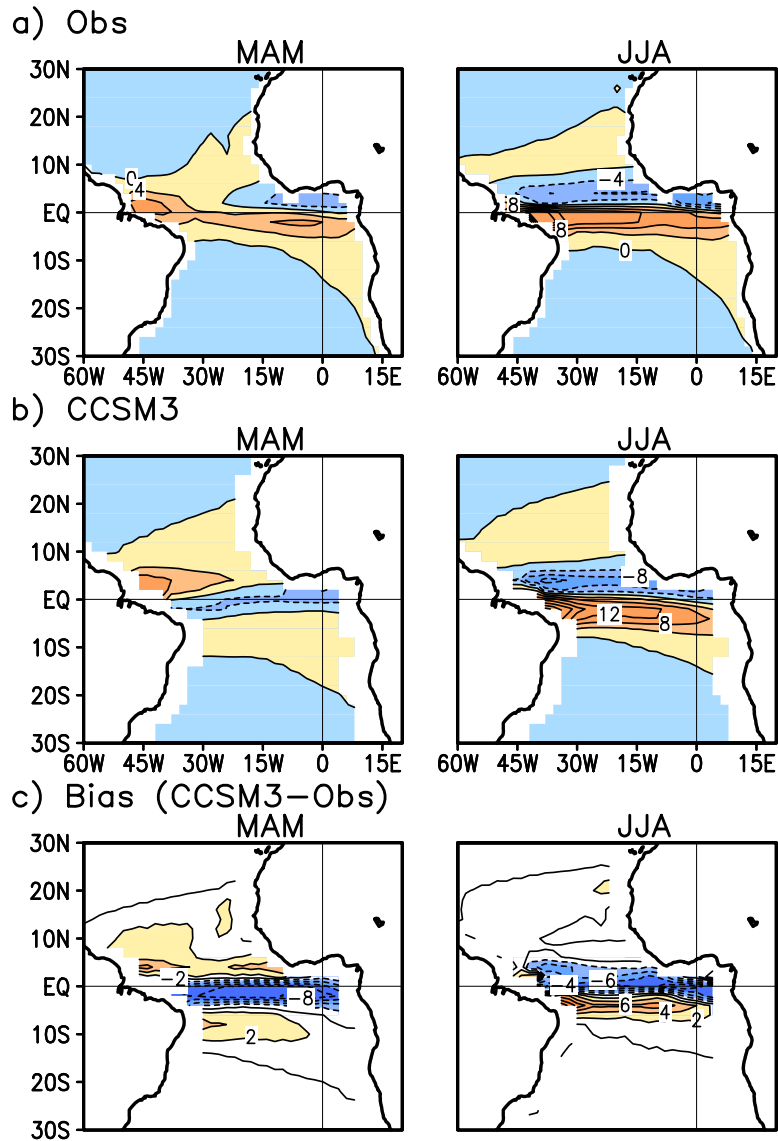


Figure 2.9 Seasonal Ekman vertical velocity. a) Observed; b) CCSM3; c) CCSM3 bias. Contour intervals are $4 \cdot 10^{-6}$ m/s for a) and b), and $2 \cdot 10^{-6}$ m/s for c).

explain the sources of bias in CCSM3. We believe these ideas may also explain why similar patterns of bias develop in other coupled models such as CFS despite wide differences in model physics and numerical codes.

The most striking feature in the bias of SST is the presence of anomalously warm SSTs to the southeast of the climatological position of the ITCZ and anomalously cool SSTs to the north. This SST dipole occurs in conjunction with a southward displacement of the ITCZ by 5-10°, crossing south of the equator in MAM. The anomalous southward shift of the ITCZ is associated with a southward shift of precipitation as well as the appearance of northerly wind errors on the equator which act to enhance the cooling of northern SSTs. In fact each of these features of the bias in CCSM3 is also associated with the observed interhemispheric mode (also known in the literature as the “dipole mode”). The interhemispheric mode, with greatest amplitude in MAM, is observed to vary mostly on decadal timescales. Studies of its dynamics indicate that it is the result of both local air-sea interaction and remote forcing tied to ENSO (Ruiz-Barradas et al., 2003). In CCSM3 it seems that errors in the coupled model project onto the physics of the interhemispheric mode, which then act to reinforce themselves through coupled air-sea interactions (see **Figure 2.1**). The Hadley circulation in CCSM3 is also enhanced, thus giving rise to stronger trade winds in both hemispheres. The latter factor may explain why the CCSM3 wind biases in both hemispheres have the same phase.

Along the equator the CCSM3 winds are characterized by intense westerlies in MAM. These anomalous westerlies occur in conjunction with a modest eastward anomalous gradient of SST and a dramatic deepening of the equatorial thermocline in the eastern basin. These features, as well, are associated with aspects of the normal year-to-

year variability of the tropical Atlantic known as the Atlantic Nino. The warm water accumulated in the eastern basin due to the seasonal equatorial westerly winds then flows southward along the Africa coast, resulting in anomalous warming along the southwest African coast and deepening of the thermocline in this region. The consequent SST bias is reminiscent of the observed phenomenon known as the Benguela Nino. Like the interhemispheric mode, the Atlantic Nino is quite seasonal, occurring in boreal summer when the cold tongue of water normally surfaces along the equator in the east. Here, by comparing the evolution of the anomalous trade winds in CCSM3 and the corresponding atmospheric simulation using observed climatological SST we are able to identify sources for the boreal spring anomalous Atlantic Nino in CCSM3. One source is the development of an anomalous westward gradient in SLP along the equator which is potentially related to the deficiency of the Amazonian precipitation. The resulting westerly wind anomalies are then reinforced by air-sea interactions leading to excess warming of the eastern ocean mixed layer and consequent enhancement of the westward gradient of equatorial SLP. A second potential mechanism involves the influence of the excessively intense subtropical SLP anomalies on the SLP of the western tropical Atlantic.

Biases are also evident in the vertical structure of convection. In addition to the ITCZ being displaced southward, convection is greatly enhanced and extends to greater altitude. The enhancement of convection at low latitude is balanced by more intense descending motion in the subtropics. The excessive precipitation is highly related to the elevated SST in the southeastern basin. Over Northwest Africa anomalously high cloud cover due to the strengthened ascending motion reduces solar radiation by 10-20W/m², while the excessive precipitation extends northward into the southern Sahara broadening

the range of latitudes in which convection is occurring and enhancing evaporative cooling. Thus, surface air temperature remains somewhat lower than observed. This bias occurs in both CCSM3 and in the atmospheric model CAM3 indicating that the cause of at least part of the problem may be attributable to the combined atmosphere/land model rather than a result of interactions with the ocean.

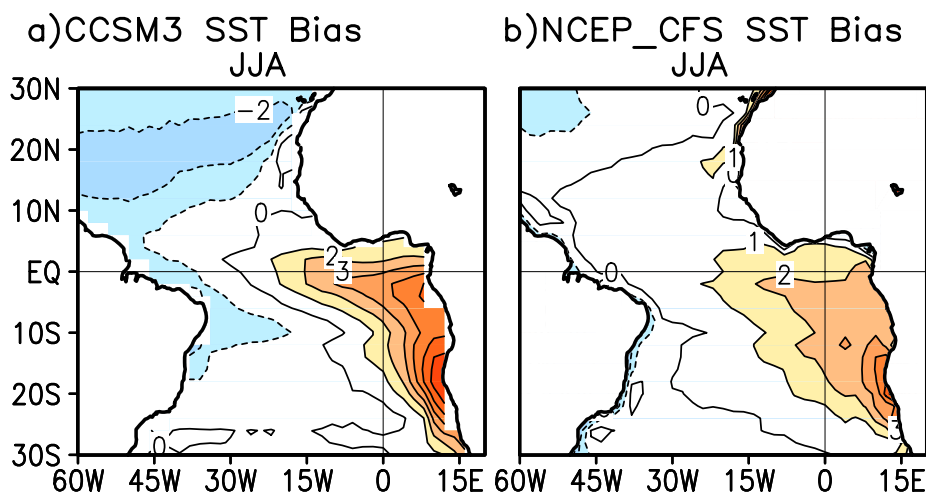


Figure 2.11 SST bias of a) CCSM3 and b) NCEP CFS (see *Saha et al., 2005* for model details). Contour intervals: 1°C.

CAM3 shares with CCSM3 similar patterns (but with less intensity) of biases of SLP, winds, and shortwave radiation. Interestingly, some similar biases have also been found in other atmospheric general circulation models (AGCMs). Okumura and Xie (2004) showed equatorial westerlies over the eastern half of the basin in winter and spring and excessive rainfall in central Africa in the same seasons in the CCSR/NIES AGCM. They argued that the problem of equatorial westerly wind bias may partly explain why many coupled GCMs fail to simulate the Atlantic cold tongue. As shown in our study, equatorial westerlies deepen the thermocline in the southeastern basin, thus preventing the

formation of the cold tongue. The equatorial westerly is also related to the southern displacement of ITCZ during MAM in CAM3. Biasutti et al. (2005) shows that many AGCMs have anomalously abundant precipitation in the Southern Hemisphere during boreal spring, while Biasutti et al. (2005) explore the connection between terrestrial insolation and the marine precipitation. Thus the southward displacement of ITCZ, equatorial westerlies and West African rainfall form a coupled problem. Improved simulation of any of these factors should reduce the biases in the other factors.

3. Origin of the Spring-time Westerly Bias in Equatorial Atlantic Surface Winds in CAM3 Model Simulations²

3.1. Introduction

Trade winds (easterlies) prevail over most of the tropical Atlantic and Pacific Oceans through the course of the year, being strongest in the northern Tropics in summer. Their seasonal fluctuation has a profound influence on sea surface temperature (SST) in the central and eastern basins; and vice-versa. Along the equator, easterly winds generate equatorial upwelling and cold SST, but not simultaneously across all longitudes: Cold SSTs first appear in the far eastern basin, and their leading edge then moves westward generating a tongue of cold SSTs; the cold-tongue is maximally extended in August-September. The easterlies relax in boreal spring, in conjunction with the deepening of the thermocline and appearance of warm SSTs in the eastern basin.

Simulation of the seasonal cycle of the equatorial trade winds is however challenging for both atmospheric and coupled ocean-atmosphere-land general circulation models (AGCM/ CGCM; Davey et al. 2002; Okumura and Xie 2004; DeWitt 2005; Chang et al. 2007). Davey et al. showed the equatorial zonal wind stress to be too weak in many non-flux-corrected CGCMs. Okumura and Xie (2004) found equatorial westerlies to prevail over the eastern half of the basin in winter and spring in an AGCM. DeWitt (2005) showed the weak zonal wind stress along the equator to be the likely cause of the simulated zonal SST-gradient error. The westerly bias in the Atlantic trade winds is thus a common simulation deficiency, but one whose origin remains unclear.

² The work of this chapter has been accepted by the Journal of Climate on January 29, 2008: Chang, C.-Y., S. Nigam and J. A. Carton: Origin of the Spring-time Westerly Bias in Equatorial Atlantic Surface Winds in CAM3 Model Simulations.

The present study seeks to investigate the cause of the westerly wind bias, especially, along the equator, in the CAM3 (NCAR's Community Atmosphere Model, version 3; Collins et al. 2006a) and CCSM3 (Collins et al. 2006b) simulations. The wind bias in these simulations was documented in Chang et al. (2007), who also examined the bias in related atmospheric and oceanic fields. These authors noted with interest the accompaniment of surface westerly bias by upper-level (200 hPa) easterly bias and deficient (excess) rainfall over Amazon (Africa) in the simulations; that is, a weaker Walker circulation in the Atlantic sector. The westerly bias in surface winds was also linked to the anomalously deep CCSM3 thermocline. Based on bias structures, Chang et al. discuss potential causes of the bias, suggesting deficient rainfall over the Amazon as one possibility.

Local mechanisms have also been proposed to account for the westerly trade wind bias in model simulations. These include insufficient generation of stratus clouds (Yu and Mechoso 1999) and coastal upwelling (Large and Danabasoglu 2006), but whether they are the symptoms or the cause remains to be seen. The notion that deficient Amazonian rainfall can be the ultimate cause of Atlantic sector biases in atmospheric and oceanic fields is an interesting, but heretical one, for two decades of ENSO research has emphasized the primacy of ocean-atmosphere coupling in shaping variability in/over the tropical oceans. Land-atmosphere coupling has however been shown to be important in initiating and setting the pace of seasonal variability over the tropical oceans, the eastern basins in particular; through the timing and location (e.g., coastline orientation) of continental convection; for example, Mitchell and Wallace (1992). The Atlantic basin is, if anything, more susceptible to land influences than the eastern tropical Pacific because

of its smaller zonal extent, sandwiched between two major continental convection centers (Amazonia to the west and Africa to the east).

The present study investigates the hypothesis that deficient Amazonian rainfall is the root cause of the westerly bias in equatorial surface winds over the Atlantic. While the hypothesis can be fully tested only with an AGCM, a diagnostic modeling analysis is presented to make the case. The magnitude and extent of the surface wind influence of deficient latent heating over the Amazon is computed using a steady, linearized dynamical core of an AGCM. The diagnostic model is described in section 2 along with the data sets used in this study. The seasonal evolution of westerly wind, precipitation and diabatic heating biases and related evidence that prompted the hypothesis on the controlling influence of Amazonian convection is presented in section 3. Dynamical diagnosis of CAM3's westerly bias in equatorial Atlantic surface winds, including those establishing the viability of the model, is presented in section 4. Synopsis and concluding remarks follow in section 5, where westerly wind and rainfall biases from a recent CAM development simulation³ are presented, in support of the case made in this study.

3.2. Datasets and diagnostic model

a. Simulation data sets

The model simulations analyzed here are the same as in Chang et al. (2007). The mean of a 5-member ensemble of T-85 resolution CAM3 AMIP simulations is analyzed. The CCSM3 simulations come from the “20th Century Climate in Coupled Models” project of the Intergovernmental Panel on Climate Change and are archived at the

³ The simulation was generated with a CAM development model (CAM3_3_fv_cmt2_dilute) that incorporated improvements to the deep convection scheme (Richter-Neale).

Program for Climate Model Diagnosis and Intercomparison (PCMDI) website, as case b30.030a (20C3M run1). This coupled integration, initiated in 1870, is forced by historical ozone, solar, volcanic, greenhouse gases, and sulfur dioxide/trioxide distributions.

b. Precipitation

Monthly precipitation analysis, based on satellite and gauge measurements, comes from the Global Precipitation Climatology Project (GPCP, version 2; Adler et al. 2003). Data is available on a 2.5° x 2.5° grid over both land and ocean, for the 1979-2006 period.

c. ERA-40 atmospheric analysis

The European Centre for Medium-Range Weather Forecasts (ECMWF) 40-year global reanalysis (ERA-40; Uppala et al 2005) spans September 1957-August 2002 and is locally available on a 2.5° global grid and 23 levels in the vertical. The reanalysis combines model forecast fields, satellite data, radiosonde and other in-situ data, including aircraft and ship reports, with 3D-VAR data assimilation. The ERA-40 assimilating model is the modified ECMWF Integrated Forecasting System which is a T-159 spectral resolution model with 60 vertical levels. The 1979-onward reanalysis, benefiting from inclusion of satellite data, is used in assessing model simulations and in generating the basic state and forcing fields for the diagnostic model.

d. Surface winds

Surface wind speed estimates (combined with wind directions from ECMWF analysis) are available on a 1°x1° longitude-latitude grid for the 1988-2000 period from

the Special Sensor Microwave Imager (Atlas et al. 1996), and this record is supplemented by the QuikSCAT scatterometer winds (Graf et al. 1998) for the period mid-1999 to 2006.

e. Diagnosed diabatic heating

Diabatic heating was diagnosed in-house using the ERA-40 isobaric reanalyses at 2.5° resolution (Chan and Nigam 2007). Heating was diagnosed as a residual in the thermodynamic equation (e.g., Hoskins et al. 1989; Nigam 1994), using monthly-averaged data and sub-monthly transient fluxes; just as it was earlier for NCEP and ERA-15 reanalyses in Nigam et al. (2000).

f. Diagnostic model

The steady linear primitive equation (SLPE) model solves the σ -coordinate ($\equiv p/p_s$, where p_s is surface pressure) primitive equations. The equations are linearized about a zonally symmetric basic state, and the model solves for the eddy component (i.e., deviation from the zonal average) of the circulation. The linearized model equations are given in the appendix of Held et al. (1989). In order to realistically represent the thermal and momentum diffusion processes in the planetary boundary layer, the simplified Rayleigh momentum dissipation and Newtonian temperature damping terms in these equations are replaced by linearized versions of the vertical momentum and thermal diffusion terms (Nigam 1997). The diffusion coefficients vary in the boundary layer, decreasing rapidly above 925 hPa. The inclusion of diffusive mixing leads to lower boundary conditions on zonal and meridional velocity, and temperature, requiring specification of drag coefficients, CDU, CDV, and CDT. In addition to vertical diffusive mixing in the planetary boundary layer, the thermodynamic and horizontal momentum

equations include horizontal diffusive mixing, with a constant coefficient of 1×10^6 . Additional model details can be found in the appendix of Nigam (1994) and Nigam and Chung (2000). All model parameters are specified exactly as in Nigam (1997), except for the drag coefficients CDU and CDV, which are both set equal to 1.0×10^{-3} instead of 1.5×10^{-3} .

The diagnostic model is solved numerically, using the semi-spectral representation for horizontal structure: 73 grid points between the two poles ($\Delta\theta = 2.5^\circ$), and zonal Fourier truncation at wavenumber 30 (equivalent to $\Delta\lambda = 6.0^\circ$), where θ is latitude and λ the longitude. The vertical structure is discretized using 18 full-sigma levels of which 14 are in the troposphere, including 5 below 850 hPa. The semi-spectral model was preferred in view of strong latitudinal variation of tropical features, such as the Inter-Tropical Convergence Zone.

3.3. CAM3 biases in the Tropical Atlantic

a. Westerly wind bias

The seasonal evolution of surface zonal wind at the equator is shown in the upper panels of **Figure 3.1** at monthly resolution⁴. Both satellite based wind observations and ERA-40 reanalysis capture the seasonal cycle – annual in the western and semi-annual in the eastern basin – quite well. Model simulations fare well in the latter half of the calendar year, but not in boreal spring when westerlies are present in most basin longitudes, and not just the eastern sector (as in observations). The westerly bias in

⁴ The 20-year simulation climatologies are only marginally different from the 50-year climatologies shown in Chang et al. (2007).

modeled surface winds is extensively documented in Chang et al. (2007), who show the entire deep Tropics (10°S-10°N) to be biased, with the zonal-wind bias peaking at the equator; see their **Figure 3.4**. The westerly bias is evidently amplified in the presence of an interactive ocean, for CCSM3's bias is twice as large, and a bit delayed, as well. The westerly bias effectively changes the character of seasonal variability in the eastern basin, from semi-annual to annual, especially in the CCSM3 simulation.

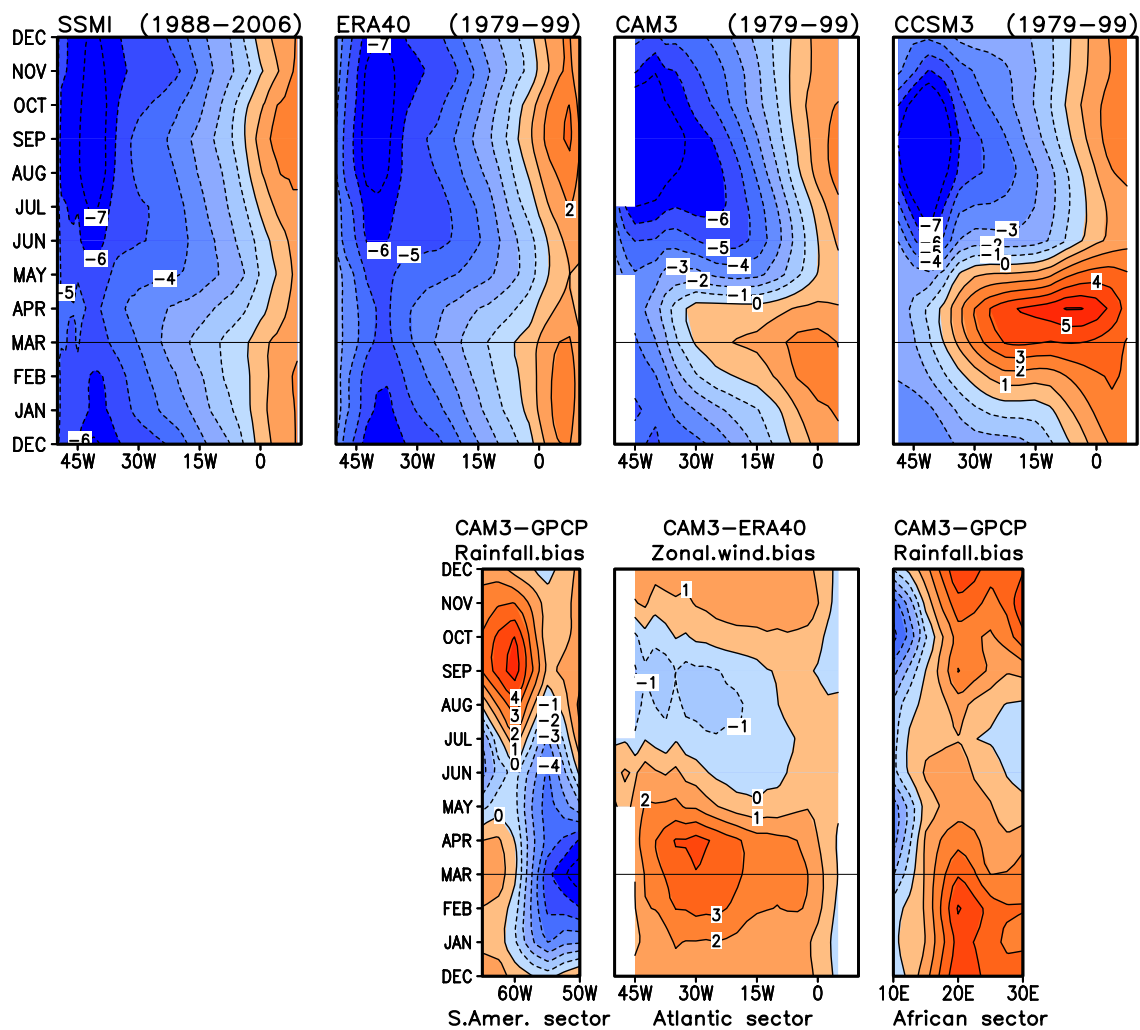


Figure 3.1. Seasonal evolution of the surface zonal wind (upper panels, 1 m/s), zonal wind bias (lower middle, 1 m/s), and rainfall bias in the equatorial American and African sectors (lower left and right panels, respectively, 1 mm/day). Data is averaged over 2°S-2°N in all panels. Wind is from the 1000 hPa level in model simulations. The GPCP rainfall climatology is for the 1979-2005 period.

An intercomparison of observed and modeled zonal wind evolution (upper panels in **Figure 3.1**), especially, the slope of westerly wind contours in the winter-to-spring months, initially suggested an eastern origin of the bias, tempering efforts to connect the bias (and the weaker Walker circulation) with Amazonian rainfall. Plotting the bias itself, however, clarified the situation: The CAM3 bias with respect to ERA-40 (lower middle panel in **Figure 3.1**) clearly shows the westerlies to originate in the western sector, e.g., from tracking of the +2 m/s contour.

b. Precipitation bias

The precipitation bias structure provides further insight into the origin of the westerly bias. CAM3's bias in Amazonian and African precipitation with respect to GPCP rainfall is shown in the lower left and right panels of **Figure 3.1**, respectively; with the panel lineup in accord with regional geography. Immediately apparent is the big deficit in eastern Amazon rainfall (by 6-7 mm/day) and its timing. The maximum deficit is in March, i.e., during the peak of the local rainy season. Interestingly, the deficit develops near-synchronously with the westerly bias, which peaks in March-April; the wind-bias lags Amazon rainfall by, at most, a month. CAM3's bias relative to ERA-40 rainfall (not shown) is very similar. The spatio-temporal structure of the eastern Amazon rainfall deficit and the downstream westerly wind bias thus provide strong, albeit circumstantial, evidence for an Amazonian origin of the Atlantic Walker circulation bias in CAM3/CCSM3 simulations.

Connection of the westerly bias with simulation errors in African rainfall – the other anchor point of the Atlantic Walker circulation – is examined in the lower right panel of **Figure 3.1**. Unlike over the Amazon, CAM3 generates excessive rainfall over much of

Africa. The year-round excess is, typically, 3-4 mm/day except in summer when it is lower. Evolution of the westerly bias in the eastern basin indicates some susceptibility to the African rainfall errors. Diagnostic modeling analysis, discussed later, however shows the Amazon influence to dominate over most of the Atlantic basin.

The off-equatorial distribution of observed and simulated precipitation over the Amazon and surrounding regions (land and ocean) is displayed in **Figure 3.2** (left panels), for the peak westerly-bias period, March-May. The CAM3 bias shows rainfall over tropical South America to be deficient, especially, over the eastern Amazon (-5 mm/day) and Andes (-2 mm/day); in both cases, the deficiency is as large as $\sim 50\%$ of the local climatology, and thus quite significant. The rainfall deficits are reflected in the diabatic heating distribution, shown next.

c. Diabatic heating bias

Diabatic heating, generated from both cloud-scale and large-scale processes, is the principal forcing of the tropical circulation. The latent heating component is dominant in the deep Tropics, especially in regions of deep convection, such as the Inter-Tropical Convergence Zone, the Western Pacific Warm Pool, and the Amazon. A close correspondence between precipitation and vertically averaged diabatic heating is expected in these regions, and this expectation is borne out in **Figure 3.2** (right panels). The correspondence is particularly striking in the middle panels, where both fields are from CAM3. Note the similar location of the field maxima. The correspondence in the top panels is not as striking since the fields are from different sources and because residual diagnosis of heating in regions of steep orography is more uncertain, especially if the underlying circulation and temperature analyses are not well anchored by observations;

the case over most of South America. Even so, the correspondence over eastern Amazon is notable and manifest in the similarity of this region's heating and precipitation biases.

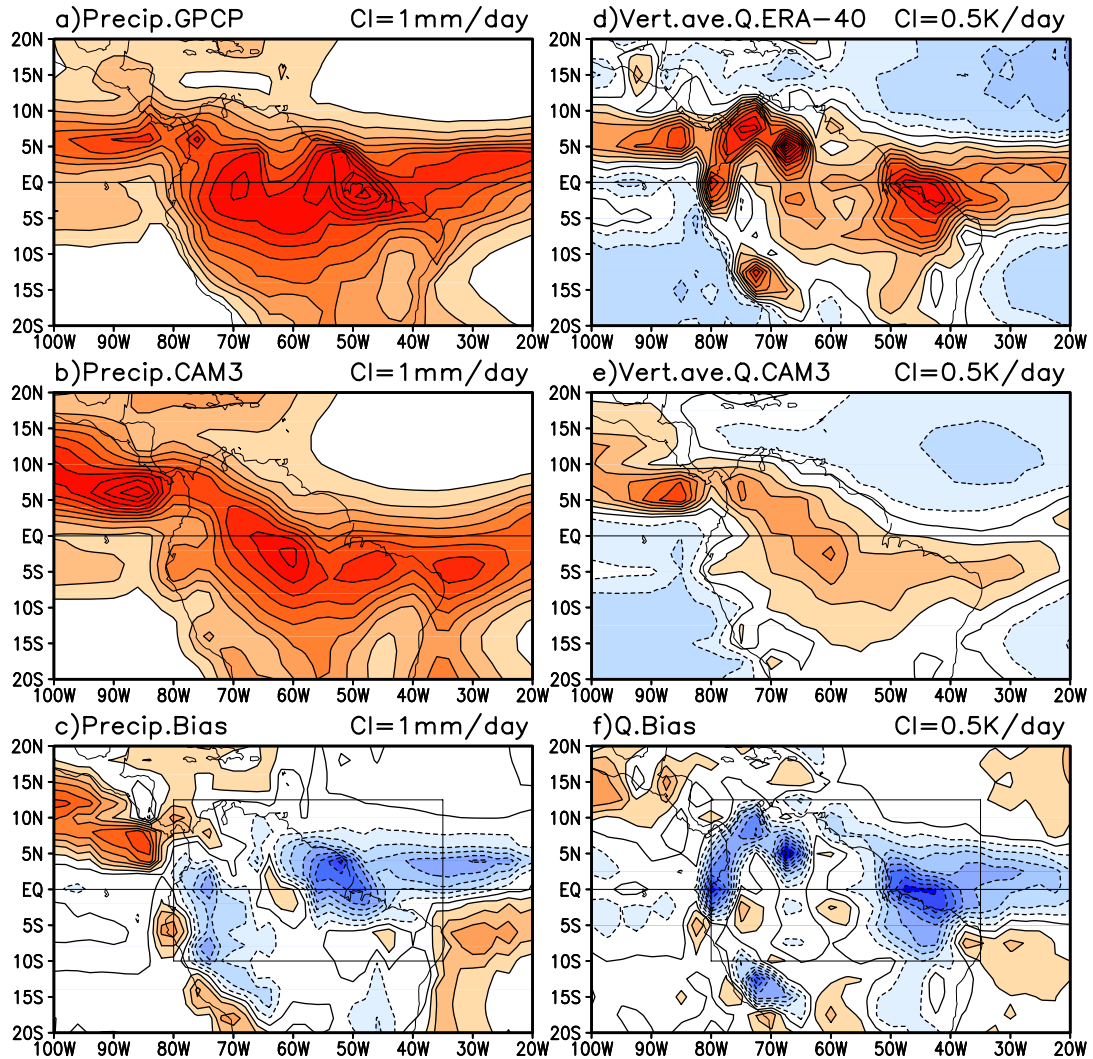


Figure 3.2 Precipitation (left, 1 mm/day) and diabatic heating (right, 0.5 K/day) distribution over tropical South America in observations and CAM3 simulation during March-May. Observationally derived fields are in the top panels, CAM3 ones in the middle, and the CAM3 bias (e.g., CAM3-ERA-40) in the bottom panels. The mass-weighted vertical average (175 hPa to the surface) of heating is displayed. The marked rectangle in the bottom panels indicates the tropical region whose influence is subsequently investigated.

3.4. Dynamical diagnosis of CAM3's westerly bias in surface winds

Modeling analysis that provides insight into the origin of CAM3's westerly bias over the equatorial Atlantic is reported here. The dynamical diagnosis is conducted using a diagnostic model – a choice that needs some justification in view of vigorous ocean-atmosphere-land interaction in the Tropics. As noted before, the westerly bias is present in both CAM3 and CCSM3 simulations, albeit more robustly in the latter, indicating that this bias is not rooted in ocean-atmosphere interactions. The same however cannot be said for land-atmosphere interactions since rainfall generation and distribution is governed by a number of processes including those dependent on the land-surface state. The use of an atmosphere-only diagnostic model, as here, can thus be limiting, especially if the analysis goals extend beyond identification of geographic regions exerting unrealistic local and remote influences. The present analysis seeks only such identification in context of CAM3's Atlantic sector biases, deferring further analysis of the causes of aberrant model behaviour over the South American continent to a later study.

A prerequisite for dynamical diagnosis is the diagnostic model's ability to simulate the target field: the CAM3's Atlantic sector bias, here. If notable features of the bias can be simulated, its origin can be investigated, at least, in a diagnostic (a posteriori) sense. For a meaningful analysis, the model should be required to simulate the individual circulations (observed, CAM3) as well. This assessment is made in **Figure 3.3** which shows the observed and diagnostically simulated March-May surface circulations after removal of the zonal-mean component; i.e., only the eddy components are shown. The zonal-mean component is removed as the diagnostic model is linearized about it; making this circulation component common to the target and simulated fields.

a. Model assessment: March-May simulation

In the **Figure 3.3** simulation, the zonal-mean zonal and meridional velocities, temperature, and surface pressure from ERA-40 are the 2D model inputs (basic state specification); and orography, surface temperature, and diagnosed 3D diabatic heating and submonthly transient heat and momentum fluxes are the model forcing. The surface circulation, consisting of sea-level pressure (SLP) and 1000 hPa winds, is of direct interest in view of the westerly surface wind bias; both target (ERA-40) and simulated surface fields are shown. The SLP-high in the tropical/subtropical Atlantic (and Pacific) is reasonably simulated, except for the amplitude; the mid-latitude simulation is even better. In the Tropics, where SLP is no longer a proxy for the winds, the simulated trade winds are weak in the northern, but not southern, tropical Atlantic. The reasonable simulation of ERA-40's March-May surface circulation clears the way for the next level of model assessment: its potential in simulating the CAM3 bias.

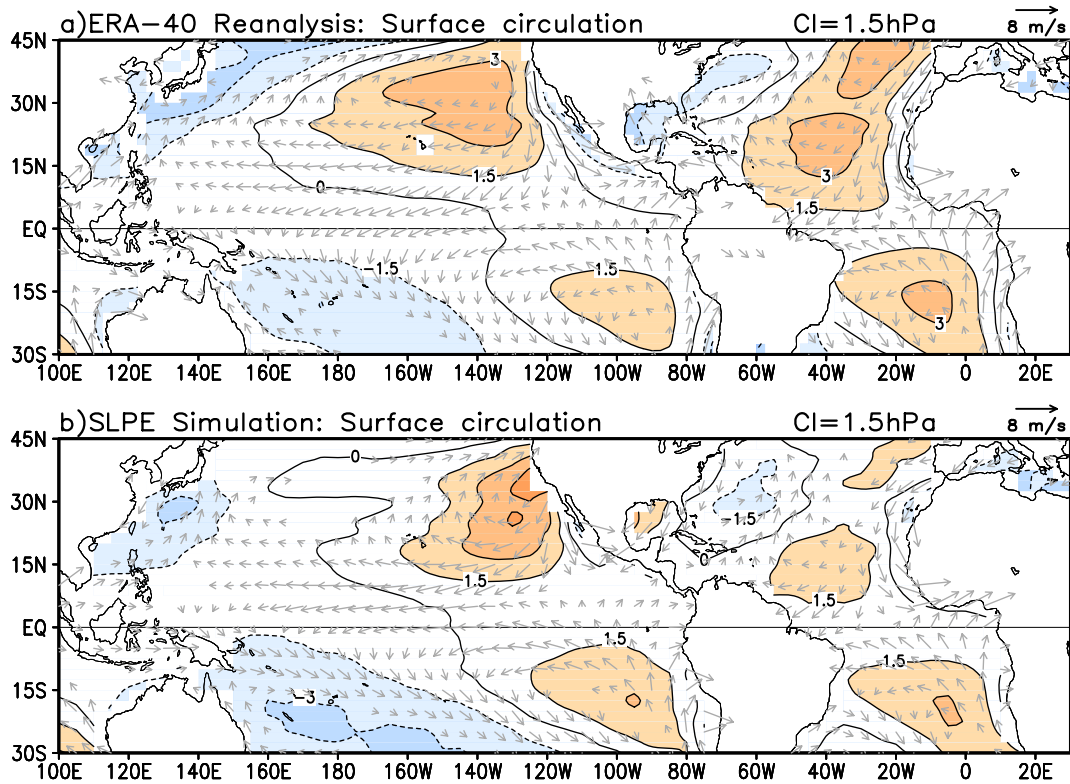


Figure 3.3 Observed and diagnostically simulated March-May surface circulation (zonally asymmetric part) in the Pacific and Atlantic sectors: Sea-level pressure and 1000 hPa winds from ERA-40 reanalysis are shown in the upper panel, while their simulation from the SLPE model is shown in the lower panel, using the same contour interval and vector scale. The SLPE model is forced by orography, 3D diabatic heating, and submonthly thermal and vorticity transient fluxes, all obtained/diagnosed from the ERA-40 reanalysis. Wind vectors are not plotted when the wind speed is less than 1 m/s, and values over land are masked out prior to computation of the zonally-asymmetric component.

b. Model assessment: Bias simulation

The simulated CAM3 bias is shown in **Figure 3.4**, with target fields in the top panel. The simulation is obtained without transient forcing, mechanical or thermal; and as the difference of two diagnostic model solutions: One obtained with ERA-40 zonal-mean basic state, surface temperature, orography, and diagnosed 3D diabatic heating, while the other with the CAM3 counterparts. The thermal and mechanical transient forcing is not applied in each case, in part, because the sub-monthly transient fluxes were unavailable in the CAM3 archive. Note, the zonally-asymmetric component of the SLP and 1000 hPa winds are displayed in both cases.

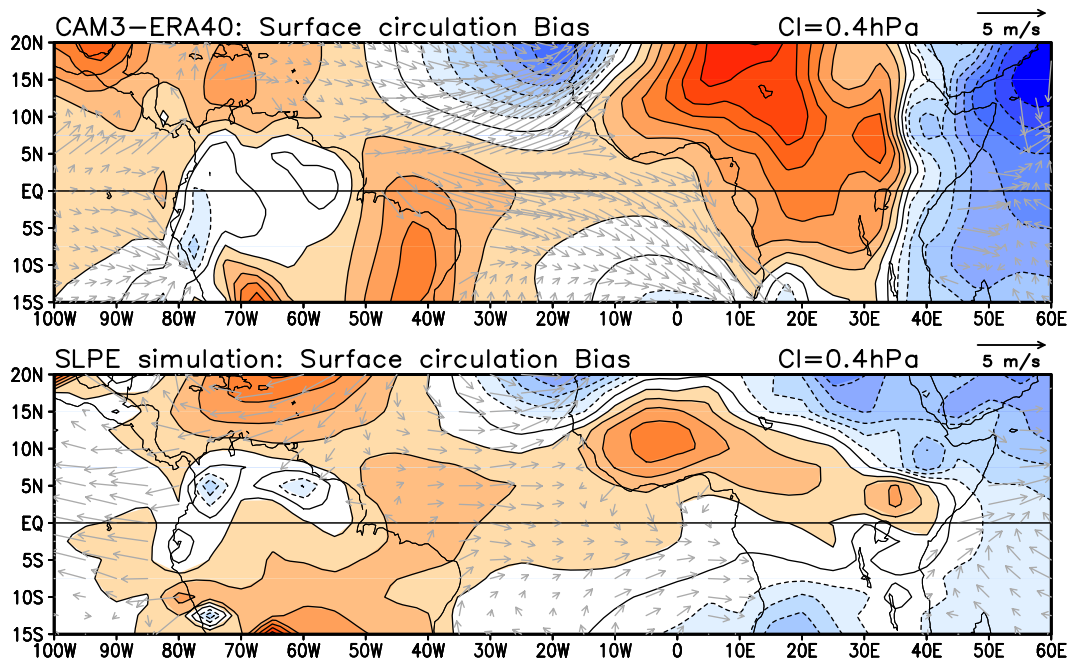


Figure 3.4 CAM3’s surface circulation *bias* (upper panel) and its diagnostic simulation (lower panel): The zonally asymmetric part of sea-level pressure and 1000 hPa winds is shown, as in **Figure 3.3**. The diagnostic simulation is obtained without thermal and mechanical transient forcing bias. The SLP contour interval and wind vector scale are indicated in the title line. Positive SLP bias is shaded red.

The bias simulation is reasonable, but not as remarkable as the simulation of the ERA-40 surface circulation (cf. **Figure 3.3**); in part, because of the missing impact of

transient fluxes, which can be significant, especially outside of the deep Tropics. CAM3's westerly bias in the equatorial Atlantic is, nonetheless, captured, albeit with weaker amplitude; just as in **Figure 3.3**. The westerly bias cannot all be attributed to heating differences in view of other model-input differences (orography, surface temperature and zonal-mean basic state). The latter differences are eliminated in the following section through the use of ERA-40 fields in both cases.

c. Diagnosis of CAM3's equatorial westerly bias

The geographic region whose heating contributes most to the equatorial westerly bias in the Atlantic is identified in this section from diagnostic modeling experiments in which heating-bias in selected regions is used as model forcing; all other fields are from ERA-40. The modeled circulation bias can then be unambiguously attributed to the select region's heating bias.

The surface circulation forced by the global tropical (15°S to 15°N) heating bias is shown in **Figure 3.5a**. Almost all of the SLP bias (~ 1 hPa) and westerly wind bias (~ 3 m/s) in the western equatorial Atlantic originates in the Tropics, not surprisingly. Note the smaller (half) SLP contour interval in **Figure 3.5**. In the interest of space, only the surface simulation is displayed. The influence of regional heating biases in the Tropics is examined next, beginning with the South American sector (80°W-35°W, 10°S-12.5°N; marked rectangle in panel b). Panel comparisons indicate that between half-to-two-thirds of the westerly bias attributed to the Tropics (panel a) originates in the South American region. The sector's influence is far from local, extending up to the African shores. The maximum westerly response, ~ 1.6 m, is located $\sim 30^\circ$ W, i.e., close to the location of CAM3's peak westerly bias. The structure of the surface response, with westerlies to the

east of the eastern Amazon cooling (cf. **Figure 3.3**) and easterlies to its west, indicates weaker surface convergence and ascending motion over the eastern Amazon in CAM3.

The next two panels parse the **Figure 3.5b** response into parts forced by the land and ocean sector heating biases. The surface circulation forced by the continental heating bias is shown in panel c. Its structure is similar to the total response (panel b) but the amplitude is smaller, being one-third to half of the latter: The continental forced westerly bias is ~ 0.6 m/s at 30°W , i.e., significant; especially, since continental convection biases are less labile than oceanic ones, in part, because the land-surface state (e.g., soil moisture) cannot change as readily as SST can from equatorial and coastal upwelling. Efforts to reduce coupled model biases, especially seasonal ones, must target the biases in continental regions. A large body of work on seasonal cycle variability in the eastern tropical Pacific (beginning with Mitchell and Wallace's 1992 study) would also argue for such a strategy.

The CAM3 simulation differs from ERA-40 not only in the horizontal distribution of vertically averaged diabatic heating (and thus precipitation in the Tropics), but also in its vertical structure. The heating profiles for the South American region are shown in **Figure 3.6**, separately for the land and ocean sectors⁵. The CAM3 profile is quite distinct from ERA-40's, particularly, over land where it is weaker (stronger) in the mid (lower) troposphere. The excessive low-level heating in CAM3 results from strong sensible heating, arising from warmer than observed land surface temperature (not shown). The CAM3 difference from ERA-40, also plotted, is, interestingly, a mirror image of the

⁵ The profiles are displayed using the σ ($=p/p_s$) vertical coordinate to preclude intercomparison of fictitious below-ground pressure-level heating data, given significant orography in the region. This vertical coordinate however portrays the regional midtropospheric (~ 500 hPa) heating maximum as a lower tropospheric feature, because of lower surface pressure (p_s) over elevated regions.

heating profile typically associated with stratiform convection (cf. Houze 1997); reflecting, potentially, under-simulation of stratiform rainfall in CAM3.

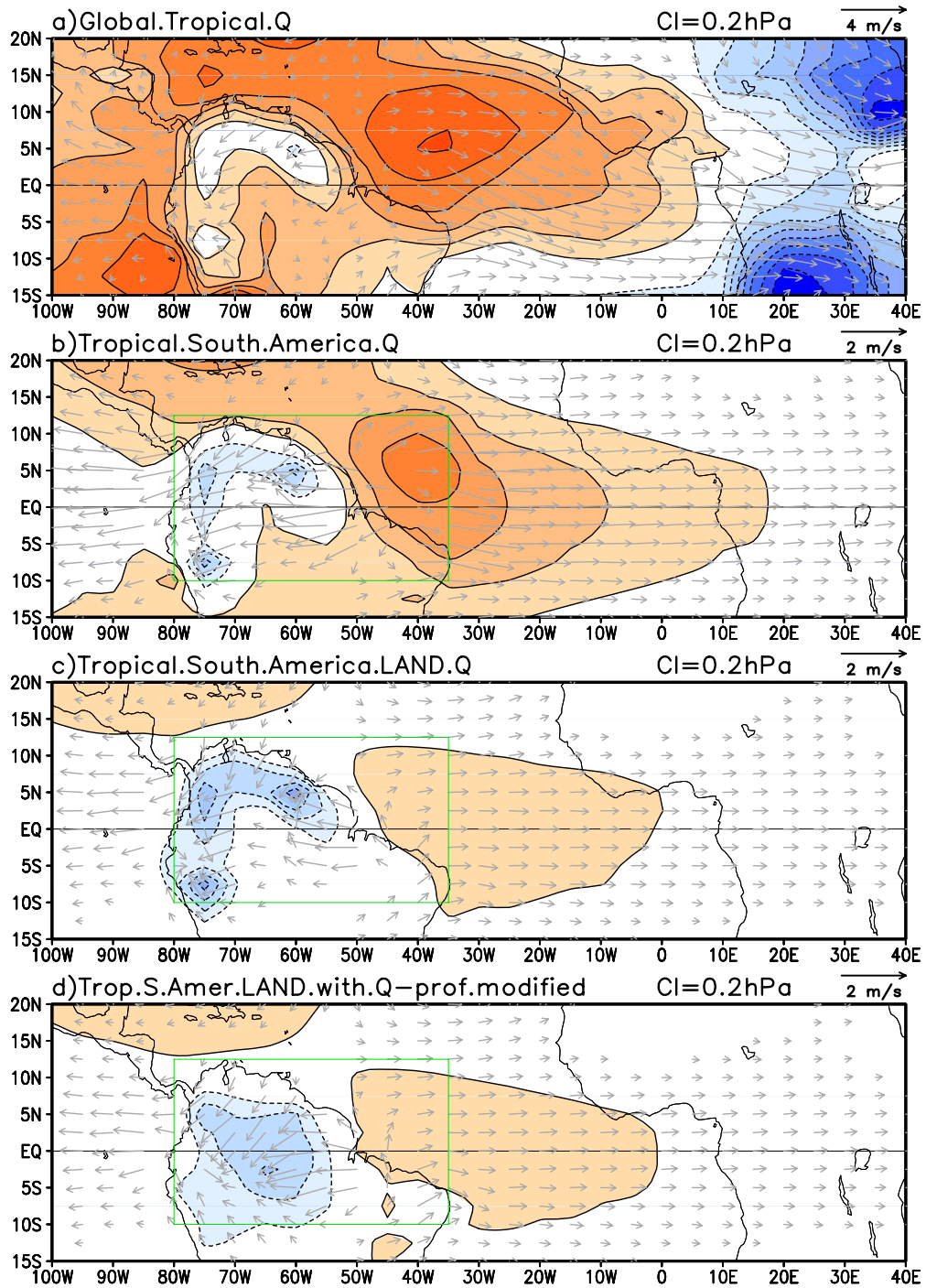


Figure 3.5 Diagnostic analysis of CAM3's March-May surface circulation *bias*: From (a) global tropical (15°S-15°N) heating bias; (b) tropical South American (marked box)

heating bias; (c) tropical South American *continental* heating bias; and (d) synthetic continental heating bias. The latter is obtained by multiplication of vertically averaged heating by the average heating profile over tropical South American land. SLP contour interval (half of **Figure 3.4**) and wind vector scale are indicated in the title line. Vector scale in the top panel is twice as large as in the rest. Bias vectors of less than 0.2 m/s wind speed are not plotted. Positive SLP bias is shaded red.

The heating profile is very influential in the deep Tropics, as latent heating is largely offset by ascent induced adiabatic cooling there, resulting in the pressure vertical velocity (ω) mimicking the heating profile ($N^2\omega \approx Q$, where N^2 is static stability and Q the diabatic heating rate). The heating vertical structure is thus directly tied to the divergent circulation through the continuity equation, and to the rotational flow via the stretching term of the vorticity equation. It is thus of some interest to examine if the heating amount or heating profile differences are more consequential in context of CAM3's westerly bias.

The influence of heating profile differences is assessed by computing the model's response to synthetic heating distributions. These are obtained from multiplication of the vertically averaged heating field by the regionally averaged heating profile, resulting in each grid point of the region having the same heating vertical structure. The synthetic distributions are assessed in **Figure 3.5d**, which shows the model response forced by the heating bias over tropical South America, just as in panel c, except for the use of synthetic CAM3 and ERA-40 heating. The close similarity of surface circulations in panel c and d attests to the viability of this analysis strategy in ascertaining the role of profile differences in generation of CAM3's westerly wind bias over the equatorial Atlantic.

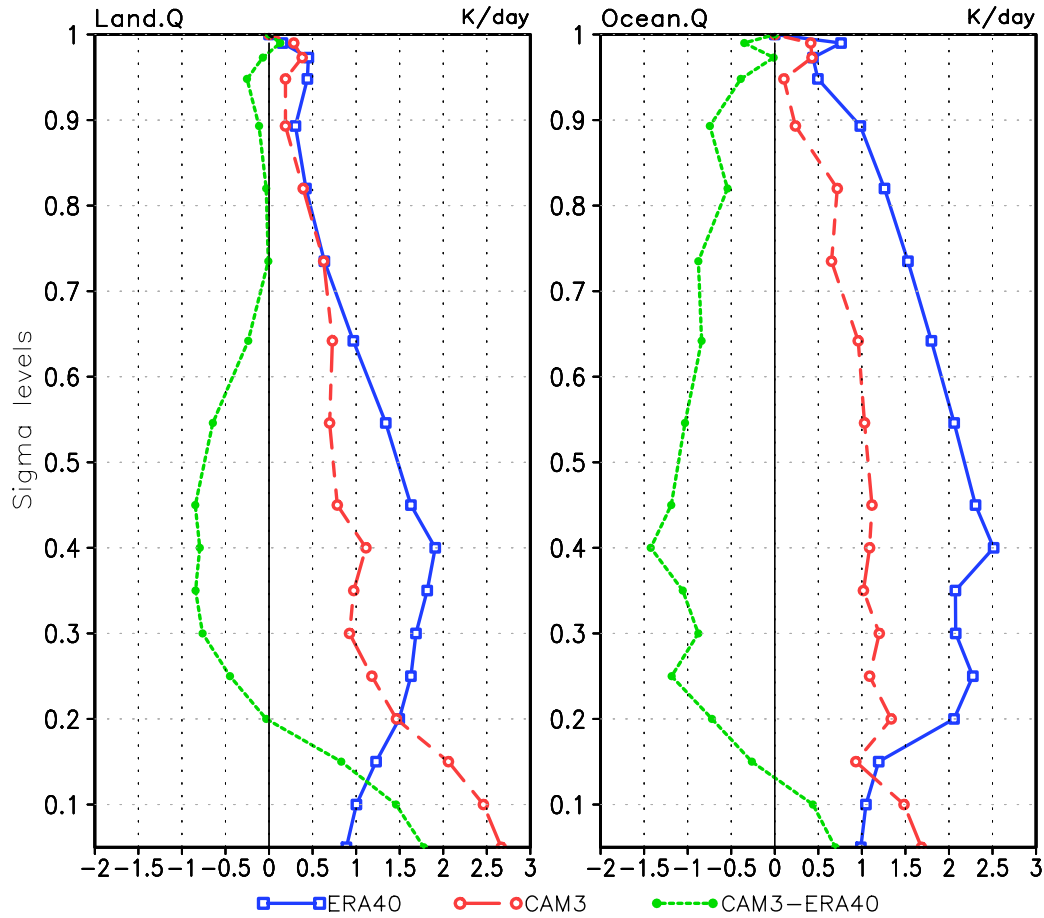


Figure 3.6 Diabatic heating profiles over the tropical South American region: Average profile over the continental (oceanic) region of the box marked in **Figure 3.5** is displayed in the left (right) panels. Both observationally constrained (ERA-40 residual diagnosis, blue) and CAM3 simulated (red) profiles are shown, along with the CAM3 bias (green).

The influence of the South American land heating bias is shown in **Figure 3.7**, with the amount and profile effects separated out. In the top panel, CAM3's heating was modified to have the same profile as ERA-40 heating, while still retaining the amount bias. The resulting surface response shows that the westerly bias attributed to heating bias over tropical South America (cf. **Figure 3.5c, d**) arises largely from heating amount rather than profile differences. The impact of the profile bias on surface circulation (**Figure 3.7b**) was found to be significant as well, but confined to the continental forcing region. The

heating profile bias over tropical South America evidently contributes little to the Atlantic westerly bias.

It is interesting to note the opposite sign of the South American SLP response generated by the amount and profile biases in **Figure 3.7**. The positive SLP in the former case arises from reduced latent heating amount (in mid-troposphere), with concomitant reduction in offsetting ascent, and thus low-level convergence, all consistent with a positive SLP response. The negative SLP response in the profile case arises from excessive low-level heating (and mid-troposphere cooling) in CAM3 (cf. left panel in **Figure 3.6**), whose compensation requires ascent and low-level convergence in the near surface levels; thus, a negative SLP signal.

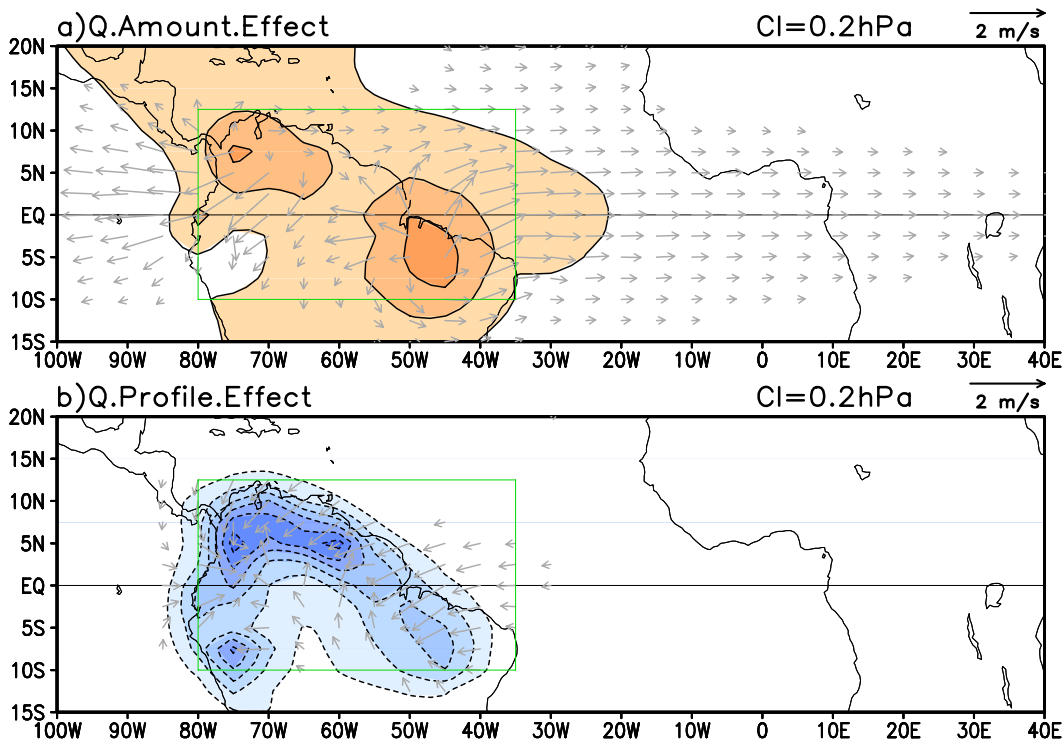


Figure 3.7 Diagnostic analysis of CAM3’s March-May surface circulation *bias* (contd.): Bias forced by synthetic heating over the tropical South American continent (land in the marked box), consisting of only the (a) CAM3 heating *amount* bias, and (b) CAM3 heating *profile* bias. Rest as in **Figure 3.5**.

3.5. Summary and concluding remarks

The study makes the case that westerly bias in CAM3's surface winds over the equatorial Atlantic in boreal spring, and indeed, also in the corresponding coupled model's (CCSM3) surface winds, has its origin in the rainfall (diabatic heating) bias over the tropical South American continent. The case is made from examination of the spatio-temporal evolution of regional precipitation and wind biases, and from dynamical diagnoses of the westerly wind bias from experiments with a steady, linearized dynamical core of an atmospheric general circulation model. Diagnostic modeling indicates that underestimation of rainfall over the eastern Amazon region can lead to westerly bias in equatorial Atlantic surface winds.

A continental origin for a key coupled model bias in the deep Tropics seems somewhat far-fetched at first in view of vigorous ocean-atmosphere interaction in equatorial regions; as, for example, during El Nino Southern Oscillation variability. Implicating deficient modeling of land-atmosphere interaction (leading to diminished continental convection and rainfall) as the source of the downstream westerly bias however seems more reasonable upon further reflection, especially in view of the large body of work on seasonal variability in the eastern tropical Pacific, beginning with Mitchell and Wallace (1992). Their analysis showed continental convection to be the pace maker in seasonal climate evolution in the eastern tropical basins. [Seasonal variability in these regions is pronouncedly annual despite incident insolation being dominantly semi-annual.]

Important support for the South American origin of the Atlantic westerly wind bias comes from a recent CAM development simulation (see footnote 1 for more details). The

simulation was produced at NCAR in early 2007 using a CAM3 version that included improvements to the deep convection scheme. [The improved scheme (Richter-Neale) will be standard in the soon-to-be-released CAM3.5 model.] The westerly bias in the equatorial Atlantic and rainfall bias in the tropical American-Atlantic-African sector are displayed in **Figure 3.8**. Immediately apparent is the significant reduction in the westerly wind bias, by more than 1 m/s (cf. **Figure 3.1**). Also notably diminished is the rainfall bias over the eastern Amazon (and Andean region); but not the ITCZ/rainfall bias over the tropical Atlantic, which is only marginally weaker. The new bias structures support the claim for a defining role of eastern Amazon rainfall deficiencies in generation of the westerly bias in equatorial Atlantic surface winds.

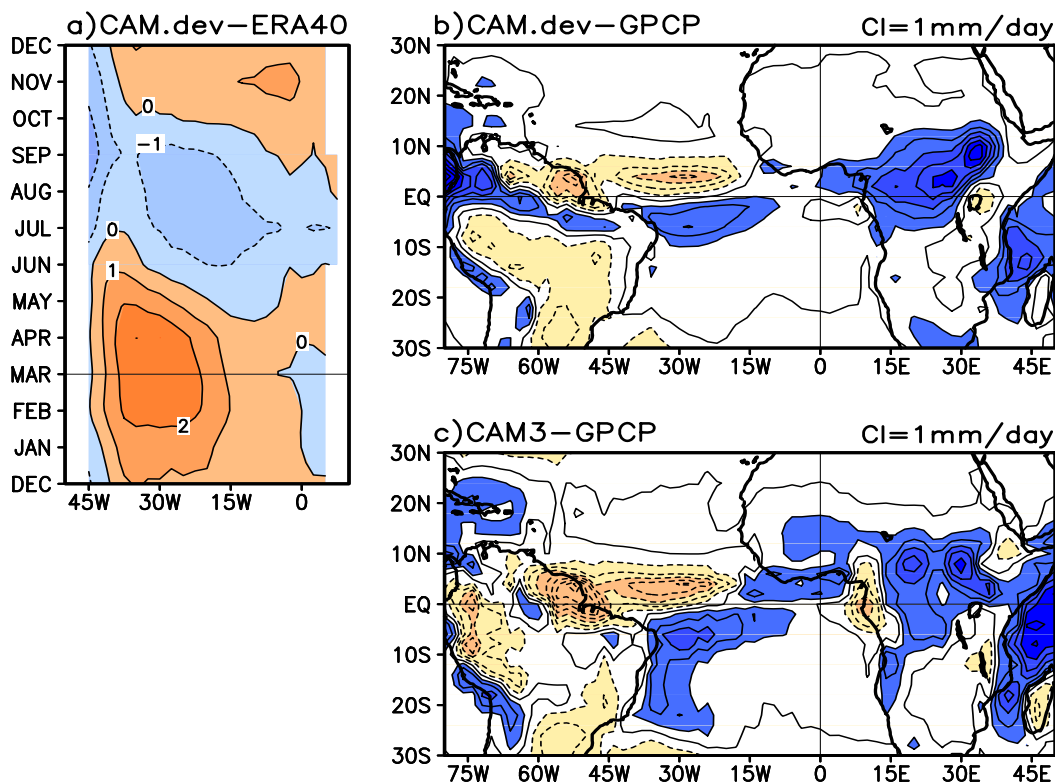


Figure 3.8 Equatorial surface zonal wind (left panel) and tropical precipitation (right) biases in a CAM3 development simulation (Richter-Neale deep convection, see footnote 1 for more details). CAM3’s precipitation bias in an expanded tropical sector is also shown to facilitate comparison. Rest as in **Figure 3.1**.

Our analysis would be incomplete without addressing the role of African rainfall bias in generation of the westerly bias over the equatorial Atlantic. The African bias is broadly of the opposite sign and about half as large as the eastern Amazon bias, especially, in the CAM development simulation; biases of both signs are present along the coast in CAM3. If the African bias was influential, a larger westerly wind bias should be in evidence in the development simulation in view of the coherent and stronger positive rainfall bias in this case. This is however not the case, for the westerly bias is found to be notably diminished in this simulation (**Figure 3.8**). Diagnostic modeling also shows the influence of the African rainfall (diabatic heating) bias to be largely confined to the far eastern basin(cf. **Figure 3.9**); supporting the assessment of a limited role of African rainfall bias in generation of the westerly bias in the western/central equatorial Atlantic basin.

However, this raises another question: Why are diabatic heating deficiencies over Africa not important in generating the Atlantic surface wind bias? The question can be answered at various levels: CAM3's diabatic heating is both positively and negatively biased with respect to ERA-40 heating in the African sector, in contrast with the mostly positive precipitation bias of CAM3 relative to GPCP rainfall! The heating and precipitation biases are more consistent with each other when both are evaluated with respect to ERA-40 data, and the African bias is not as pronounced as the Amazon one in such evaluation. As the linear model is driven by the heating bias, the African component has significantly lesser impact on Atlantic surface winds than the Amazonian one, consistent with the relative strengths of the two bias components. Area-averaged heating

profile in the Amazon and African sectors is shown in **Figure 3.10**, with the bias in the former one being notably strong; answering the question.

Finally, it is of some interest to inquire about the fate of the westerly bias in a coupled ocean-atmosphere environment. The bias is larger in CCSM3 (cf. **Figure 3.1**), as noted before, indicating the lack of any corrective/negative feedbacks in this coupled model. Chang et al. (2007) argue that westerly bias leads to deeper thermocline (and warmer SSTs) in the eastern equatorial basin, with the SST-gradient change generating additional westerlies (cf. Lindzen and Nigam 1987); that is, for the existence of a positive feedback, which amplifies the bias.

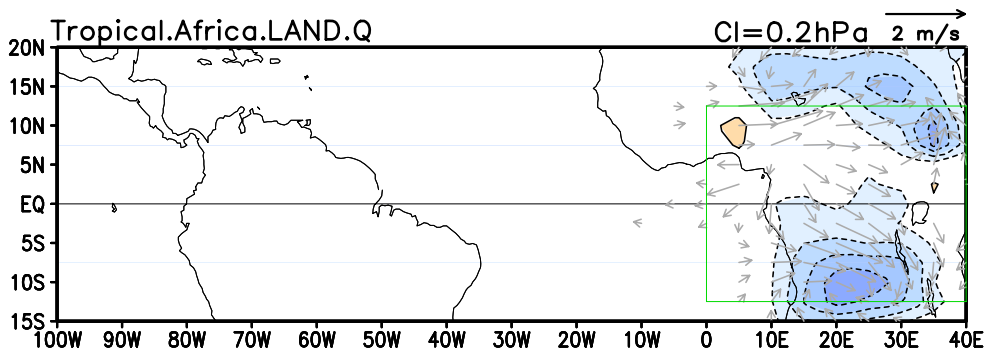


Figure 3.9 Diagnostic analysis of CAM3's March-May surface circulation *bias* from tropical African continental heating bias. Rest as in **Figure 3.5**.

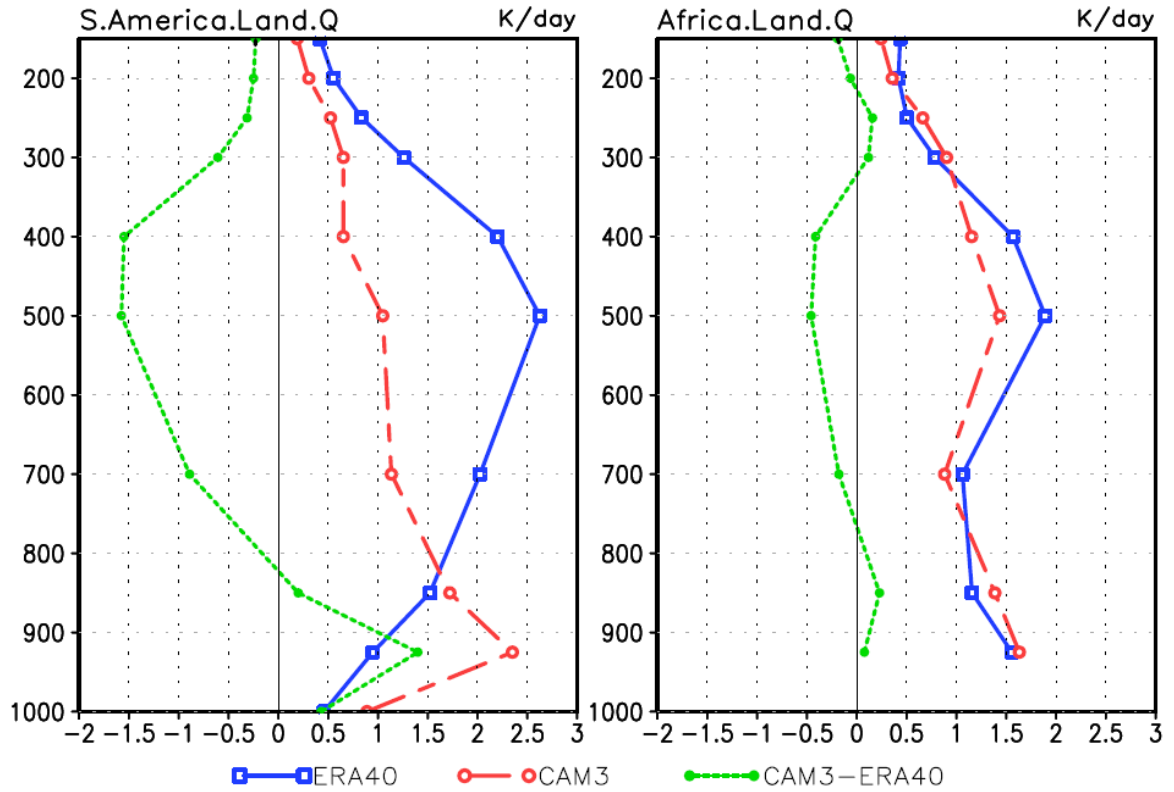


Figure 3.10 Diabatic heating profiles over the tropical South America and *tropical Africa*: Average profile over the continental region of the box marked in **Figure 3.5** (**Figure 3.9**) is displayed in the left (right) panels. Both observationally constrained (ERA-40 residual diagnosis, blue) and CAM3 simulated (red) profiles are shown, along with the CAM3 bias (green).

4. Tropical Atlantic Variability and Prediction of Summer West African Rainfall

4.1. Introduction

At subseasonal periods tropical Atlantic climate is dominated by two patterns of variability, one a meridional pattern of anomalous SST with its strongest expression in boreal spring and another associated with a zonal pattern of anomalous SST located near the equator whose strongest expression is in boreal summer. The meridional pattern is strongly associated with latitudinal location of the Intertropical Convergence Zone (ITCZ) band of enhanced convection. A few studies that have examined the relationship between these two patterns of variability have come to different conclusions regarding which leads which: Servain et al. (1999; 2000) show that the zonal pattern leads the meridional pattern, while Murtugudde et al (2001) found these two patterns have high correlation at zero lag. Here we revisit the observational record to reexamine the relationship between these patterns in order to clarify their relationship and relation to the seasonal cycle. One practical outcome of this clarification of the patterns is that it provides information that can be used to improve seasonal prediction of West African summer rainfall.

The climate of the tropical Atlantic is dominated by the seasonal shift of the ITCZ and consequent shifts of the northeast and southeast trade wind systems. During boreal spring when the ITCZ is in its most southerly position and SSTs are rather uniform with latitude, small anomalies of the meridional SST gradient may induce anomalous shifts in the position of the ITCZ and thus anomalous cross-equatorial winds (Ruiz-Barradas et al., 2000; Chiang et al., 2002). Anomalous shifts in the position of the ITCZ by a few

hundred kilometers can have a vast impact on the climate of the semi-arid Nordeste region of Brazil (Moura and Shukla, 1981). At least two forcing mechanisms have been proposed to explain the prevalence of this pattern of variability. The first is usually referred to as the Wind-Evaporation-SST (WES) feedback which states that SST responds to the changing wind field through its impact on latent heat loss and ITCZ, giving rise to anomalies that act to reinforce the initial wind anomaly (Carton et al., 1996). The sign of this local air-sea interaction may be controlled by ocean advection (Chang et al., 1997). The second is the remote response to the ENSO cycle in the tropical Pacific which impacts SST and winds in the northern tropics (the warm phase of ENSO leads to positive North Atlantic SST anomalies with a few month delay, e.g. Enfield and Mayer, 1997).

During boreal summer when the ITCZ is displaced well north into the northern hemisphere, southeasterly winds prevail along the equator, and a tongue of cool SSTs appears in the east. During some years this cool tongue appears only weakly and is accompanied by weaker than normal zonal winds and a southward shift of convection (Carton and Huang 1994; Henin, 1980). This pattern is usually referred to as the Atlantic Nino due to its similar mechanism to the Pacific ENSO (Zebiak 1993), and is highly related to the zonal wind anomaly in the western equatorial Atlantic (Servain et al. 1982; Keenlyside and Latif, 2007). Like the meridional mode, Atlantic mode is influenced by both the local air-sea interactions and the remote forcing from Pacific ENSO (Wang, 2002; Grotzner et al., 2000). Rainfall over the Coast of Guinea tends to increase during the years of Atlantic Nino (warm events) (Janicot, 1992; Cook and Vizy, 2006).

As indicated above these two patterns (or modes) of interannual variability are linked by the similarity of their impact on the position of the ITCZ and their effect on the

trade winds along the equator. Servain et al. (1999; 2000) carried out an examination of data from the 1980s and 1990s and model simulations for a similar time period and found that these two modes are highly correlated at both interannual and decadal timescales. According to these studies the highest correlation occurs when the zonal mode leads the meridional mode by a month or two, a surprising conclusion since the latter peaks a season before the former. Their results also show that ITCZ leads the zonal mode by two months (and therefore ITCZ also leads the meridional mode).

On the other hand, when data of longer record period (1949-2000) are used Murtugudde et al. (2001) show that the high correlation between these two modes drops off, which they attribute to the mid-1970s climate change, but for shorter record the two modes are highly correlated at zero lag. They also find that the movement of the ITCZ leads the zonal mode. Most recently, Lee and Wang (2008) revisit the relationship of these modes using model simulations and show that at decadal timescales either phase of the meridional pattern leads to the warm phase of the zonal mode because of the cold (warm) water advection in the western (eastern) boundary resulted from an oceanic gyre formed across the equator. The results of Lee and Wang (2008) may explain the drop of the correlation for longer record in Murtugudde et al. (2001), however if this mechanism is dominating, there should be very little correlation between the two modes.

Intrigued by the discrepancies among these studies and the seasonality of the two modes, which would imply the meridional mode leads the zonal mode if there is indeed strong correlation, an aspect absent in those studies, we revisited this problem emphasizing the two modes in their peak seasons. In this paper, we apply Empirical Orthogonal Function (EOF) analysis on seasonal-averaged SSTA of boreal spring and

summer seasons and look for the EOFs that represent the two modes to investigate the relationship between them. The data and the detail of our analysis methods are described in Section 2. The results of EOF analysis are displayed in Section 3 along with regression and correlation analyses between the Principal Components (PCs) and surface variables. Section 4 focuses on the discussion on the mechanism that provides the connection between the modes. In Section 5 we emphasize that the relationship between these two modes can be utilized in the predictability of summer West African rainfall, which is followed by concluding remarks of Section 6. In this paper, we use the terminology meridional mode and dipole mode interchangeably, and similarly for the equatorial mode and zonal mode, as they are usually referred to in the literature.

4.2. Datasets and analysis methods

a. Datasets

The primary dataset of this study, the SST data which we apply the EOF analysis, is HadISST 1.1 SST from the Hadley Center of the United Kingdom Meteorological Office. The original dataset is available on a global $1^\circ \times 1^\circ$ grid for the 1870-onward period. The HadISST 1.1 SSTs are constructed using a reduced-space optimal interpolation along with the insertion of quality-controlled gridded observations onto the reconstruction (Rayner et al. 2003).

The NCEP/NCAR reanalysis (Kalnay et al. 1996) provides the meridional and longitudinal components of the surface winds (at 1000-hPa) for the regression analysis. For the precipitation data, we mainly rely on the CRU TS 2.1 dataset, which consist of century-long observed climate variables, for the period 1901-2002, and covering the global land surface at $0.5^\circ \times 0.5^\circ$ resolution (Mitchell 2004). CRU TS 2.1 dataset provides

only the continental precipitation; for the marine precipitation needed in this study we utilize that from the NCEP/NCAR reanalysis.

The NAO index used in this study is the station monthly NAO index based on the difference of normalized sea level pressures (SLP) between Ponta Delgada, Azores and Stykkisholmur/Reykjavik, Iceland since 1865 (Hurrell et al. 2003).

In this study, to have a coherent climatology when utilizing the surface winds from NCEP/NCAR reanalysis (Kalnay et al. 1996), we take only the 1949-onward data for the HadISST 1.1 SST, the CRU TS 2.1 precipitation, and the NAO index, which also further guarantees the quality of the datasets.

b. Methods

To focus on the modes in their peak seasons of variability, monthly SSTAs derived from removing the climatological values are seasonally averaged for boreal spring (March-April-May) and boreal summer (June-July-August). Then EOF analysis is applied separately on the seasonal-averaged SSTA of spring and of summer. That is, we apply on EOF on spring SSTA and look for the EOF pattern that can best represent the meridional mode. Then we repeat EOF analysis on averaged summer SSTA, but look for the pattern that best represents the equatorial mode. (Although we expect that meridional mode and the equatorial mode should be the prime mode in spring and summer seasons, respectively). Two corresponding PCs derived from the EOF analysis are then defined as the spring meridional mode PC (or dipole PC) and summer equatorial mode PC (or zonal PC). The PCs are used in the regression and correlation analysis to study the relationship between the modes and the surface winds, precipitation, and SSTs.

EOFs derived from the EOF analysis are intrinsically orthogonal to one another, temporally and spatially. This constraint prohibits the investigation on the correlation between any two modes derived from the same EOF analysis on the same variable(s). Therefore Servain et al. (1999) defined different indices for the modes, or different variables need to be chosen for different modes when applying EOF analysis (as in Servain et al. 2000 and Murtugudde et al. 2001, SSTA for meridional mode and changes in equatorial thermocline slope for equatorial mode).

When applying EOF analysis on SSTA of different seasons (as in this study), the derived EOFs in the same season are independent to one another, but modes from different seasons are not necessarily independent to each other, hence investigation on the correlation between modes from different seasons using the same variable (SSTA) is applicable if the connection does exist.

Since the Pacific ENSO can affect both Atlantic SST and equatorial winds (Czaja et al. 2002; Barreiro et al. 2005), one may wonder how ENSO's influence is exhibited in the relationship between the meridional and equatorial modes. To investigate this aspect, we first remove the ENSO influence by subtracting the regression between winter-time Nino 3 index (December, January, and February average) and the monthly SSTA from the original monthly SSTA. After that, we repeat the above described EOF analysis on the ENSO-influence-removed SSTAs.

4.3. Results

a. EOF patterns and PCs – From original SST anomaly

The first EOF in boreal spring is the meridional mode (**Figure 4.1a**), as it should be since this mode is strongest in this season. It has a dipole pattern with opposite signs across

the equator, and a strong meridional SST gradient. This mode explains 37.5% of the SSTA variance in spring. In boreal summer, the first EOF is the equatorial mode (**Figure 4.1b**), as the EOF pattern has maximum amplitude in the eastern equatorial region and is generally of the same sign across the whole basin. This mode explains 41% of the SSTA variance in summer.

The PCs of the spring meridional and summer equatorial modes bear great similarity (**Figure 4.1c**). The correlation coefficient between these two time series is 0.71, significantly high correlation. They both contain decadal and interannual signals, which are consistent with Servain et al. and Murtugudde et al., but the result showed here represents that meridional mode leads the equatorial mode. Although the time lag between these two modes is three months, the high correlation does not necessarily mean that there is a three-month lag between these two modes, but rather just showing a general lead-lag relationship between the modes (the meridional mode leading the equatorial mode). We also de-trend these two PCs (not shown) and re-calculate the correlation, whose value is 0.65, only slightly reduced. This indicates that the long term trend does not significantly contribute to the high correlation, but rather some other mechanism(s) is in effect.

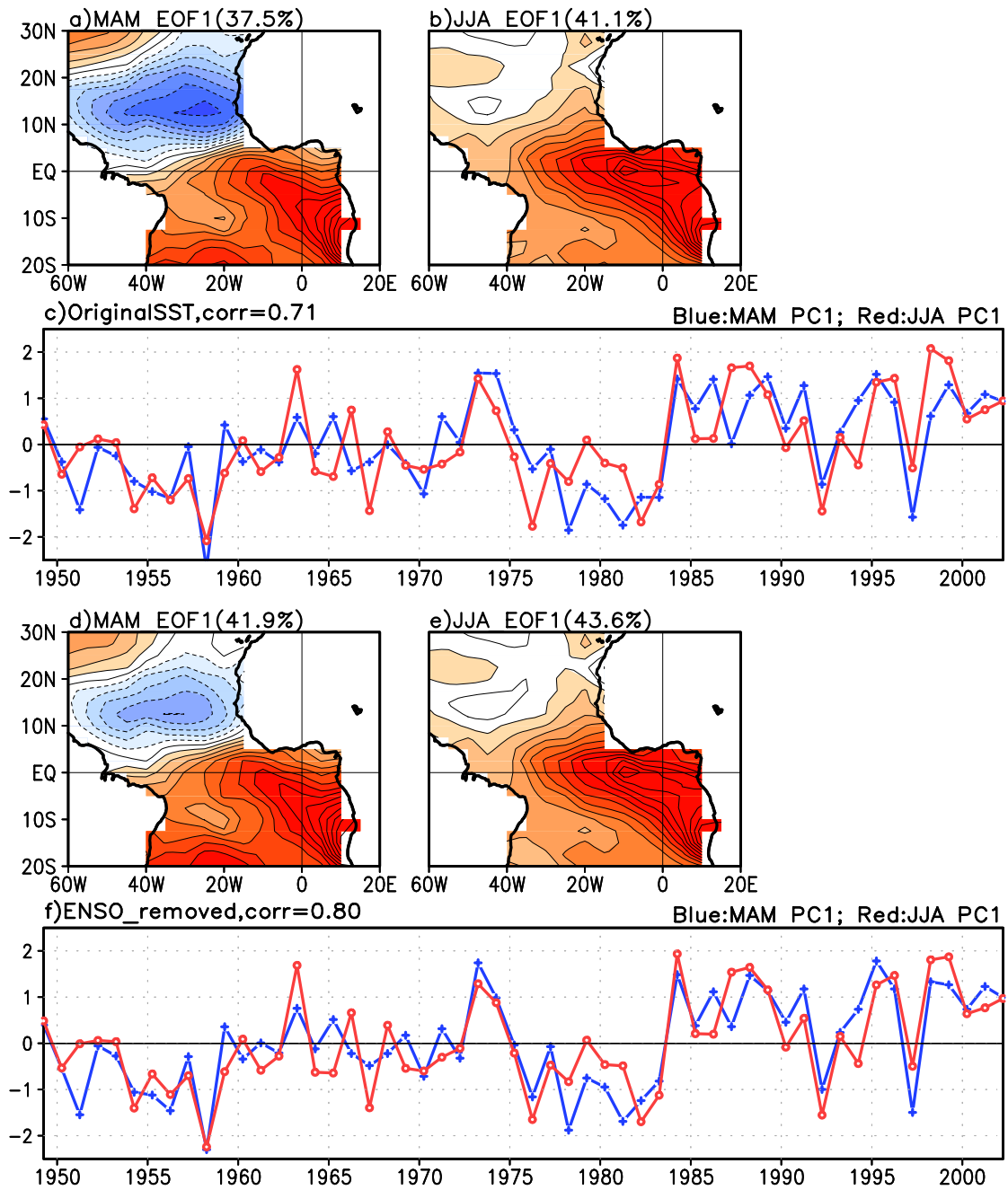


Figure 4.1 EOF patterns and the corresponding PCs. From original SSTA: EOF patterns of spring meridional mode (a) and summer equatorial mode (b), and their PCs (c). From ENSO-influence-removed SSTA: EOF patterns of spring meridional mode (d) and summer equatorial mode (e), and their PCs (f). Contour intervals for a, b, d, and e: 0.05°C .

b. EOF patterns and PCs – ENSO influence removed

The results from the ENSO-influence-removed SSTA are basically the same as the previous case of original SSTA. The meridional mode is still the first mode in spring, but the pattern of the EOF has weaker amplitude in the north hemisphere (**Figure 4.1d**). This is consistent with the findings of other studies that ENSO mainly affects the North Tropical Atlantic SST (e.g. Czaja et al. 2002). The variance explained by this mode increases to 41.9%, but this only means a raise in the relative importance of this mode in this season as the total SSTA variance decreases after removing the ENSO influence. The first mode in summer is still the zonal mode with less change in the EOF pattern (**Figure 4.1e**). The relative variance of this mode in summer also slightly increases.

Like it does to the EOF patterns, removing ENSO influence changes the spring dipole PC more than it does the summer zonal PC (**Figure 4.1f**). This result makes sense as the ENSO influence on Atlantic is known to be of maximum at 4-5 month lag (Enfield and Mayer 1997), which coincides mostly with the spring dipole mode. The correlation between the PCs of these two modes is now 0.8, higher than the previous case of original SSTA, indicating that ENSO in fact adds variability to the dipole-zonal modal relationship and that this relationship is quite internal to Atlantic, not orchestrated by ENSO.

c. Regression and correlation with Precipitation

In this paper hereinafter we will focus on the relation of the two modes, respectively, to precipitation, surface winds, and SST, using PCs derived from the original SSTA to represent the two modes. Contours indicate the magnitudes of the regression between PCs and the surface variables, and shadings represent significant correlation above 95% level.

Although these PCs contain ENSO signal, but as ENSO plays a minor role here, the difference between the two cases (original and ENSO-removed) is rather insignificant.

The meridional mode is known to be related to the spring rainfall over the Nordeste Brazil (Moura and Shukla 1981), as represented by the high correlation/regression between the spring dipole PC and March-April rainfall over this area (**Figure 4.2a**). The equatorial PC has high correlation/regression with the July-August rainfall over the Coast of Guinea (**Figure 4.2b**), which is also consistent with findings in the literature (Hirst and Hasternrath 1983). Therefore although the methods applied here are not identical to those in the literature, the meridional and equatorial modes defined here are consistent with previous studies.

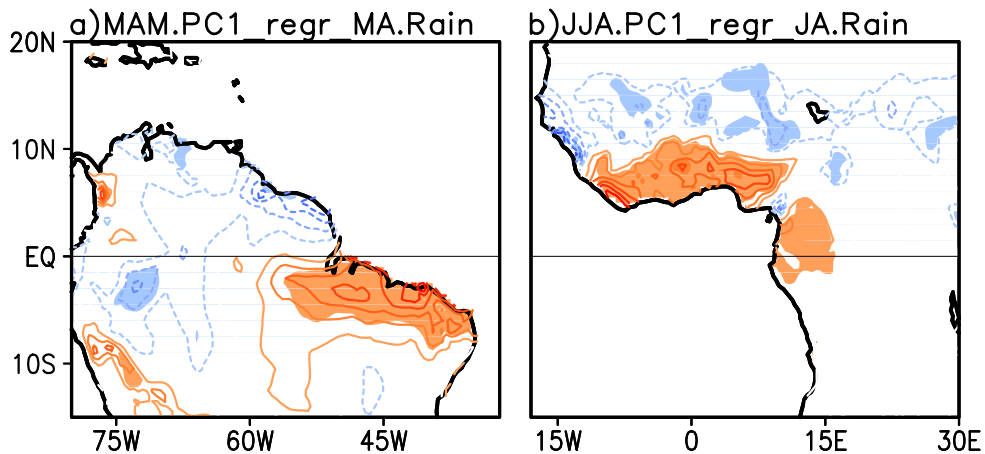


Figure 4.2 Regression (contours) between MAM PC1 and March-April South American rainfall (a); and between JJA PC1 and July-August West African rainfall (b). Shading indicates significant correlation (above 95% level). Contour levels: 3 mm/day.

Figure 4.3 is the real March-to-August monthly SSTA patterns of two example years. Take year 1958 for example, one can see it clearly that in spring there is a dipole pattern of anomaly, warm in the north and cold in the south and along the equator; later on the cold anomaly strengthens along the equator. In the other example of year 1974 which has

the opposite phase of the anomaly, there is also a dipole pattern of anomaly in spring and gradually the anomaly along the equator reinforces. These examples show that the high correlation between the PCs of these two modes is not mere statistical artifact but captures this kind of dipole-to-zonal evolutionary modal relationship between these two modes.

d. Regression and correlation with surface winds

To understand how this dipole-to-zonal model relationship exists we investigate the relationship between the atmospheric surface circulation and each mode. These two modes are known to be associated with the different components of surface winds – dipole mode associated with the cross-equator flow (meridional winds) and zonal mode associated with the zonal wind anomaly in the western equatorial region. Regression and correlation between each component of monthly surface winds and each PC are calculated to show the mode-wind relationship in an evolutionary perspective.

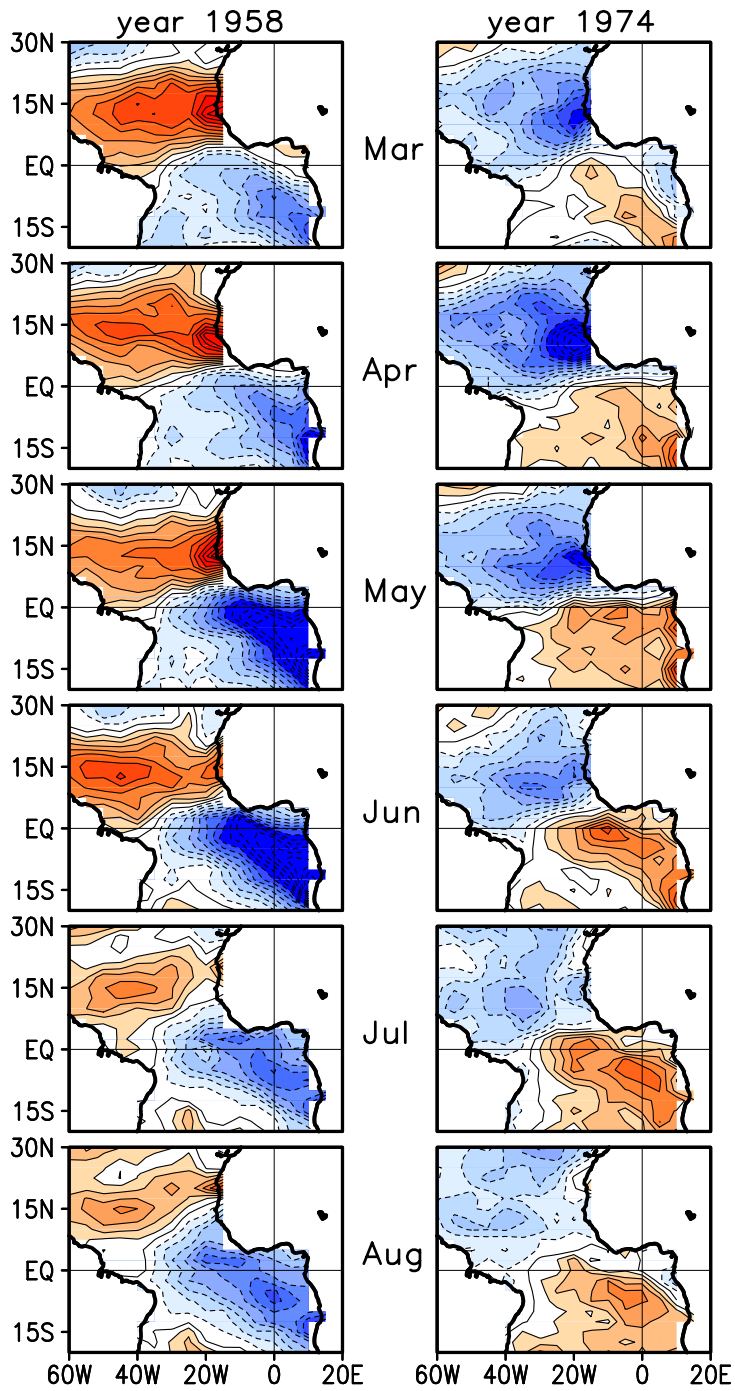


Figure 4.3 Real monthly SST anomaly patterns, March through August, in year 1958 (left panel) and 1974 (right panel).

The patterns of regression of the spring meridional PC and the spring meridional winds show a strong southward cross-equatorial flow corresponding to a cold-

north/warm-south SSTA (**Figure 4.4a, b**). This agrees with the results from the literature for the meridional mode (Ruiz-Barradas et al. 2000), which is another indication that the meridional mode defined here is indeed correspondent with the meridional mode in the literature. This cross-equatorial flow gradually changes into a confluent flow into the eastern equatorial region in the summer, as the northerlies recede and the southerlies in the southeastern basin strengthen (**Figure 4.4c, d**). This result of confluent flow is the same for the regression between the summer zonal mode and the summer meridional winds (**Figure 4.4g, h**). A confluence of meridional winds into the eastern equatorial region is consistent with a warm equatorial SSTA anomaly resulting in an anomalous low pressure of this region, which indicates the emerging of the summer equatorial mode. Interestingly the summer equatorial mode is also highly related to a cross-equator flow in spring (**Figure 4.4e, f**), although the magnitude is not as strong as spring meridional mode's (**Figure 4.4a, b**).

From another point of view, the evolution of the regression of meridional winds onto the two PCs also indicates an equator-ward progression of the warmest anomaly. In spring the confluence of the northerly and southerly occurs at the far off-equator region in the South Hemisphere, over the warmest area of this season. This region of confluence advances equator-ward as the month moves along until it reaches the equator in summer. The equator-ward progression of the confluent region suggests an equator-ward evolution of the warmest anomaly, which is consistent the Hu and Huang (2007), who report a coherent warming/cooling extending from the Angola coast toward the equator in the Gulf of Guinea.

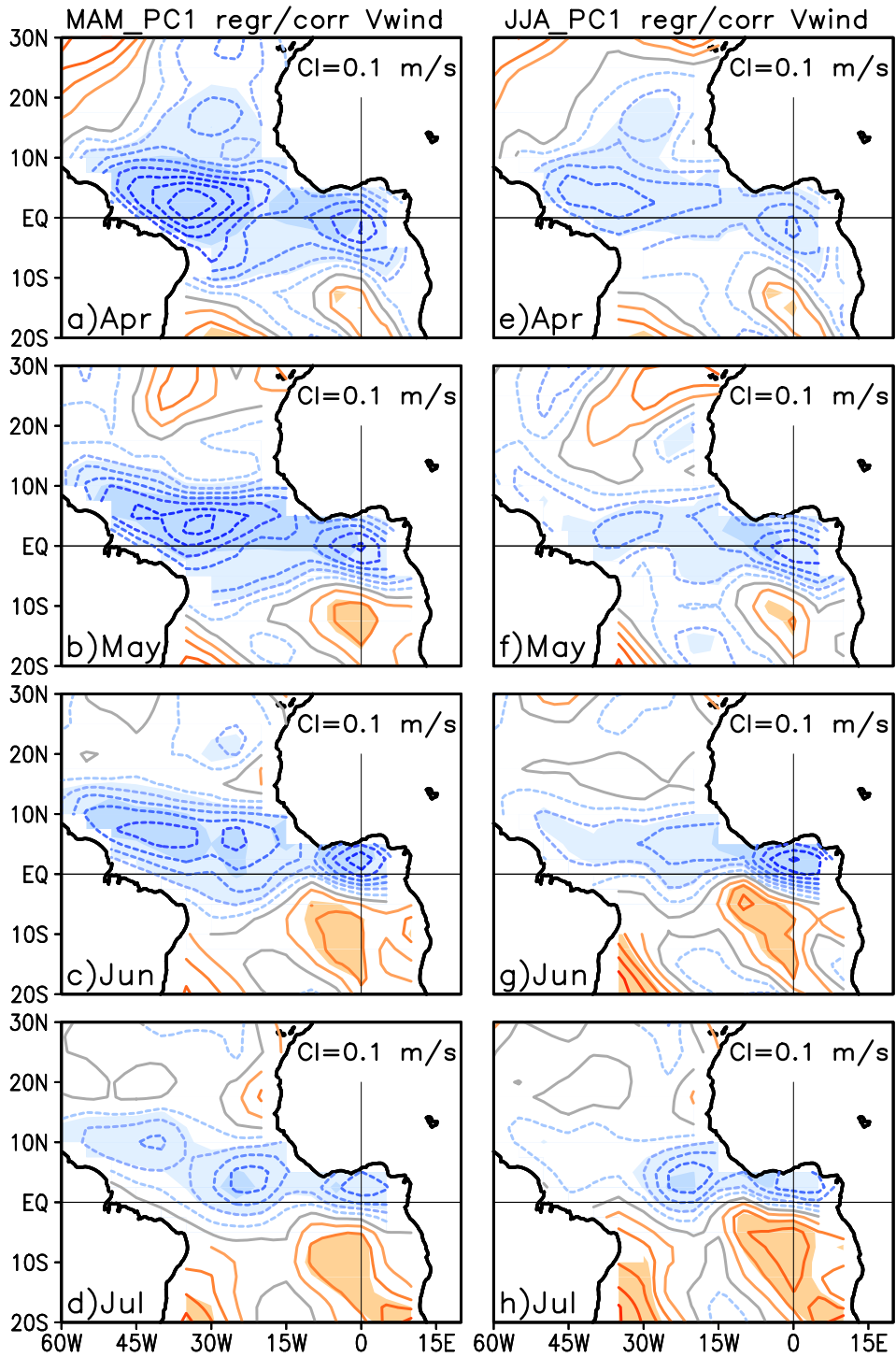


Figure 4.4 Regression maps (contours) of meridional winds onto MAM PC1 (left panel), and onto JJA PC1 (right panel). Shading indicates significant correlation (above 95% level).

Zonal wind anomaly in the western equatorial region is important in the formation of the equatorial mode (Zebiak 1993), therefore the summer equatorial mode is highly associated with the zonal wind anomalies in the western equatorial basin as shown in **Figure 4.5f, g, and h**. Equatorial zonal wind anomaly is related to the zonal mode starting as early as May, about one month before the equatorial thermocline in the east starts its seasonal shoaling in summer. This result is in accordance with the ocean dynamics that the equatorial Kelvin waves take about three to four weeks to travel from the west to the east (Gill, 1982). Some studies have also shown zonal wind anomalies in the western Atlantic precede eastern Atlantic SSTA by about one month (Servain et al. 1982; Hirst and Hastenrath, 1983; Keenlyside and Latif, 2007).

On the other hand, surprisingly, the spring dipole mode is also markedly related to equatorial zonal wind anomaly (**Figure 4.5a through d**), especially in spring the magnitude of regression shows greater than 0.5 m/s in some region (while the regression of the zonal wind onto the zonal mode has maximum of only 0.4 m/s). Also in spring the meridional mode is related to equatorial zonal wind anomalies almost across the whole basin. There is a roughly asymmetric pattern across the equator -- strong westerly anomaly along and south to the equator and weaker easterly north to the equator. This pattern moves northward in summer, resulting a more symmetric pattern (across the equator) of the zonal wind anomaly response in the equatorial region.

The above relationship between the two modes and the surface winds show that the wind anomaly patterns that are generally associated with one mode are in fact also related to the other mode. This is a powerful indication that there indeed exists a close relationship between the spring meridional mode and summer equatorial mode.

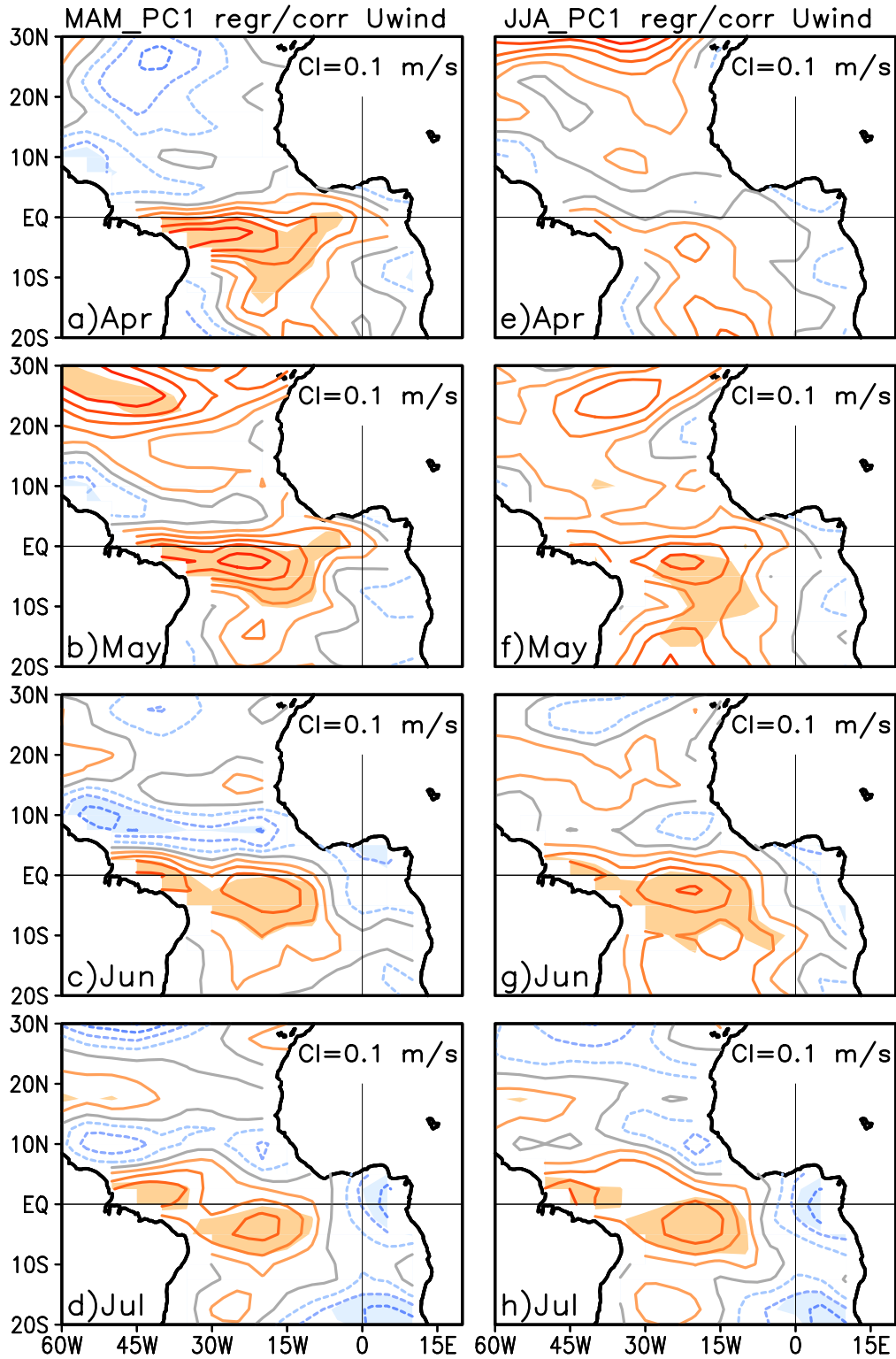


Figure 4.5 Regression maps (contours) of zonal winds onto MAM PC1 (left panel), and onto JJA PC1 (right panel). Shading indicates significant correlation (above 95% level).

As both these two modes are significantly related to the zonal wind anomaly in the western equatorial region starting from May, we define an index of equatorial zonal wind anomaly in May in the region between 45°W-20°W and 5°S-2.5°N (see the green box in **Figure 4.6c**) by averaging May zonal wind anomaly of this region, then regress (and correlate) the monthly SSTA onto this index. The results show that in April, May, and Jun (**Figure 4.6b, c, and d**), this index of May equatorial zonal wind is related to a dipole pattern of SSTA, although the response at the equator and the south gradually strengthens while the response in the north approximately remains its magnitude. In July and August (**Figure 4.6e, f**), the response in the north recedes rapidly, and the response in the equator and the south also diminishes, but in a slower rate, resulting a predominant equatorial pattern. Many studies have shown that equatorial zonal wind anomalies in the western basin play a crucial role in the formation of the equatorial mode (Servain et al. 1982; Hirst and Hasternrath 1983; Keenlyside and Latif 2007), and here we see that the regression patterns of SSTA onto the May-zonal-wind index indicate a dipole-to-zonal evolution that echoes the high correlation between the PCs derived from the EOF analysis.

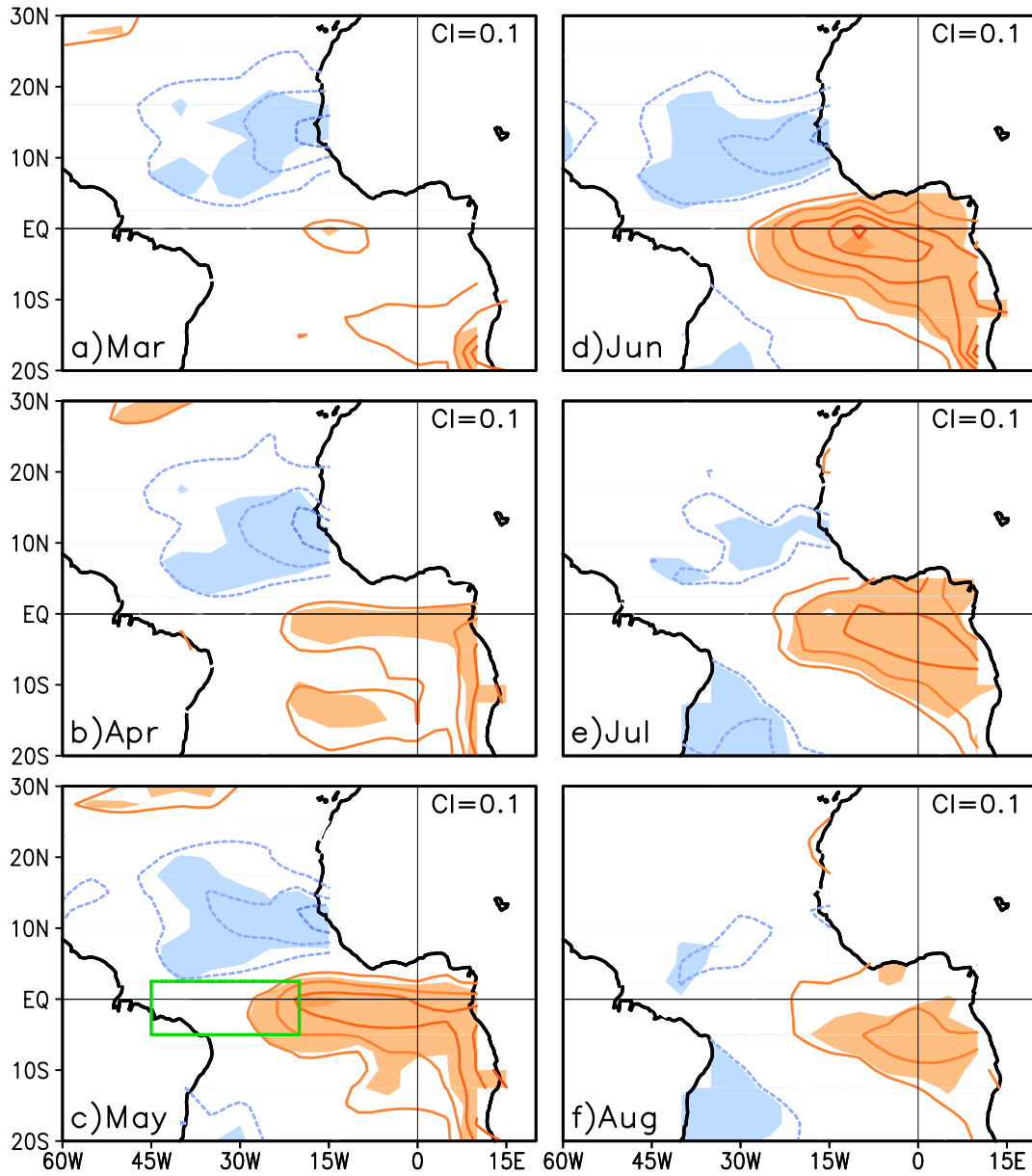


Figure 4.6 Regression maps of SST anomaly (contours) onto the May west-equatorial zonal winds. Shading indicates significant correlation (above 95% level). Contour intervals: 0.1°C.

e. Regression and correlation with SSTs

The regression patterns of the SSTs onto the spring dipole PC (**Figure 4.7**, left panel) are basically dipole patterns; however, the south lobe grows as the north lobe decays,

indicating a tendency for the dipole mode evolving into equatorial mode. On the other hand, the regression patterns of precursory SSTs onto the summer equatorial PC do not have a dipole pattern (**Figure 4.7e, f**). This suggests that spring meridional mode can lead to the summer equatorial mode, but summer equatorial mode does not have to be resulted from the spring meridional mode.

Figure 4.7 also points out an interesting aspect that although spring meridional mode has a dipole pattern; however, the SST patterns related to this mode indicate that the north lobe and south lobe behave out of phase from April to June. When extending the lead-lag regression between spring meridional mode and SST of other months, the results indicate that the north lobe and south lobe grows coherently from January to April (not shown). This suggests that some external modulation to the spring dipole mode may exist, such as NAO or ENSO. We extend the domain for the SST regression to the high-latitude of North Atlantic, the pattern has a tri-pole pattern that resembles the NAO influence for the precursory and contemporary SSTs (**Figure B.0.2a** and **Figure B.0.3a**), indicating the NAO may force or modulate the meridional mode in boreal winter and spring. The correlation between Jan-Feb-Mar-averaged NAO index and the spring meridional PC is significant (but not high, 0.34), supporting this idea.

On the other hand, the SST (of the extended domain) regression onto the summer equatorial PC does not resemble the NAO influence at any month of the year (e.g. **Figure B.0.2d** and **Figure B.0.3d**), and the correlation between the NAO index and summer equatorial PC is very little (0.09), consistent with the result of SST regression patterns. These results suggest that the connection between the spring meridional mode and

summer equatorial mode is not governed by the NAO, either; local air-sea interaction is mainly responsible for this modal relationship.

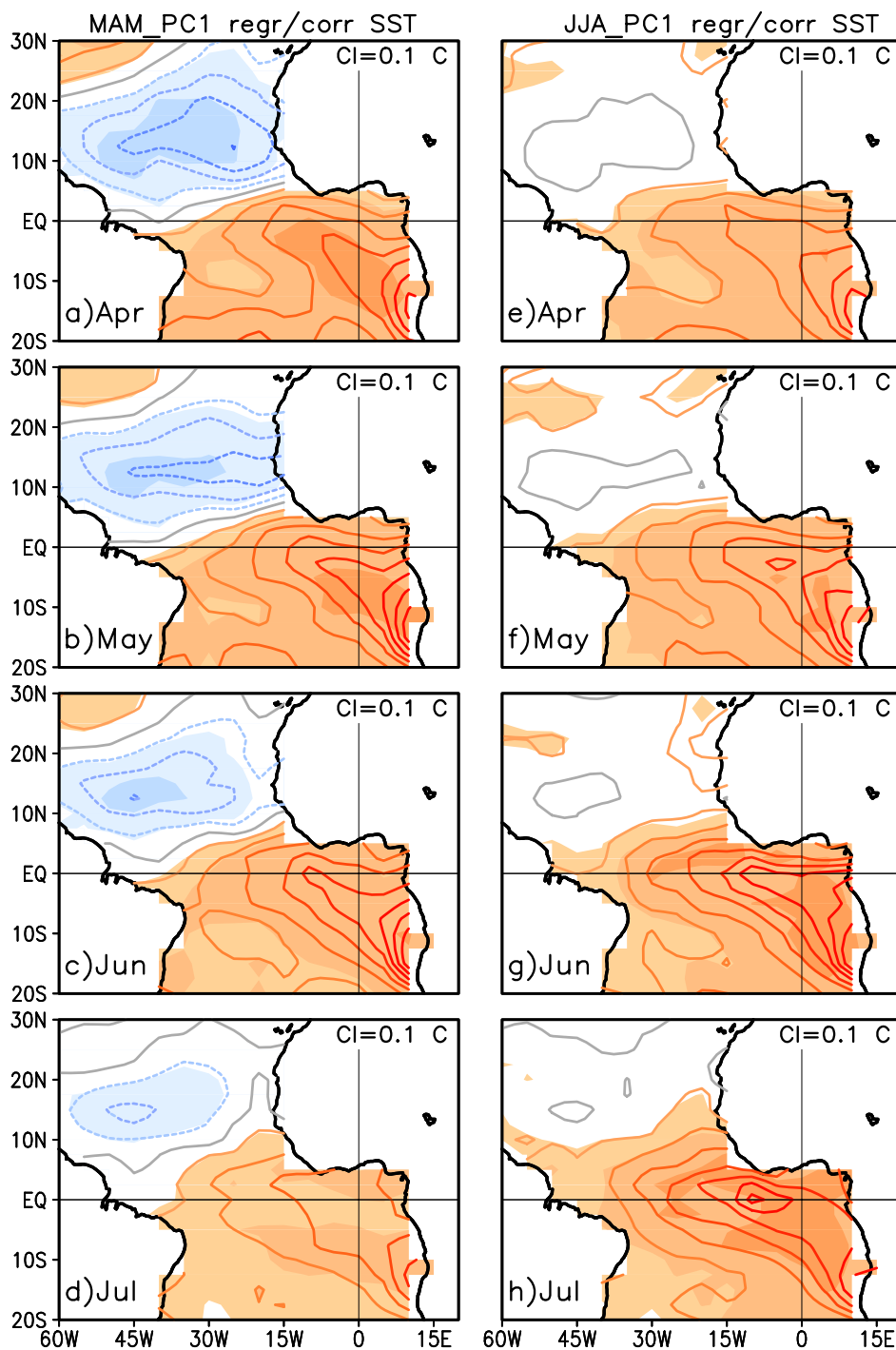


Figure 4.7 Regression maps (contours) of SSTs onto MAM PC1 (left panel), and onto JJA PC1 (right panel). Shading indicates significant correlation (above 95% level).

4.4. Mechanism supporting the model relationship

Spring dipole mode is related to equatorial zonal wind anomaly as early as April and this response persists into summer (**Figure 4.5**, left panel). On the other hand, zonal mode is significantly related to equatorial zonal wind anomaly starting from May (**Figure 4.5f**); these zonal wind anomalies play an important role in the formation of the equatorial mode (Carton and Huang 1994; Keenlyside and Latif 2007). We therefore have the hypothesis as the following: If the presence of dipole mode can result in equatorial zonal wind anomaly in spring, as long as this zonal wind anomaly remains at least into May (which is indeed the case as shown in **Figure 4.5** left panel), then this zonal wind anomaly can lead to the zonal mode in summer. Another required condition is the corresponding relationship between the phase of the dipole mode and the direction of zonal wind anomaly. Cold-north/warm-south of dipole mode causes westerly anomalies along the equator, so that the westerly anomalies can further warm the eastern equatorial region. Likewise, warm-north/cold-south will cause easterly anomaly along the equator, which can cool the equator further more.

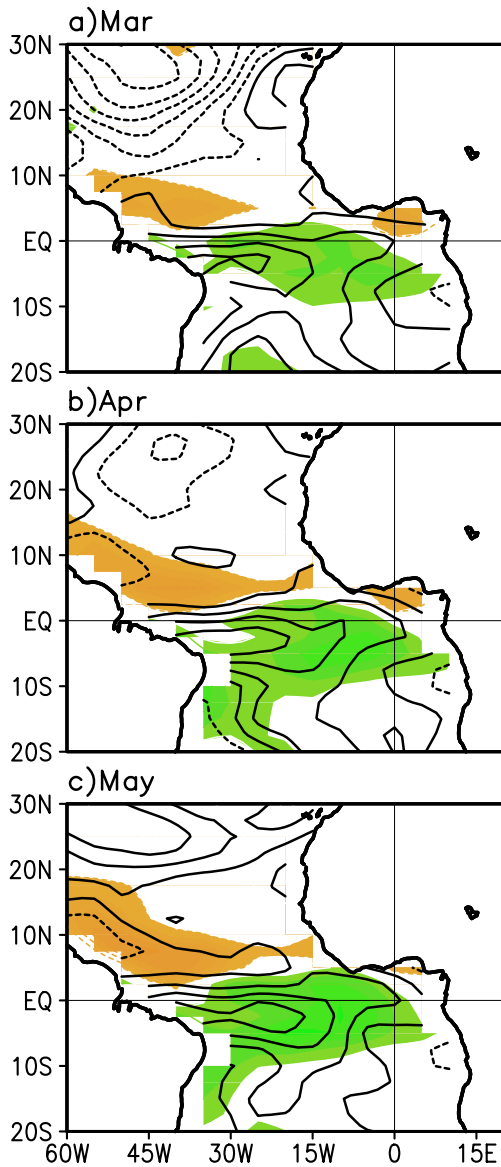


Figure 4.8 Regression maps of monthly zonal winds (black contours) and monthly rainfall (green/yellow shading) onto the MAM PC1.

Comparing the left panels of **Figure 4.4** and **Figure 4.5**, one can see that spring dipole mode has stronger equatorial zonal wind response when there is a strong cross-equator flow. This leads to the thinking that the ITCZ may play a role in the excitation of the equatorial zonal wind anomaly in spring (also as suggested by Servain et al. 1999, 2000 and Martugudde et al. 2001). **Figure 4.8** shows simultaneously the regression of

monthly rainfall and zonal wind anomalies onto the spring dipole PC. Indeed there is a very good correspondence between the directions of zonal wind anomalies and the signs of the rainfall anomalies near the equator: Near the equator, westerly (easterly) anomalies occur in the region of positive (negative) rainfall anomaly. The climatological ITCZ in this season is located near the equator, but still in the north hemisphere. Henceforth the anomaly pattern of rainfall is approximately asymmetric to the equator -- excessive rainfall in one hemisphere and deficient in the other. Positive rainfall anomaly represents extra latent heating, and negative for latent cooling. Therefore **Figure 4.8** indicates that near the equator, westerly anomaly occurs in the region of heating and easterly anomaly in the region of cooling. When the season progresses into summer, the climatological ITCZ moves northward, therefore the nodal line of the positive/negative rainfall anomaly also shifts northward. This is consistent with the result in **Figure 4.5**: the zonal wind response moves northward as the season moves into summer. The relation between westerly wind anomaly and heating is consistent with the Gill model for the circulation resulted from heating (Gill 1980). In Gill's model a low pressure center occurs west to the heating center in the pole-ward direction, therefore resulting in the westerly near the equator in the hemisphere of heating.

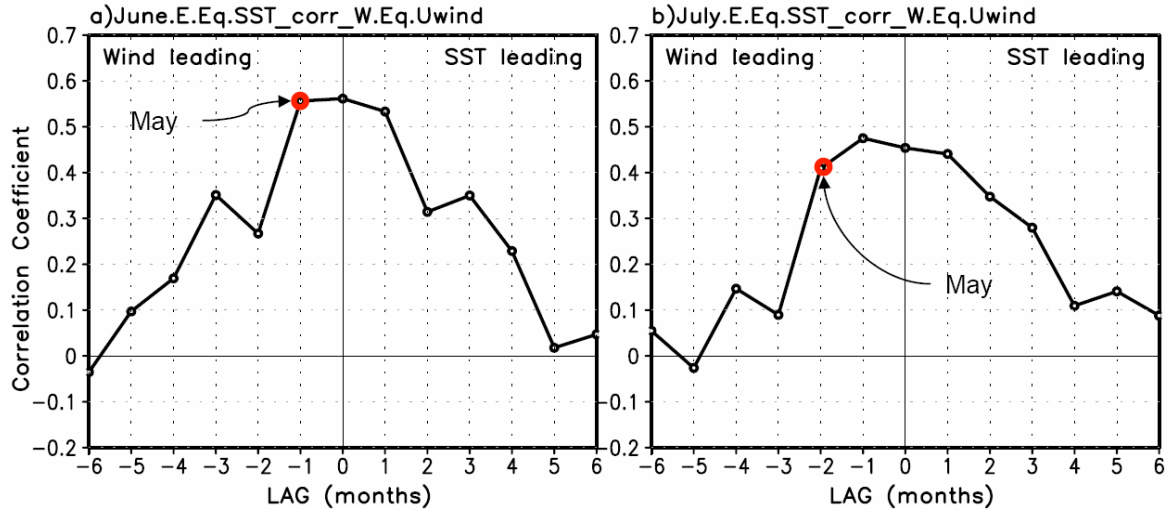


Figure 4.9 Lead-lagged correlation between the west equatorial zonal winds and the a) June and b) July eastern equatorial SST.

Based on Gill’s model, one can argue that when the ITCZ is shifted southward by the pressure gradient force due to cold-north/warm-south of dipole SST anomaly in spring, extra rainfall anomaly occurs on and south to the equator, and thus westerly anomaly occurs along and near the equator, which will further warm up the equator in summer. The same argument (but with opposite sign for the equatorial wind anomaly) goes along for the opposite sign of dipole anomaly in spring.

In particular, the zonal wind anomaly in May is especially important. Both June and July the SST anomalies in the eastern equatorial region have high correlation with the monthly western equatorial zonal wind anomaly starting from May (**Figure 4.9**). The high correlations between the eastern equatorial SSTA and the western zonal wind anomaly from May through July (or August) indicate the effectiveness of Bjerknes feedback between the SST and the zonal winds during this period of the year. May is the time of the start-up of the significant Bjerknes feedback. Therefore as long as the zonal wind anomalies resulted from the anomalous latent heating persist into May (which is true

as shown in **Figure 4.5**), the Bjerknes feedback can come into play and lead to the equatorial mode in summer. **Figure 4.9** also echoes the result that summer equatorial mode has significant correlation with the zonal wind anomalies starting from May (**Figure 4.5f**).

4.5. The modal relationship and prediction of summer West African rainfall

Rainfall variability over the Coast of Guinea is known to be highly related to the SST variability over Tropical Atlantic (Hirst and Hasternrath 1983; Giannini et al. 2003); this relationship is most prominent in boreal summer (**Figure 4.10**, right panel). The lead-lag regression between African rainfall and the zonal PC shows that in March and April, West African rainfall basically has little dependence on the zonal mode (**Figure 4.10d**); in May and June, right on the equator and around 10°N, some connection between the rainfall and the summer zonal mode builds up but only in very limited areas along the coast (**Figure 4.10e**). In July and August a strong connection between zonal mode and the rainfall occurs throughout the Guinea Coast (**Figure 4.10f**, same as **Figure 4.2b**), with a weaker and opposite-sign of regression along the belt of Sahel region, which, in some sense, resemble the well-known dipole pattern of the rainfall anomaly over this region. The dipole rainfall anomaly pattern is the leading EOF pattern for this area in this season, and the pattern can be seen sometimes in the pure anomaly (Nicholson and Webster 2007; Cook and Vizu 2006).

Interestingly, this evolution of the relationship between the African rainfall and the summer zonal mode can be almost reproduced using the spring dipole mode (**Figure 4.10**,

left panel). Most importantly, the high regression between the spring dipole PC and the July-August rainfall implies a possibility of predicting rainfall using spring-time Tropical Atlantic SST. The climatology of the rainfall in this region in summer is about 6 mm/day (**Figure 4.11b**), and the regression of the rainfall onto summer zonal PC is about 1.2 mm/day, 20 % of the climatology, which is very significant. The regression of summer rainfall onto the spring dipole PC is close to 1 mm/day. That is, even using the spring dipole mode that leads the rainfall by two or three months, it still explains quit significant variance of the summer African rainfall.

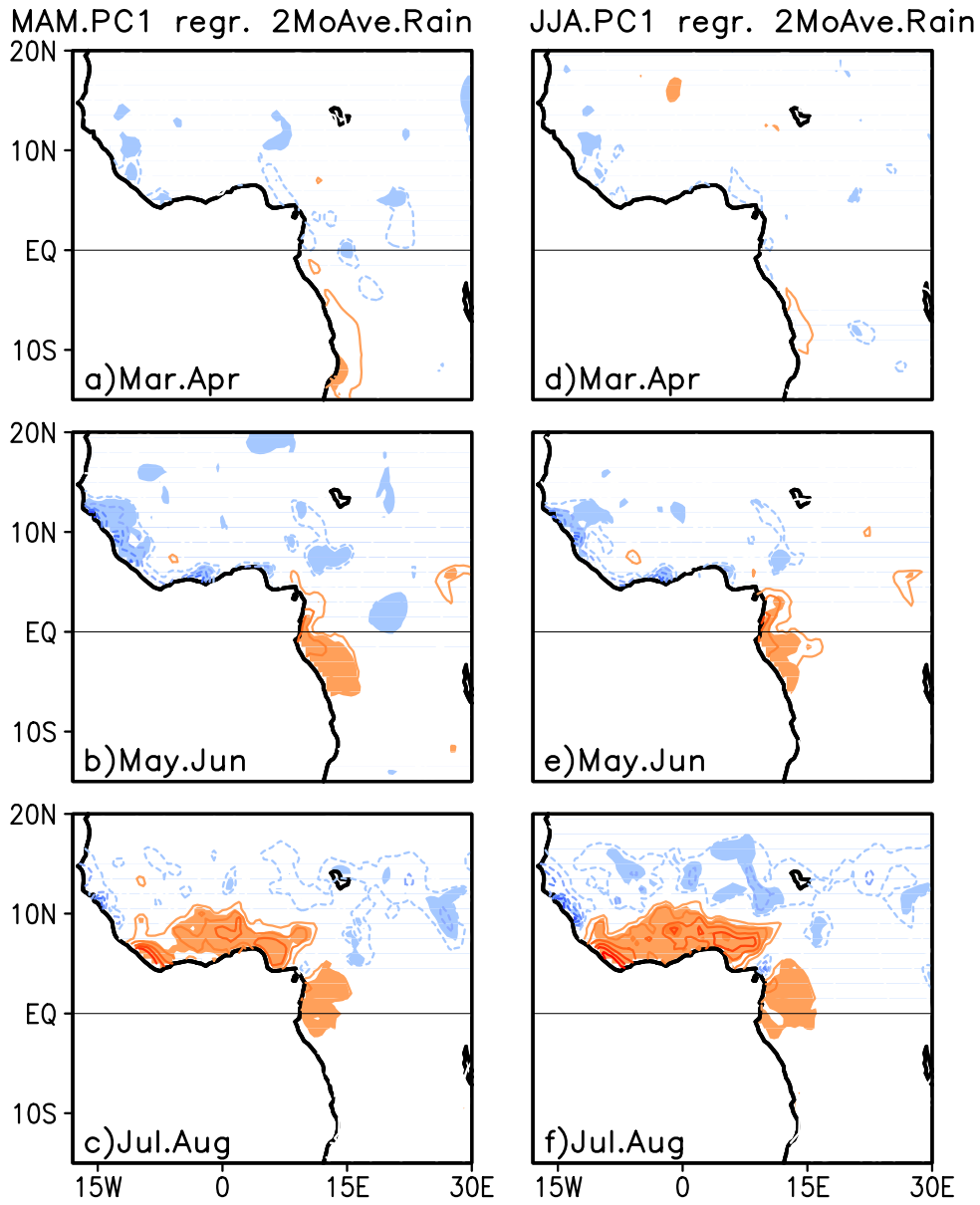


Figure 4.10 Regression (contours) between African rainfall (2-month-averaged) and MAM PC1 (left panel), and between African rainfall and JJA PC1 (right panel). Shading indicates significant correlation (above 95% level). Contour intervals: 0.3 mm/day.

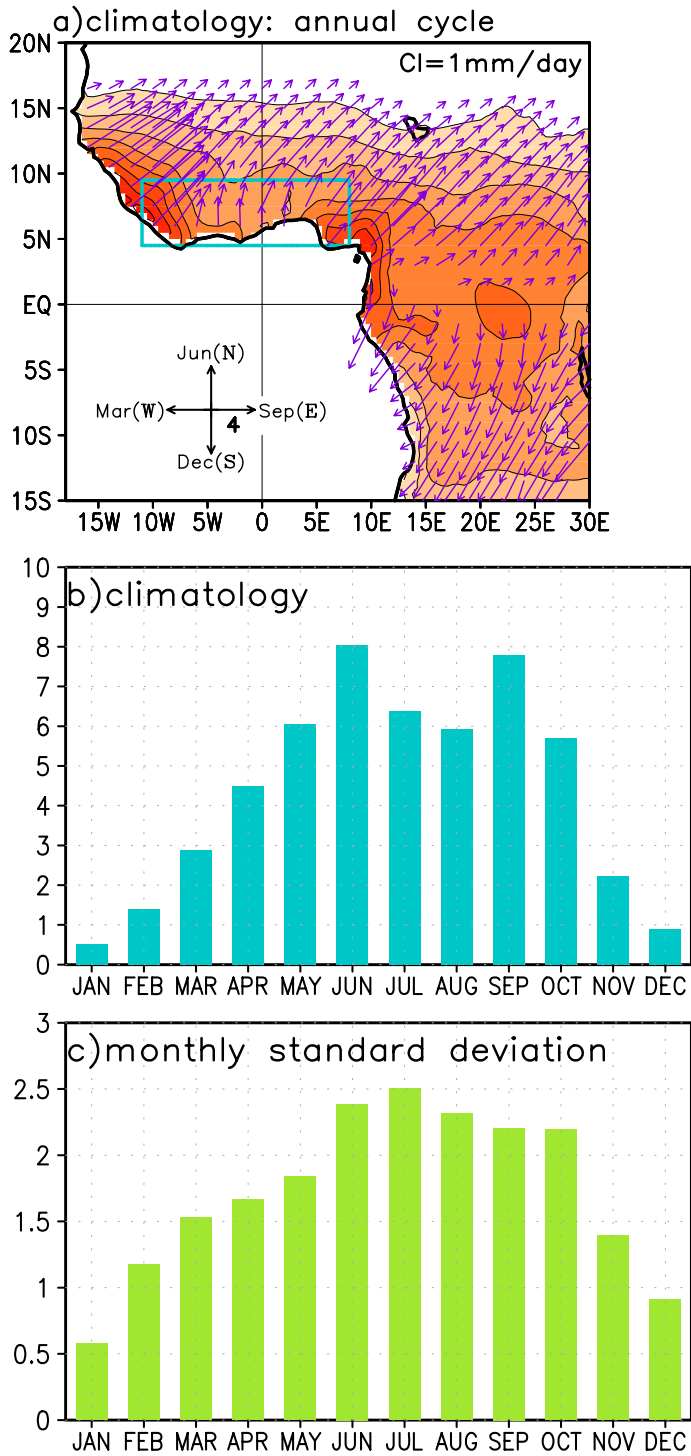


Figure 4.11 a) West African rainfall climatology: contours: annual mean; vectors: amplitude and phase of the first harmonics of climatology. The vectors point to the time when the peak of the annual cycle of climatology occurs. b) Area averaged climatology of the box in a); unit: mm/day. c) Area-averaged monthly standard deviation of the box; unit: mm/day.

To further investigate the consequence of this relationship, we define an index for rainfall variability along the Guinea Coast, which is the area average of the summer rainfall (July and August) of the rainfall anomaly in the region between 11°W to 8°E and 4.5°N to 9.5°N (see the blue box in **Figure 4.11a**). This region is chosen because it is the region of highest regression/correlation between the summer rainfall and the zonal and dipole PCs.

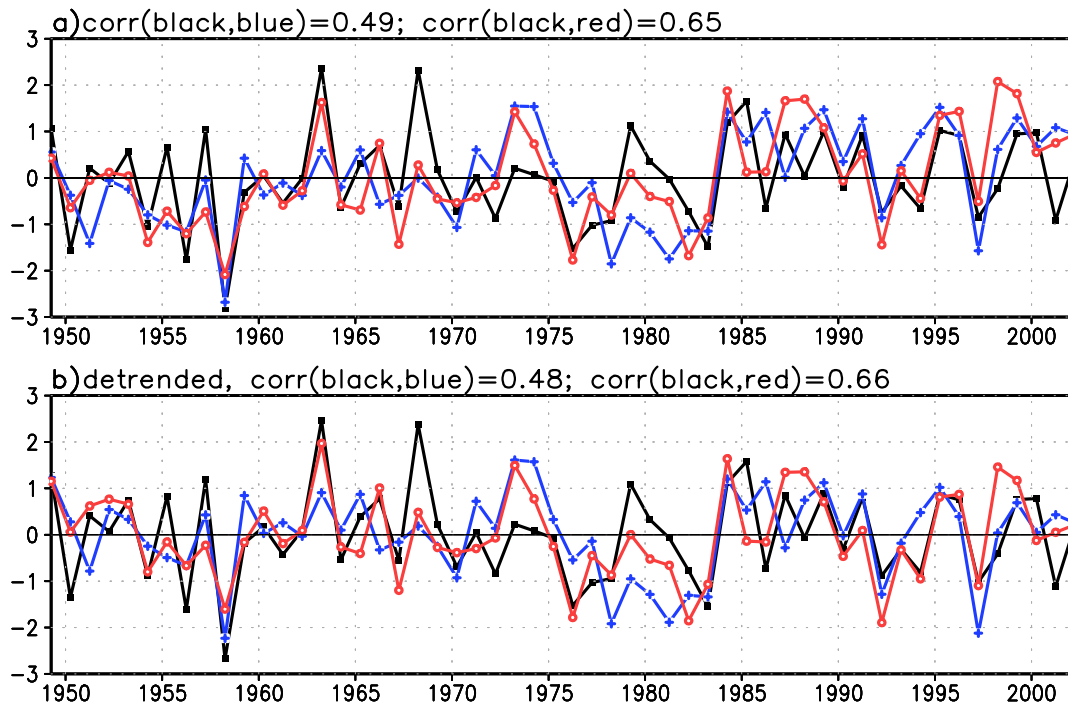


Figure 4.12 Time series of the spring dipole PC (blue) and the summer zonal PC (red) and the index of Jul-Aug rainfall anomaly of Guinea Coast (black): a) original, b) detrended.

The rainfall climatology maximizes in June right on the coast between 5°W and 5°E, which coincides with the onset season of the West African monsoon. Further inland the rainy month comes later, spreading from July to September (**Figure 4.11a**), corresponding to the seasonal northward movement of the ITCZ in this period of a year. The rainfall climatology of the box area has two peaks of the rainy months, in June and in

September. June through September is generally considered as the rainy season of this area (Fontaine et al. 1998; Cook and Vizy 2006); however there is a slight decline of rainfall in July and August (**Figure 4.11b**). Nevertheless, July and August stand for two of the months that have greatest variance in rainfall (**Figure 4.11c**). Therefore, predicting rainfall variability in these two months can have significant social/economical influence over this region.

The index of summer rainfall over Coast of Guinea is indeed highly correlated with both the summer zonal PC and the spring dipole PC, with correlation coefficients as 0.65 and 0.49, respectively (**Figure 4.12a**). We also de-trend all the three time series and the correlation coefficients remain high and stable (0.66 and 0.48, see **Figure 4.12b**). Therefore it is not the long term trend that governs this relationship between the SSTA and rainfall anomaly. The same calculation is repeated for some sub-regions inside the box. The results prove that the correlation is not sensitive to the chosen sub-regions (not shown), remaining about 0.65 for the summer zonal PC and 0.50 for the spring dipole PC, no matter it is de-trended or not. These results indicate that summer zonal mode can explain about 42% - 44% of the rainfall variance in July-August, and that spring dipole mode explains about 24%, more than half of that explained by the summer zonal mode.

To understand how well the prediction skill is when using the spring Atlantic SST, we investigate the correlation coefficients between the rainfall index and the PCs of the first four modes derived from EOF analysis. We found that in both season there is another mode, EOF3, that is also highly related to the Jul-Aug Coast of Guinea rainfall. The third EOFs of spring and of summer resemble each other in the EOF patterns, except in the eastern equatorial area where the summer EOF3 has much stronger amplitude than the

spring EOF3 does (**Figure A.0.1d, e**). Interestingly, the PCs of these two modes are also highly correlated to each other (correlation coefficient is 0.76). The correlation coefficients between the Jul-Aug Coast of Guinea rainfall and the summer PC3 and spring PC3 are 0.41 and 0.39, respectively, which is about 15% of the total summer rainfall variance (**Table 4.1**). The large amplitude in the eastern equatorial region of the summer EOF3 is consistent with its high correlation to the Jul-Aug Guinea Coast rainfall variability.

Combining EOF1 and EOF3, Summer Atlantic SST explains about 60% of the summer rainfall variance, and spring Atlantic SST does about 40%. It has been shown that Pacific and Indian Oceans also have quite some influence on the African rainfall variability; in fact, SSTs all over the global tropics and subtropics can affect the African rainfall variability (Rowell et al. 1995; Fontaine et al. 1998). Therefore that the contemporary Tropical Atlantic SSTA alone can explain 60% of the summer African rainfall variance is substantial and that predicting 40% of the rainfall variance using *only* Tropical Atlantic SSTA with *one season in advance* is rather significant and promising.

	Contemporary PCs and summer rainfall index		PCs leading summer rainfall index	
	JJA PC1 (zonal mode)	JJA PC3	MAM PC1 (dipole mode)	MAM PC3
No de-trending				
Correlation (r)	0.65	0.41	0.49	0.39
Explained variance (r^2)	0.42	0.16	0.24	0.15
Sum of variance	0.58		0.39	
De-trended				
Correlation (r)	0.66	0.47	0.48	0.43
Explained variance (r^2)	0.44	0.22	0.23	0.18
Sum of variance	0.66		0.41	

Table 4.1 Correlation coefficients between the PCs and the summer Guinea Coast rainfall index. Shaded numbers are those also shown in **Figure 4.12**.

4.6. Summary and concluding remarks

This study shows the spring meridional mode and the summer equatorial mode of Tropical Atlantic variability to be strongly connected. The spring meridional mode can lead to the summer equatorial mode: Cold-north/warm-south SST dipole anomaly in spring leads to a warm phase of the equatorial mode in summer, and vice versa. This link can be attributed, at least, partly to the meridional movement of the ITCZ and the resultant latent heating (cooling) anomalies from excessive (deficient) rainfall. Consistent with Gill's model (1980), the westerly wind anomalies occur along and to the south to the equator when the ITCZ is southward shifted, leading to warmer SSTs in the eastern equatorial region through the Bjerknes feedback. Similar arguments apply for the opposite phase.

The meridional mode is generally associated with the cross-equator flow, and the equatorial mode with zonal winds in the western basin. In this study, we show the wind anomalies associated with one mode to be, in fact, also related to the other mode: The summer equatorial mode is related to the cross-equatorial flow in spring, and the spring-time meridional mode to the equatorial zonal wind in the April-onward period. This is another powerful indication, besides high correlation of the PCs, of the close relationship between the springtime meridional mode and the summertime equatorial mode.

A large fraction of the variance of the summer equatorial mode can be attributed to the spring meridional mode. The equatorial mode, however, remains susceptible to other influences generating zonal wind anomalies in the western equatorial Atlantic, such as

ENSO. In other words, while the meridional mode can lead to the summer equatorial mode, this is not the only evolutionary pathway for the equatorial mode.

Our analysis shows the spring meridional mode to be modestly linked to precursor NAO variability but the summer equatorial mode shows no such linkage. While the spring meridional mode may be influenced by NAO, its relationship with the summer equatorial mode is not orchestrated by NAO. NAO's influence on the spring meridional mode is in accord with the notion that middle and high latitude climate variability can affect tropical climate (Vimont et al., 2001; Chiang and Vimont, 2004).

It is interesting that Pacific ENSO's influence on the western Atlantic perturbs the evolutionary link between the spring meridional and the summer equatorial modes. Barreiro et al. (2005) showed ENSO's influence to both reinforce and diminish tropical Atlantic variability. Chang et al. (2006) attribute the fragile relationship between ENSO and the Atlantic Nino to the destructive interference between ENSO-related atmospheric and oceanic processes. These analyses indicate that ENSO's influence on the tropical Atlantic depends on the relative strengths of various processes. The resulting complexity partially decouples the evolutionary link between the two TAV modes; as a result, removing ENSO influence solidifies the modal connection.

Power spectrums of the PCs of these two modes show that these two modes both have strong amplitudes on the decadal (13-14 year) and interannual (3-6) timescales⁶ (**Figure 4.13**), therefore the high correlation between them also comes from the decadal and interannual signals, which is consistent with Servain et al. (1999, 2000). Even though the meridional mode is generally know to be more at decadal timescales and the

⁶ With limited number (54) of points in the time series, power spectrum analysis will not be able to resolve the detailed structure of the spectrum; nevertheless it can still point out the main timescales of the PCs.

equatorial mode interannual timescales. This does not exclude the possibility of the modes' acquiring signals of other timescales. The power spectrum shows that both modes have decadal and interannual signals and therefore they can be related on these timescales.

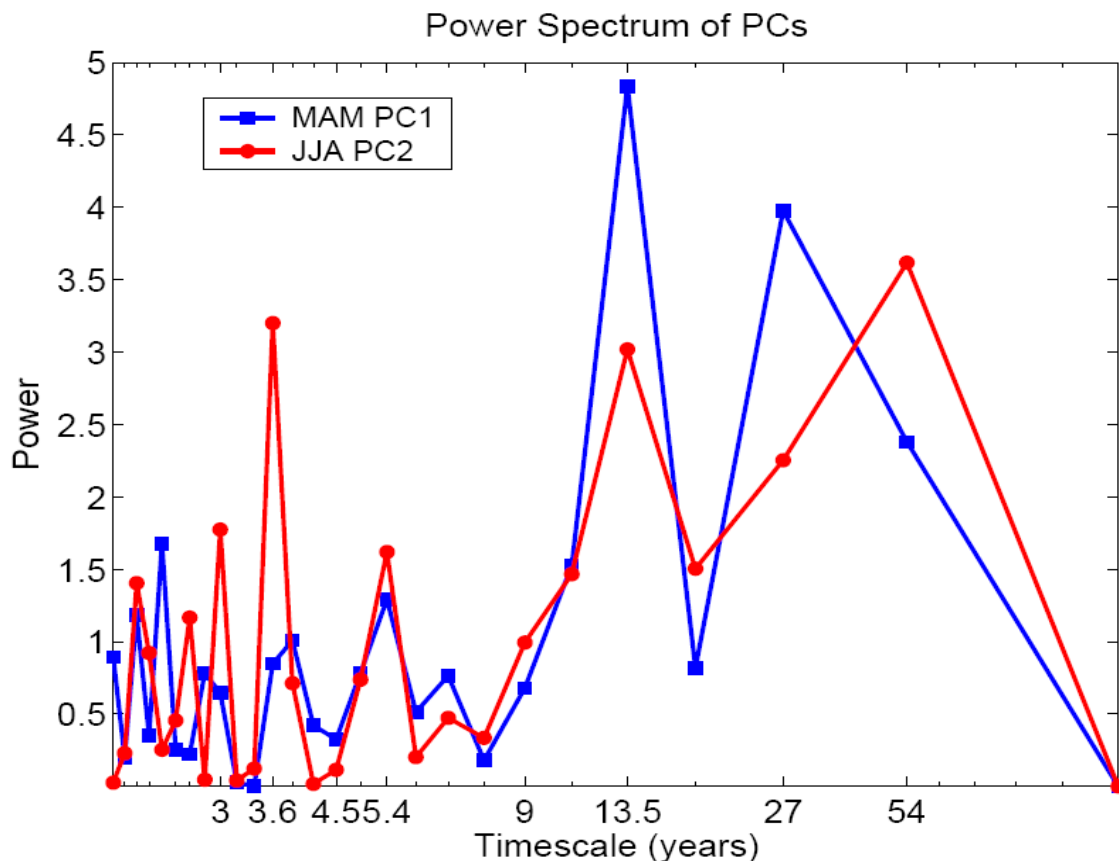


Figure 4.13 Power spectrum of spring dipole PC (blue) and summer zonal PC (red).

Regarding precipitation impacts, Fontaine et al. (1998) show that summer rainfall along the Guinea Coast is essentially related to the precursory (April-May-June) equatorial and southern Atlantic SST anomalies. These SST anomalies are elements of an EOF pattern obtained from analysis of global all-month SSTA. Fontaine et al.'s analysis, however, shows the rainfall-SST correlation to decrease with contemporary (July-August-September) SST anomalies – in contrast with our analysis where the contemporary

correlation is higher. The higher correlation likely results from the confinement of the SST EOF analysis to individual seasons.

Nicholson and Webster (2007) have recently shown that the dry years of the Guinea Coast region are related to a strengthened low-level jet-like westerly wind over West Africa that pushes the African Easterly jet northward and increases inertia instability over the Sahel region. Our analysis is apparently consistent with their findings: a cold phase of the summer equatorial mode increases the meridional surface pressure gradient over West Africa, and the low-level jet-like westerly wind strengthens (not shown) while the Guinea Coast region is dryer than usual. This strengthening or weakening of the westerly winds can be predicted using the spring dipole PC.

The evolutionary link between the two TAV modes, indeed, enhances the prospects for prediction of boreal summer rainfall over the Coast of Guinea. It is also shown that there is another mode in each season that is also highly related to the rainfall over the Coast of Guinea. As a result, contemporary Tropical Atlantic SSTAs can explain 58%-66% of the summer rainfall variance along the Guinea Coast. The seasonal-leading (or precursor) SSTAs can predict about 40% of the summer rainfall variance.

Lee and Wang's (2008) recent modeling analysis shows that either phase of a dipole mode leads to a warm equatorial mode (i.e. Atlantic Nino) on decadal timescales, through equatorial oceanic gyre circulation and the Bjerknes feedback. Although their analysis also links the two TAV modes (as in our study), the relationship they uncover is asymmetric, in that both phases of the dipole mode lead to a warm equatorial mode; quite unlike our observational based finding of a one-to-one correspondence between the phases of the two modes (cold-north dipole leading to the Atlantic Nino, and vice-versa).

Lee and Wang's model based findings are not supported by observational analysis. Modal correlation should be very weak under Lee and Wang's scenario where both phases of the dipole mode are linked with the same phase of the equatorial mode; not the case as reported here and in observation studies of Servain et al. (1999, 2000) and Murtugudde et al. (2001) and our study. Their proposed mechanism can however partly account for the correlation drop during 1949-2000 in Murtugudde et al.'s (2001) study. As indicated by our analysis, the strong modal connection in observations results from anomalous rainfall (and related latent heating). Under-representation of the latter in model simulations or its weakness in observational sub-records can lead to weaker modal links.

The mechanism advanced by Lee and Wang (2008) operates mainly on decadal timescales in their model, but a similar mechanism can be easily envisioned to operate on interannual timescales as well. The mechanism will constructively interfere with the evolution of the cold-north/warm-south dipole, and destructively with that of the one in the opposite phase. This should lead to asymmetry in the warming/cooling rates and the strength of the equatorial mode: larger warming rate and stronger amplitude for warm events, and smaller cooling rate and weaker amplitude for cold events. This asymmetry is indeed noted in **Figure 4.14**, which shows the warming rate of warm events to be greater than the cooling rate of the cold events, and the warm events to attain stronger strength. The result holds in analysis of de-trended SSTA (not shown).

Our analysis shows the spring meridional mode to be highly correlated to summer equatorial mode, suggesting that the former leads to the latter. However, this does not exclude other SST anomaly structures from evolving into the equatorial mode, nor the equatorial mode from evolving into the meridional mode (Servain et al., 1999 and 2000).

Okumura and Xie (2006) have recently noted the relationship of anomalous warm/cold events in the eastern equatorial Atlantic in November-December to the following spring's SST dipole pattern, consistent with the results of Servain et al..

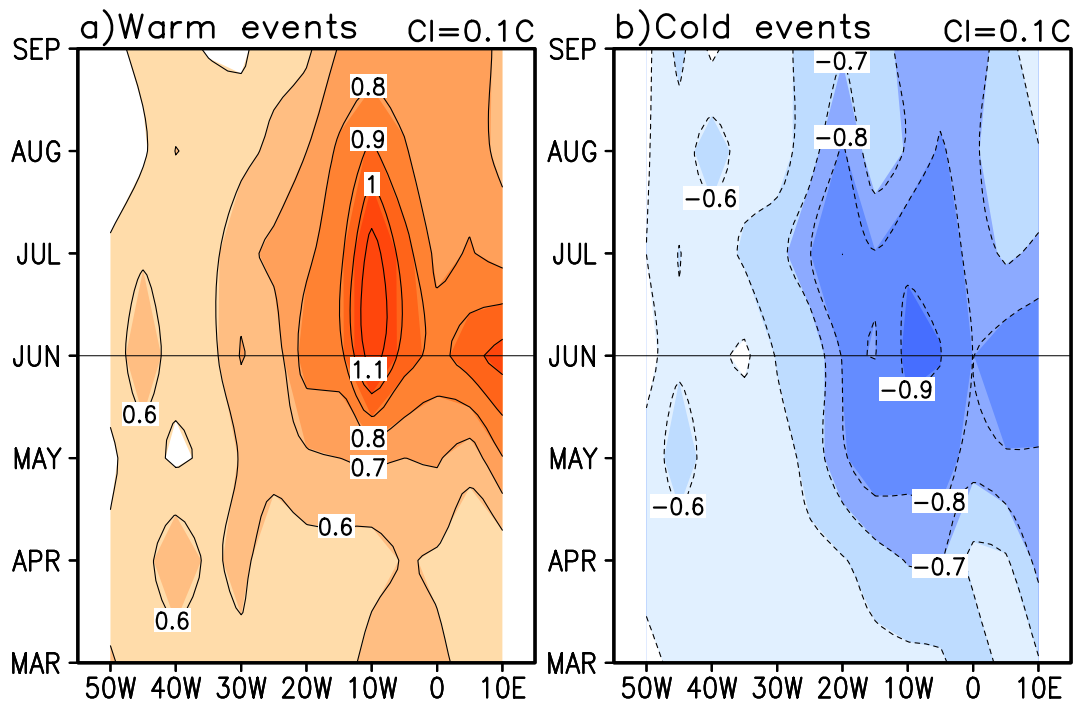


Figure 4.14 Time evolution of a) warm events and b) cold events at the equator. Only warm anomalies warmer than 0.4 °C and cold anomalies colder than -0.4 °C are included in the calculation.

5. Summary and Concluding Remarks

The theme of this dissertation is the relationship among the meridional dipole pattern of SST, the equatorial zonal wind, and the equatorial SST, for both the CCSM3 model biases (Chapter 2) and the natural climate variability (Chapter 4) over the Tropical Atlantic sector. It is shown that there is a similar relationship between these two phenomena in both the model bias and the year-to-year climate variability.

Chapter 2 documents the bias structures of the seasonal cycle of the CCSM3 (coupled) and CAM3 (atmosphere only) models and proposes some possible causes of the biases. The CCSM3 has a dipole-like pattern with a cold bias in the northern Tropics and a warm bias in the southeastern Tropics, which is reminiscent of the meridional mode of the observed climate variability in boreal spring. Along the equator, in contrast, in boreal spring CCSM3 exhibits striking westerly winds with easterly winds in the upper troposphere, in turn similar to the equatorial mode of climate variability in boreal summer. Westerly winds cause a deepening of the eastern thermocline that keeps the east warm despite enhanced coastal upwelling. Thus, the bias of the seasonal cycle in the coupled model appears to project at least partially onto the spatial patterns of natural climate variability in this sector.

Information about the origin of the bias in CCSM3 is deduced from a comparison of CCSM3 with a simulation using specified historical SST to force the atmospheric component of the CCSM3-- the CAM3 model. The patterns of bias in CAM3 resemble those apparent in CCSM3, including the appearance of substantially intensified subtropical bands of SLP, indicating that the problem may be traced to difficulties in the

atmospheric component model. Positive SLP bias also appears in the western tropical region, which may be related to deficient Amazonian precipitation. The positive SLP bias seems to be the cause of the anomalous westerly trade winds in boreal spring, and those in turn appear to be responsible for the anomalous deepening of the thermocline in the southeastern Tropics.

The westerly surface winds in MAM have fundamental impacts on CCSM3-simulated climate in the tropical Atlantic sector, which can possibly further degrade the model's simulated climate over other region; for example, the Sahel desert is likely misplaced. The westerly winds deepen the thermocline in the eastern basin and result in the too weak variance of the simulated SST which has been reported by some studies (Deser et al. 2006; Breugem et al. 2006).

Chapter 3 makes the case that westerly bias in the surface winds of the CAM3 over the equatorial Atlantic in boreal spring has its origin in the rainfall (thus diabatic heating) bias over the tropical South American continent. This case is made by examination of the spatio-temporal evolution of regional precipitation and wind biases, and by dynamical diagnoses of westerly wind bias in experiments with a steady, linearized dynamical core of an atmospheric general circulation model. Diagnostic modeling indicates that underestimation of rainfall over the eastern Amazon region can lead to the westerly bias in equatorial Atlantic surface winds. The study suggests that efforts to reduce coupled model biases, especially seasonal ones, must target continental biases, even in the deep Tropics where ocean-atmosphere interaction generally rules.

Chapter 4 investigates the relationship between the leading interannual modes of Tropical Atlantic SST variability in boreal spring and summer. The spring meridional

mode and summer equatorial mode are shown to be related, with the spring meridional mode leading into equatorial mode in a corresponding phase in summer. For example, if the meridional mode is expressed as cold-north/warm-south in spring, then the summer equatorial mode has warm phase in summer; and vice-versa. This modal linkage is not orchestrated by ENSO or NAO variability.

It is proposed in this dissertation that the connection between these two phenomena is a consequence of the anomalous diabatic (latent) heating from the ITCZ rainfall due to its latitudinal displacement. The meridional location of the ITCZ is subject to the influence of the cross-equatorial pressure gradient that is related to the cross-equatorial SST gradient.

The relationship between these modes and the variability of July-August African rainfall along the Coast of Guinea is also investigated. The modal relationship enhances the prospects for prediction of boreal summer rainfall over the Coast of Guinea: with tropical Atlantic SST alone, the spring meridional mode can explain 25% of the summer-time West African rainfall variance.

Appendices

A. The second and third modes in boreal spring and summer

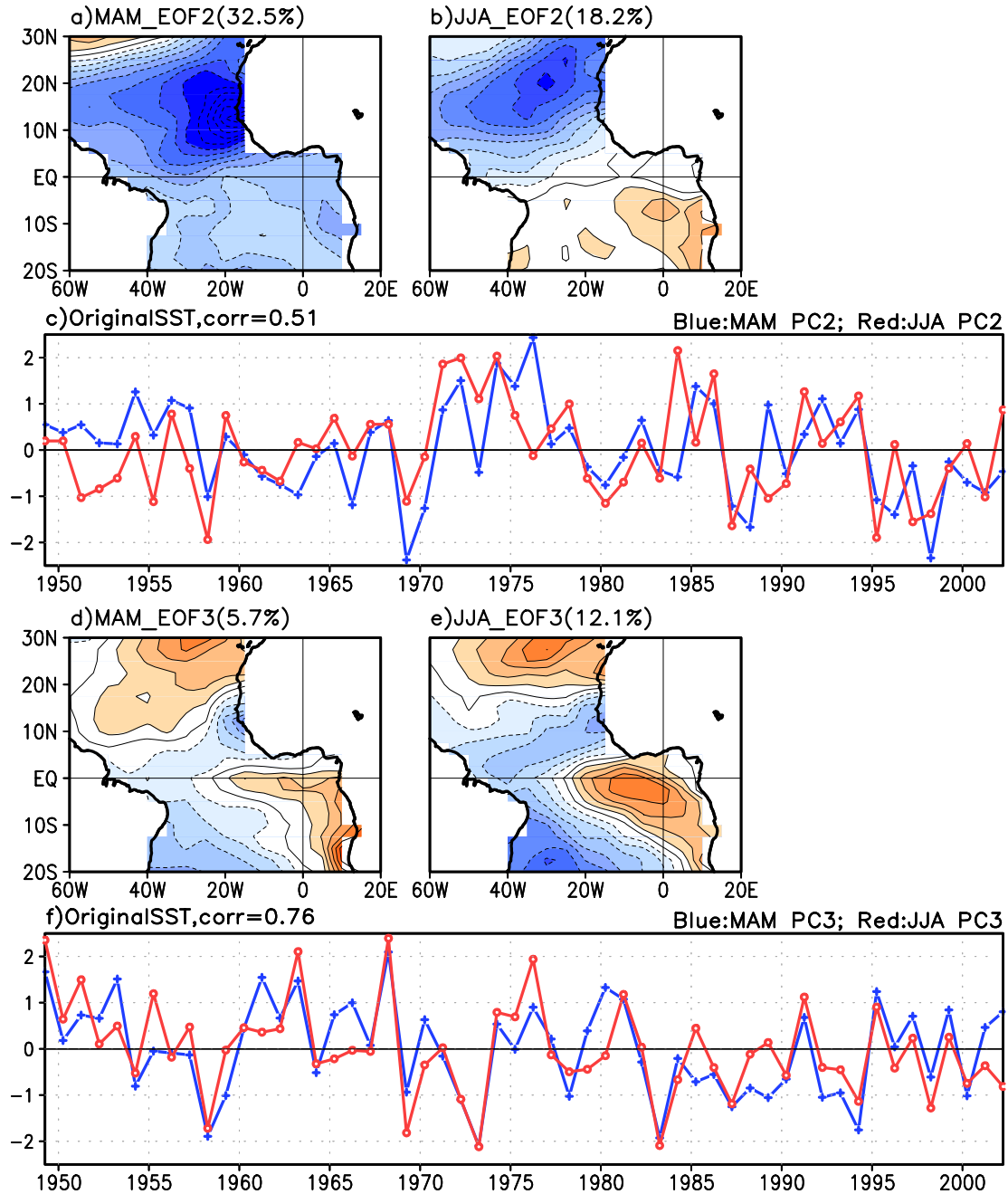


Figure A.0.1 EOF patterns and the corresponding PCs, from original SSTA: EOF patterns of the second and third modes in spring (a and d, respectively) and in summer (band e, respectively), and their PCs (c and f). Contour intervals for a, b, d, and e: 0.05 °C.

B. The relation between the North Atlantic Oscillation and the first three modes in both seasons

The coefficients of the correlation between the PCs of the EOFs and the 3-month-averaged NAO indices (**Table B.1**) show that spring PC1 and PC2 are correlated to the NAO indices in the boreal winter and early spring. Spring PC3 appears to be very little correlated to the NAO indices of any time. For the summer modes, only PC2 is significantly correlated to spring and early summer NAO indices. The results generally remain the same for the most of the detrended PCs, with some exception for the spring PC1 and summer PC3.

NAO month	Original PCs						Detrended PCs					
	MAM PC1	MAM PC2	MAM PC3	JJA PC1	JJA PC2	JJA PC3	MAM PC1	MAM PC2	MAM PC3	JJA PC1	JJA PC2	JJA PC3
DJF	-0.28	0.28	0.13	0.09	0.10	0.01	-0.23	0.33	0.09	0.02	0.10	0.07
JFM	-0.34	0.34	0.14	0.10	0.23	0.01	-0.21	0.50	0.06	-0.09	0.26	0.16
FMA	-0.27	0.30	0.15	-0.03	0.13	-0.01	-0.14	0.43	0.07	-0.23	0.14	0.12
MAM	-0.16	0.39	0.15	-0.16	0.41	0.00	-0.10	0.45	0.12	-0.26	0.41	0.06
AMJ	-0.10	0.18	0.05	-0.15	0.43	-0.14	-0.16	0.16	0.08	-0.12	0.44	-0.18
MJJ	-0.08	0.07	0.08	-0.02	0.42	-0.24	-0.14	0.04	0.10	0.04	0.42	-0.29

Table B.1 Correlation between 3-month-averaged NAO index and the PCs. Numbers in red font indicates the correlation is above 95% of significance. The shaded cases are used for plotting the correlation between the PCs and the SSTAs.

When three-month-averaged SSTAs are regressed and correlated onto the these PCs, the results are generally consistent with the correlation coefficients between the PCs and the NAO indices (**Figure B.0.2**), meaning that when the correlation coefficient is high, the pattern of the regression/correlation show a pattern that is well known as the NAO response in the North Atlantic, e.g. the tripole pattern or the horse shoe patter. These patterns indicate that NAO may play a role in generating spring EOF1, EOF2, and summer EOF2, but has much little relation to the other modes. These results remain stable

with de-trended PCs (not shown), or ENSO-removed PCs (not shown), or de-trended ENSO-removed PCs (**Figure B.0.3**). However, more detailed investigation with regard to the NAO's connection to these modes is needed for further understanding.

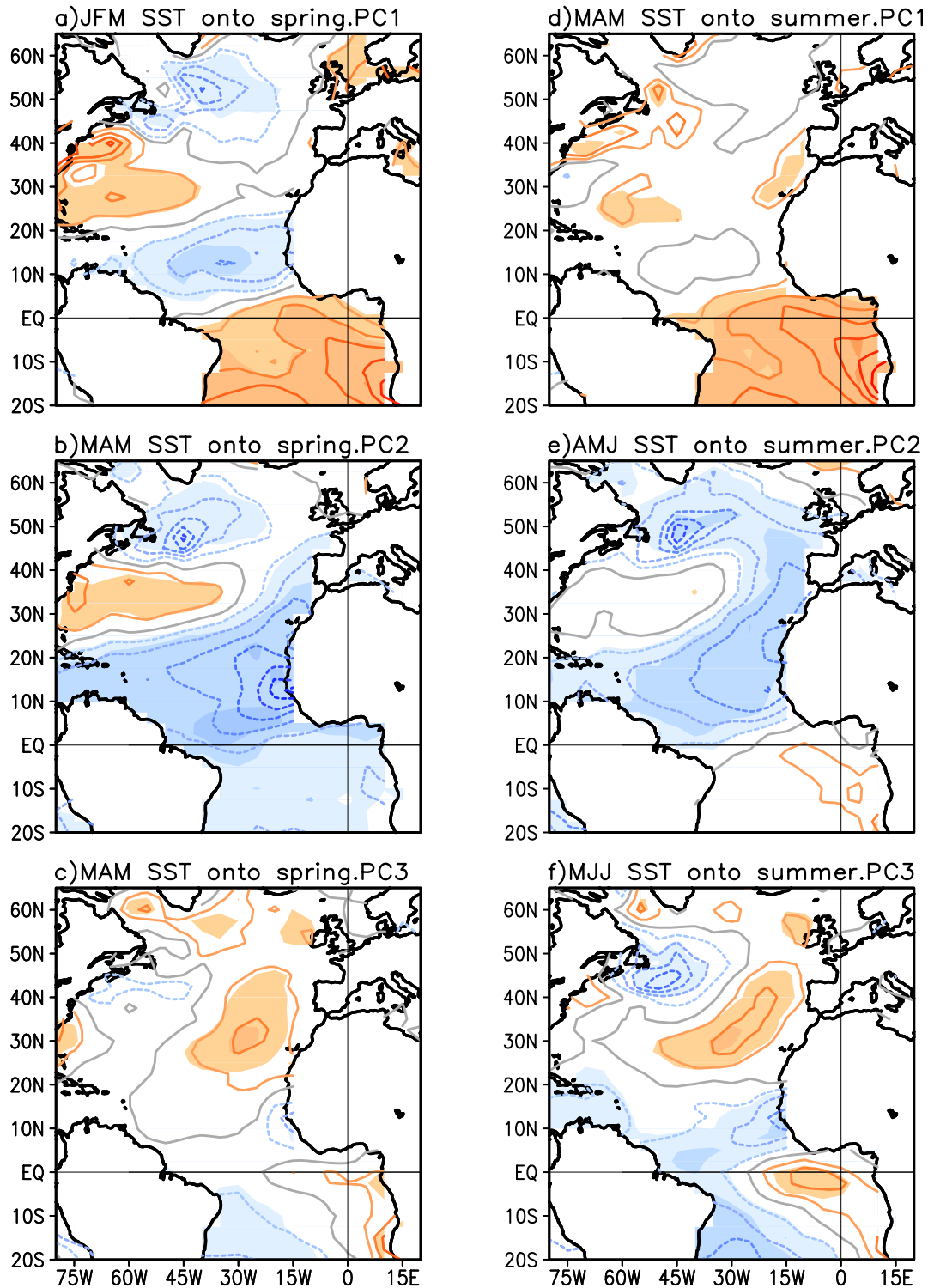


Figure B.0.2 Regression (contours) maps between the three-month-averaged SSTA onto the PCs derived from the original SSTA. Contour intervals: 0.1 °C. Correlation significance above 95% level are shaded.

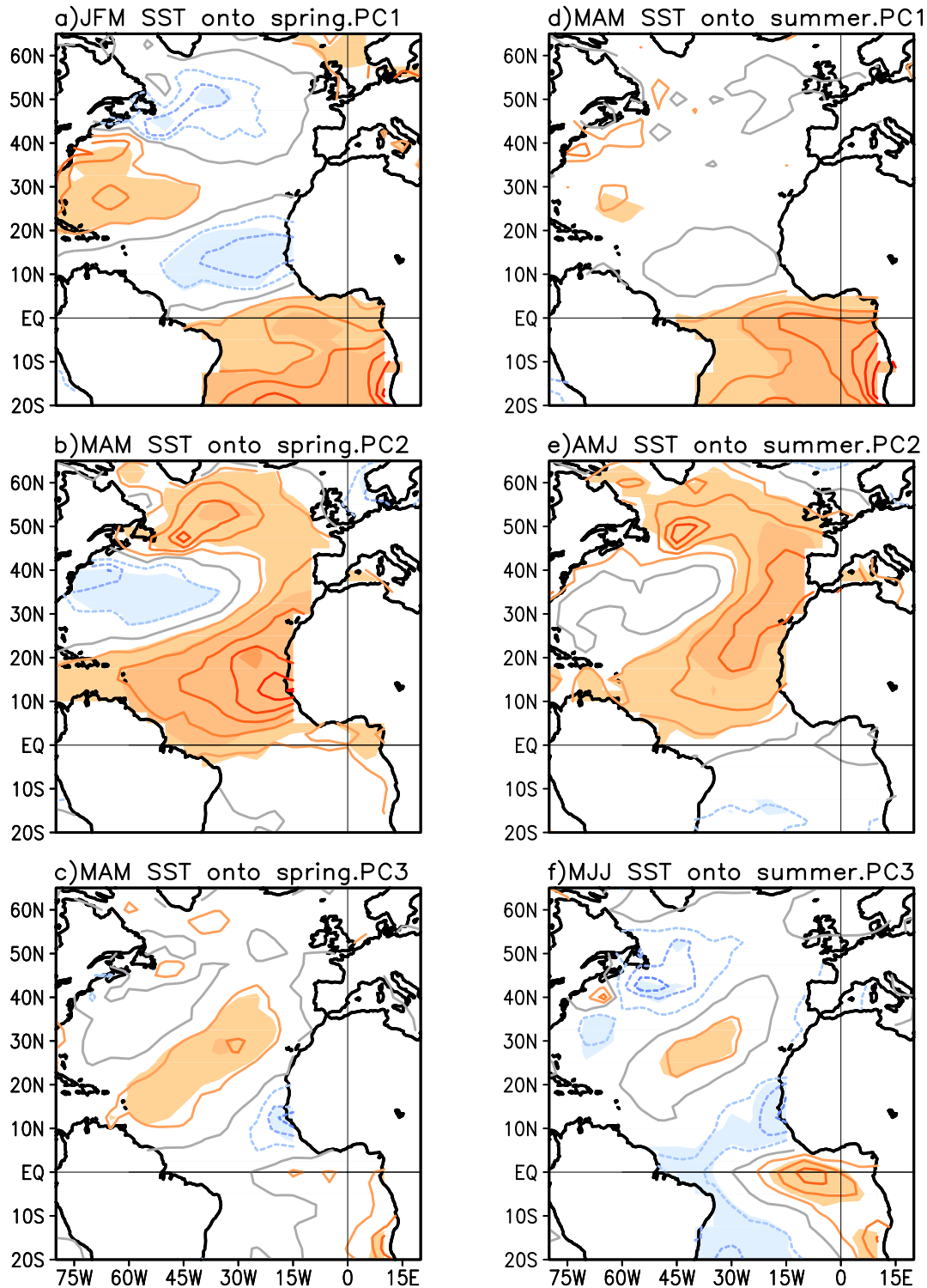


Figure B.0.3 Regression (contours) maps between the three-month-averaged SSTA onto the de-trended PCs derived from the ENSO-removed SSTA. Contour intervals: 0.1 °C. Correlation significance above 95% level is shaded.

C. Climate general circulation models

There are many aspects or features of the earth's climate that are not feasible to be reproduced in the laboratory, such as the long-term climate changes due to the increase of the greenhouse gases. To investigate more details of the mechanisms that are affecting the climate, or even to predict the climate, scientists rely on numerical simulation using climate general circulation models (CGCMs). A CGCM usually comprises a few component models, such as atmospheric model, ocean model, and land model. These component models communicate through a coupler to interact with other component models. Depending on the different interests of the research, there could be different combinations of the component models. For example, to focus on the dynamical aspects of the atmosphere and its thermodynamic interactions with the ocean, a combination of atmospheric general circulation model (AGCM) with a slab ocean model (an ocean model that only contains thermodynamic processes, but no dynamic processes) can work well. An AGCM coupled to an ocean GCM (OGCM) and land model (and/or ice model) is expected to contain most mechanisms of the dynamical and thermodynamic interactions between the research objects.

The fundamental equations that govern the motions of the atmosphere and oceans in AGCMs and OGCMs are called primitive equations which are a set of equations, derived from conservation laws for momentum, mass, and energy, and an equation of state, that describe hydrodynamic flow on the earth under hydrostatic approximation which assumes that vertical motion is much smaller than horizontal motion and that the fluid layer depth is small compared to the radius of the sphere. A general form of primitive equations for the atmosphere is as the following:

$$\frac{du}{dt} - \left(f + u \frac{\tan \phi}{a}\right)v = -\frac{1}{a \cos \phi} \frac{1}{\rho} \frac{\partial p}{\partial \lambda} + F_\lambda \quad (1)$$

$$\frac{dv}{dt} - \left(f + u \frac{\tan \phi}{a}\right)u = -\frac{1}{\rho a} \frac{\partial p}{\partial \phi} + F_\phi \quad (2)$$

$$g = -\frac{1}{\rho} \frac{\partial p}{\partial z} \quad (3)$$

$$\frac{\partial \rho}{\partial t} = -\frac{1}{a \cos \phi} \left[\frac{\partial}{\partial \lambda} (\rho u) + \frac{\partial}{\partial \phi} (\rho v \cos \phi) \right] - \frac{\partial (\rho w)}{\partial z} \quad (4)$$

$$C_p \frac{dT}{dt} - \frac{1}{\rho} \frac{dp}{dt} = Q \quad (5)$$

$$p = \rho RT, \quad (6)$$

where (u, v, w, ρ, p, T) stand for (zonal velocity, meridional velocity, vertical velocity, air density, pressure, air temperature), and a is the radius of the earth, λ and ϕ are longitude and latitude, respectively. F with a subscript represents the forcings in the corresponding direction. Q is the diabatic heating. For the ocean, the equation of state (equation (6) in the above) relates seawater density (ρ_w) to temperature (T), salinity (S), and pressure (p):

$$\rho_w = f(T, S, p)$$

The modeling of the oceans is similar to the modeling of the atmosphere in terms of the basic physics laws. The differences between them are 1) the dominant time scales in the oceans are much longer than those in the atmosphere due to the greater mass and thermal inertia, 2) the horizontal length scales of the relevant motions in the ocean are shorter than those in the atmosphere because of the small compressibility of the ocean and thus smaller radius of deformation, and 3) the radiative flux considerations are much more complicated for the ocean. The smaller radius of deformation in the ocean requires a much finer horizontal grid size for the ocean model (*Washington and Parkinson, 2005*).

Bibliography

- Adler, R.F. and Coauthors, 2003: The version 2 Global Precipitation Climatology Project (GPCP) monthly precipitation analysis. *J. Hydrometeor.*, 4, 1147–1167.
- Atlas, R., R.N. Hoffman, S.C. Bloom, J.C. Jusem, and J. Ardizzone, 1996: A multiyear global surface wind velocity dataset using SSM/I wind observations, *Bull. Amer. Met. Soc.*, 77, 869–882.
- Barreiro, M., P. Chang, L. Ji, R. Saravanan, and A. Giannini, 2005: Dynamical elements of predicting boreal spring tropical Atlantic sea-surface temperatures. *Dyn. Atmos. Oceans*, 39, 61–85.
- Boville, BA, and PR Gent, 1998: The NCAR Climate System Model, Version – One. *J. Climate*, 11, 1115–1130.
- Biasutti, M., D. S. Battisti, and E. S. Sarachik, 2005: Terrestrial influence on the annual cycle of the Atlantic ITCZ. *J. Climate*, 18, 211–228.
- Biasutti, M., A. Sobel, and Y. Kushnir, 2006: AGCM precipitation biases in the tropical Atlantic. *J. Climate*, 19, 935–958.
- Breugem, W-P, W. Hazeleger, R. J. Haarsma, 2006: Multimodel study of tropical Atlantic variability and change. *Geophys Res Lett* 33:doi:10.1029/2006GL027831
- Carlson, T. N., and S. G. Benjamin, 1980: Radiative heating rates for Saharan dust. *J. Atmos. Sci.*, 37, 193–213.
- Carton, J. A., and B. Huang, 1994: Warm events in the tropical Atlantic. *J. Phys. Oceanogr.*, 24, 888–903.
- Carton, J.A., and B.S. Giese, 2006: SODA: A Reanalysis of Ocean Climate. *J. Geophys. Res.*, submitted,
- Chan, S., and S. Nigam, 2007: Intercomparison of diabatic heating diagnosed from ERA-40, ERA-15, and NCEP-NCAR reanalyses (To be submitted to *J. Climate*, August 2007).
- Chang, C.-Y., J. A. Carton, S. A. Grodsky, and S. Nigam, 2007: Seasonal climate of the tropical Atlantic sector in the NCAR Community Climate System Model 3: Error structure and probable causes of errors. *J. Climate*, 20, 1053–1070.
- Chang, P., L. Ji, and H. Li, 1997: A decadal climate variation in the tropical Atlantic ocean from thermodynamic air-sea interactions. *Nature*, 385, 516–518.
- Chang, P., Y. Fang, R. Saravanan, L. Ji, and H. Seidel, 2006: The cause of the fragile relationship between the Pacific El Nino and the Atlantic Nino. *Nature*, 443, 324–327, doi:10.1038
- Chang, P., and G. Philander, 1994: A coupled ocean-atmosphere instability of relevance to the seasonal cycle. *J. Atmos. Sci.*, 51, 3627–3648.
- Chiang, J. C. H., Y. Kushnir, and A. Giannini, 2002: Deconstructing Atlantic Intertropical Convergence Zone variability: Influence of the local cross-equatorial sea surface temperature gradient and remote forcing from the eastern equatorial Pacific. *J. Geophys. Res.*, 107, 4004, doi:10.1029/2000JD000307
- Chiang, J. C. H. and D. J. Vimont, 2004: Analogous Pacific and Atlantic Meridional Modes of Tropical Atmosphere-Ocean Variability. *J. Climate*, 17, 4143–4158.
- Chiang, J., M. Biasutti, and D. S. Battisti, 2003: Sensitivity of the Atlantic Intertropical Convergence Zone to Last Glacial Maximum boundary conditions. *Paleoceanography*. 18, 1094, doi:10.1029/2003PA000916.

- Collins, W. D., C. M. Bitz, M. L. Blackmon, G. B. Bonan, C. S. Bretherton, J. A. Carton, P. Chang, S. C. Doney, J. J. Hack, T. B. Henderson, J. T. Kiehl, W. G. Large, D. S. McKenna, B. D. Santer, and R. D. Smith, 2006a: The Community Climate System Model Version 3 (CCSM3). *J. Climate*, 19, 2122-2143.
- Collins, W. D., P. J. Rasch, B. A. Boville, J. J. Hack, J. R. McCaa, D. L. Williamson, B. P. Briegleb, C. M. Bitz, S-J. Lin, and M. Zhang, 2006b: The formulation and atmospheric simulation of the Community Atmosphere Model Version 3 (CAM3). *J. Climate*, 19, 2144-2161.
- Cook, K. N. and E. K. Vizy, 2006: Coupled model simulations of the West African Monsoon system: twentieth- and twenty-first century simulations. *J. Climate*, 19, 3681–3703.
- Czaja, A., P. Van Der Vaart, and J. Marshall, 2002: A Diagnostic study of the Role of Remote Forcing in Tropical Atlantic Variability. *J. Climate*, 15, 3280–3290
- Davey, M., M. Huddleston, K.R. Sperber et al., 2002: STOIC: A study of coupled model climatology and variability in tropical ocean regions. *Clim. Dyn.*, 18, 403-420.
- DeWitt, D. G., 2005: Diagnosis of the tropical Atlantic near-equatorial SST bias in a directly coupled atmosphere-ocean general circulation model. *Geophys. Res. Lett.*, 32, L01703, doi:10.1029/2004GL021707
- Danabasoglu, G., and Coauthors, 2006: Diurnal coupling in the tropical oceans of CCSM3. *J. Climate*, 19, 2347–2365.
- Deser, C., A. Capotondi, R. Saravanan, and A. Phillips, 2006: Tropical Pacific and Atlantic climate variability in CCSM3. *J. Climate*, 19, 2451–2481.
- DeWitt, D. G., 2005: Diagnosis of the tropical Atlantic near-equatorial SST bias in a directly coupled atmosphere-ocean general circulation model. *Geophys. Res. Lett.*, 32, L01703, doi:10.1029/2004GL021707
- Enfield, D. B. and D. A. Mayer, 1997: Tropical Atlantic sea surface temperature variability and its relation to El Nino-Southern Oscillation. *J. Geophys. Res.-Ocn.* 102, 929–945
- Foltz, G. R., S. A. Grodsky, and J. A. Carton, 2003: Seasonal mixed layer heat budget of the tropical Atlantic Ocean. *J. Geophys. Res.*, 108, 3146, doi:10.1029/2002JC001584.
- Gill, A. E., 1980: Some simple solutions for heat budget induced tropical circulation. *Quart. J. R. Meteor. Soc.*, 106, 447–463
- Gill, A. E. 1982: Atmosphere-Ocean dynamics. Section 11.5: The Equatorial Kelvin Wave. Academic Press, International Geophysics Series, **30**, 436–437.
- Graf, J., C. Sasaki, C. Winn, W.T. Liu, W. Tsai, M. Freilich, and D. Long, 1998: NASA Scatterometer Experiment. *Acta Astronautica*, 43, 397-407.
- Grodsky, S. A., J. A. Carton, C. Provost, J. Servain, J. A. Lorenzetti, and M. J. McPhaden (2005), Tropical instability waves at 0 N, 23 W in the Atlantic: A case study using Pilot Research Moored Array in the tropical Atlantic (PIRATA) mooring data, *J. Geophys. Res.*, 110, C08010, doi:10.1029/2005JC002941.
- Grotzner, A, M. Latif, and D. Dommenges, 2000: Atmospheric response to sea surface temperature anomalies during El Nino 1997/98 as simulated by ECHAM4. *Quart. J. R. Meteor. Soc.*, 126, 2175-2198.

- Hagen, E., R. Feistel, J.J. Agenbag, and T. Ohde, 2001: Seasonal and interannual changes in intense Benguela upwelling (1982–1999), *Oceanologica Acta*, 24, 557–567.
- Hazeleger, W. and R. J. Haarsma, 2005: Sensitivity of tropical Atlantic climate to mixing in a coupled ocean-atmosphere model. *Climate Dynamics*, 25, 387–399 doi: 10.1007/s00382-005-0047-y
- Held, I. M., S.W. Lyons, and S. Nigam, 1989: Transients and the extratropical response to El Niño. *J. Atmos. Sci.*, 46, 163–174.
- Hirst, A. and S. Hastenrath, 1983: Atmosphere-ocean mechanisms of climate anomalies in the Angola-tropical Atlantic sector, *J. Phys. Oceanogr.*, 13, 1146–1157.
- Hoskins, B. J., H. H. Hsu, I. N. James, M. Masutani, P. D. Sardeshmukh, and G. H. White, 1989: Diagnostics of the global atmospheric circulation based on ECMWF analyses 1979–1989. WCRP-27; WMO/TD-No. 326, 217pp.
- Houze, R. A., Jr., 1997: Stratiform precipitation in regions of convection: A meteorological Paradox? *Bull. Amer. Meteor. Soc.*, 78, 2179–2196.
- Hu, Z.-Z., and B. Huang, 2007: Physical Processes Associated with the Tropical Atlantic SST Gradient during the Anomalous Evolution in the Southeastern Ocean. *J. Climate*, 20, 3366–3378.
- Hurrell JW, Y. Kushnir, G. Ottersen, and M. Visbeck, 2003: An overview of the North Atlantic Oscillation. In: Hurrell JW, Kushnir Y, Ottersen G, Visbeck M (eds) *The North Atlantic Oscillation: climatic significance and environmental impact*. Geophys Monograph 134, 1–35
- Janicot, S., 1992: Spatiotemporal variability of West African rainfall. Part II: Associated surface and air mass characteristics. *J. Climate*, 5, 499–511
- Kalnay, E., and Coauthors, 1996: The NCEP/NCAR 40-Year Reanalysis Project. *Bull. Amer. Meteor. Soc.*, 77, 437–471.
- Keenlyside, N. S. and M. Latif, 2007: Understanding Equatorial Atlantic Interannual Variability. *J. Climate*, 20, 131–142.
- Kushnir, Y., R. Seager, J. Miller, and J. C. H. Chiang, 2002: A simple coupled model of tropical Atlantic decadal climate variability. *Geophys. Res. Lett.*, 29, 2133, doi:10.1029/2002GL015874.
- Large, W.G. and G. Danabasoglu, 2006: Attribution and impacts of upper-ocean biases in CCSM3. *J. Climate*, 19, 2325–2346.
- Le Barbe, L., T. Lebel, and D. Tapsoba, 2002: Rainfall variability in West Africa during the years 1950–90. *J. Climate*, 15, 187–202
- Lee, S. K. and C. Z. Wang, 2008: Tropical Atlantic decadal oscillation and its potential impact on the equatorial atmosphere-ocean dynamics: A simple model study. *J. Climate*, 38, 193–212.
- Lindzen, R.S., and S. Nigam, 1987: On the role of sea surface temperature gradients in forcing low-level winds and convergence in the tropics. *J. Atmos. Sci.*, 44, 2418–2436.
- Li, T., and S. G. H. Philander, 1996: On the annual cycle of the eastern equatorial Pacific, *J. Climate*, 9, 2986–2998.

- Ma C. C., C. R. Mechoso, A. W. Robertson, A. Arakawa, 1996: Peruvian stratus clouds and the tropical Pacific circulation: A coupled ocean-atmosphere GCM study. *J. Climate*, 9, 1635-1645.
- Mitchell, T. D., and P. D. Jones, 2005: An improved method of constructing a database of monthly climate observations and associated high-resolution grids. *Int. J. Climatol.*, 25, 693–712.
- Mitchell, T. P., and J. M. Wallace, 1992: The annual cycle in equatorial convection and sea surface temperature. *J. Climate*, 5, 1140–1156.
- Moura, A. and J. Shukla, 1981: On the dynamics of droughts in northeast Brazil: Observations, theory and numerical experiments with a general circulation mode. *J. Atmos. Sci.*, 38, 2653–2675.
- Murtugudde, R. G., J. Ballabrera-Poy, J. Beauchamp, and A. J. Busalacchi, 2001: Relationship between zonal and meridional modes in the tropical Atlantic. *Geophys. Res. Lett.*, 22, 4463–4466.
- Nicholson, S. E., and P. J. Webster, 2007: A physical basis for the interannual variability of rainfall in the Sahel. *Q. J. Royal Met. Soc.*, 133, 2065-2084
- Nigam, S., 1994: On the dynamical basis for the Asian summer monsoon rainfall-EL Nino relationship. *J. Climate*, 7, 1750-1771.
- Nigam, S., and Y. Chao, 1996: Evolution dynamics of tropical ocean-atmosphere annual cycle variability. *J. Climate*, 9, 3187–3205.
- Nigam, S., 1997: The annual warm to cold phase transition in the eastern equatorial Pacific: Diagnosis of the role of stratus cloud-top cooling. *J. Climate*, 10, 2447-2467.
- Nigam, S., C. Chung, and E. DeWeaver, 2000: ENSO diabatic heating in ECMWF and NCEP Reanalyses, and NCAR CCM3 simulation. *J. Climate*, 13, 3152-3171.
- Nigam, S., and C. Chung, 2000: ENSO surface winds in CCM3 simulation: diagnosis of errors. *J. Climate*, 13, 3172-3186.
- Okumura, Y., and S.-P. Xie, 2004: Interaction of the Atlantic Equatorial Cold Tongue and the African Monsoon. *J. Climate*, 17, 3589–3602.
- Okumura, Y., and S.-P. Xie, 2006: Some overlooked Tropical Atlantic Climate Leading to a New Nino-like Phenomenon. *J. Climate*, 19, 5859-5874
- Pinker, R. T., I. Laszlo, and B. Zhang, 2001: Pathfinder large scale radiative fluxes: data availability and their use in climate research, in *IRS 2000: Current Problems in Atmospheric Radiation*, W. L. Smith and Yu. M. Timofeyev (Eds.). A. Deepak Publishing, Hampton, Virginia. pp. 485-488.
- Rayner, N. A., D. E. Parker, E. B. Horton, C. K. Folland, L. V. Alexander, D. P. Rowell, E. C. Kent, and A. Kaplan, 2003: Global analysis of sea surface temperature, sea ice, and night marine air temperature since the late nineteenth century. *J. Geophys. Res.*, 108, 4407, doi:10.1029/2002JD002670
- Reynolds, R., N. Rayner, T. Smith, D. Stokes, and W. Wang, 2002: An improved in situ and satellite SST analysis for climate. *J. Clim.*, 15, 1609–1625.
- Richter, I., C. R. Mechoso, and A. W. Robertson, 2008: What determines the position and intensity of the South Atlantic anticyclone in austral winter? – An AGCM study. *J. Clim.*, 21, 214-229.
- Richter, I. and S.-P. Xie, 2008: On the origin of equatorial Atlantic biases in coupled general circulation models. *Clim. Dyn.*, in press.

- Ruiz-Barradas, A., J. A. Carton, and S. Nigam, 2000: Structure of interannual-to-decadal climate variability in the tropical Atlantic sector. *J. Clim.*, 13, 3285–3297.
- Ruiz-Barradas A, J.A. Carton and S. Nigam, 2003: Role of the atmosphere in climate variability of the tropical Atlantic. *J. Clim.*, 16, 2052-2065.
- Saha, S., S. Nadiga, C. Thiaw, J. Wang, W. Wang, Q. Zhang, D. Behringer, W. Ebisuzaki, S. Lord, S. Moorthi, H.L. Pan, P. Peng, D. Stokes, H. M. van den Dool, G. White, P. Xie, 2006: The Climate Forecast System at NCEP. *J. Climate*, 19, 3483-3517.
- Servain, S., J. Picaut, and J. Merle, 1982: Evidence of remote forcing in the equatorial Atlantic Ocean. *J. Phys. Oceanogr.*, 12, 457–463.
- Servain, J., I. Wainer, J. P. McCreary Jr., A. Dessier, 1999: Relationship between the equatorial and meridional modes in the tropical Atlantic. *Geophys. Res. Lett.*, 23, 57–60.
- Servain, J., I. Wainer, H. L. Ayina, and H. Roquet, 2000: The relationship between the simulated climatic variability modes of the tropical Atlantic. *Int. J. Climatol.*, 20, 939–953.
- Skole, D. and C. Tucker, 1993: Tropical deforestation and habitat fragmentation in the Amazon - Satellite data from 1978 to 1988. *Science*, 260, 1905-1910.
- Stockdale T.N., M. A. Balmaseda, A. Vidard, 2006: Tropical Atlantic SST prediction with coupled ocean-atmosphere GCMs. *J. Clim.*, 19, 6047-6061.
- Uppala, S. M., and Coauthors, 2005: The ERA40 reanalysis. *Q. J. Royal Met. Soc.*, 131, 2961-3012.
- Vimont, D. J., D. S. Battisti, and A. C. Hurst, 2001: Footprinting: A seasonal connection between Tropics and mid-latitudes. *Geophys. Res. Lett.*, 28, 3923–3926.
- Xie, S.-P., 1994: On the genesis of the equatorial annual cycle. *J. Climate*, 7, 2008-2013.
- Xie, S.-P., and J.A. Carton, 2004: Tropical Atlantic variability: patterns, mechanisms, and impacts. To appear in the AGU Geophysical Monograph on Ocean-Atmosphere Interaction and Climate Variability, C. Wang, S.-P. Xie, and J. Carton, eds.
- Yu, J.-Y., and C. R. Mechoso, 1999: A discussion on the errors in the surface heat fluxes simulated by a coupled GCM. *J. Climate*, 12, 416–426.